N86-28953

NASA CR-177,112

JANUARY 1986

LIDS-TH-1530

NASA-CR-177112
19860019481

Research Supported By

*NASA Ames and Langley
Research Centers
Grant NASA/NAG 2-297*

MULTIVARIABLE CONTROL OF A FORWARD SWEPT WING AIRCRAFT

Wilma W. Quinn

Laboratory for Information and Decision Systems
MASSACHUSETTS INSTITUTE OF TECHNOLOGY, CAMBRIDGE, MASSACHUSETTS 02139

January 1986 LIDS-TH-1530

MULTIVARIABLE CONTROL OF A FORWARD SWEPT WING AIRCRAFT

by

Wilma W. Quinn

This report is based on the unaltered thesis of Wilma W. Quinn submitted in partial fulfillment of the requirements for the Degree of Master of Science in Electrical Engineering at the Massachusetts Institute of Technology in December 1985. This research was carried out at the MIT Laboratory for Information and Decision Systems with support provided by the NASA Ames and Langley Research Centers under Grant NASA/NAG 2-297.

Massachusetts Institute of Technology
Laboratory for Information and Decision Systems
Cambridge, Massachusetts 02139

MULTIVARIABLE CONTROL
OF A
FORWARD SWEPT WING AIRCRAFT

By

WILMA W. QUINN

BSME LEHIGH UNIVERSITY (1980)

MSME DREXEL UNIVERSITY (1983)

SUBMITTED IN PARTIAL FULFILLMENT
OF THE REQUIREMENTS FOR THE
DEGREE OF MASTER OF SCIENCE
IN ELECTRICAL ENGINEERING
AT THE
MASSACHUSETTS INSTITUTE OF TECHNOLOGY

DECEMBER 1985
MASSACHUSETTS INSTITUTE OF TECHNOLOGY

Signature of Author Wilma W Quinn
Department of Electrical
Engineering, December 1985

Certified By Michael Athans
Professor M. Athans
Thesis Advisor

Accepted By ______________________
Chairman, Department Committee
on Graduate Students

MULTIVARIABLE CONTROL
OF A
FORWARD SWEPT WING AIRCRAFT

By

WILMA W. QUINN

Submitted to the Department of Electrical Engineering in December 1985 in partial fulfillment of the requirements for the degree of Master of Science in Electrical Engineering.

ABSTRACT

The impact of independent canard and flaperon control of the longitudinal axis of a generic forward swept wing aircraft is examined. The LQG/LTR method is used to design three compensators: two single-input-single-output systems, one with angle of attack as output and canard as control, the other with pitch attitude as output and canard as control, and a two-input-two-output system with both canard and flaperon controlling both the pitch attitude and angle of attack. The performances of the three systems are compared showing the addition of flaperon control allows the aircraft to perform in the precision control modes with very little loss of command following accuracy.

THESIS SUPERVISOR: Dr. Michael Athans, Professor of Systems
Science and Engineering

ACKNOWLEDGEMENTS

I would like to thank my thesis advisor, Dr. Michael Athans, for his help throughout this research. I would also like to thank Dr. Gunter Stein for patiently answering my questions. Finally, I would like to thank my husband and daughter for their support.

This research was carried out at the MIT Laboratory for Information and Decision Systems with support provided by the NASA Ames and Langley Research Centers under grant NASA/NAG 2-297.

MULTIVARIABLE CONTROL
OF A FORWARD
SWEPT WING AIRCRAFT

Chapter 1: Introduction and Summary

Chapter 2: System Description and Model Formulation

Chapter 3: Model Analysis and Design Specification

MULTIVARIABLE CONTROL
OF A FORWARD
SWEPT WING AIRCRAFT

Chapter 4: LQG/LTR Designs

Chapter 5: Flaperon Effectiveness in the Precision Control Modes

Chapter 6: Control of Wing Tip Bending Rate

Chapter 7: Summary, Conclusions and Directions For Further Research

LIST OF FIGURES

Chapter 2:

Chapter 3:

LIST OF FIGURES

Chapter 3 (Cont):

Chapter 4:

LIST OF FIGURES

Chapter 4 (Cont):

Chapter 5:

LIST OF FIGURES

Chapter 5 (Cont):

Chapter 6:

LIST OF TABLES

Chapter 2:

Chapter 3:

Chapter 4:

Chapter 6:

CHAPTER 1: INTRODUCTION AND SUMMARY

1.1 Background

Forward swept wing aircraft were not generally built before composite materials became available. The Germans designed and built a forward swept wing bomber during World War II, but it was captured before it became operational [1]. The potential advantages of a forward swept wing aircraft are better maneuverability, low stall speed, improved low speed handling, increased aerodynamic efficiency and shorter takeoff and landing distances [2, 3]. The problem is that the dynamic pressures associated with transonic flight results in the divergence phenomenon; the wings twist and bend beyond their structural limits. This divergence tends to occur at lower speeds for the forward swept wing than for the aft swept wing. Increasing the wing stiffness requires adding metal, which increases the weight and the wings may still fail. However, composite wings can be tailored to give strength in the required directions without large weight penalties [4, 5]. N.J. Krone showed that a practical forward swept wing aircraft can be built using composite materials [6]. The X-29 aircraft is, of course, a forward-swept wing airplane, built by Grumman, that is currently being flight tested.

References 2, 7, 8, 9, 10, and 11 describe work done at Purdue University investigating wing divergence and control of the forward swept wing aircraft. Dynamic Modeling and Active Control of an Aeroelastic Aircraft by M. Gilbert [7] contains the development of a linear model of a generic forward swept wing aircraft. In addition, in Reference 7 a linear quadratic regulator is designed which stabilizes pitch rate and dampens the wing bending mode using both the canard and flaperon as controls.

1.2 Motivation

The goal of this study is to investigate the usefulness of independent canard and flaperon control. The model of a generic forward swept wing aircraft developed in Reference 7 will be used. The major emphasis is on the coordinated use of the canard and flaperon surfaces to independently control both the angle of attack and pitch attitude. Most of the studies [20] that relate to the longitudinal dynamics of the X-29 treat it as a single-input-single-output system either using the canard as the sole control variable, or by slaving the canard and the flaperons. Although the flaperons may have limited control authority, it was felt that it would be interesting to design a multivariable control system to investigate their effect in controlling small motions in the longitudinal plane. An alternate configuration, using the flaperon and canard to control pitch rate and wing bending rate will be examined briefly.

1.3 Research Scope

The major goal of this thesis is to examine the usefulness of coordinated canard and flaperon control surfaces, particularly with angle of attack and pitch attitude as independent outputs.

The LQG/LTR multivariable technique [12, 21] will be used to design the controllers. Two single-input-single-output (SISO) designs will be examined first. The canard is used to control angle of attack in the first SISO design, while it is used to control pitch attitude in the second SISO design. The characteristics of these systems are used to gain insight into the two-input-two-output (TITO) system, in which both the flaperon and canard are used to independently control small commands for angle of attack and pitch attitude. The performance of the three designs will be compared in order to understand and highlight the impact of flaperon control.

The design issues involved include the tradeoff between good performance and neglected high frequency dynamics. This tradeoff is further complicated by the open loop aircraft instability, which imposes its own minimum bandwidth limitations.

Also, it should be noted that all the LQG/LTR designs do not require sensing of all aircrafts states, only of the outputs that we wish to control.

The compensators designed in this study are introduced to exhibit feasibility of independent flaperon and canard control. These feedback control designs are not ready for implementation on an actual aircraft.

1.4 Contribution

The major contribution of this thesis is the investigation of coordinated flaperon and canard independent surfaces for control of the pitch attitude and angle of attack for a forward swept wing aircraft. The performance in the three precision control modes, with and without flaperon control, is investigated. An alternate configuration, using the canard and flaperon to control pitch rate and wing bending rate is briefly examined.

In addition, the solution to this design problem gives an example of how to proceed in multivariable LQG/LTR based designs considering an unstable open loop system and lightly damped flexible mode. The design is evaluated in terms of command-following, disturbance rejection and stability-robustness considerations when we intentionally ignore high frequency wing torsion mode dynamics. From a technical point of view, we have used extensively the directional information inherent in the singular value decomposition to tie the mathematics to the physics of the aircraft.

1.5 Outline of Thesis

Chapter 2 contains a description of the longitudinal dynamics of the forward swept wing aircraft model, including a brief explanation of how the linear model was developed. A description of the linear model is included, explaining the states, inputs, outputs, and scaling of the units of the variables.

Chapter 3 is devoted to analysis. The linear model is examined in terms of its poles and zeroes, modes, controllability, frequency response, and singular values. The technique of using model errors for design purposes is described, as well as the specific errors for this model. The design specifications are developed in terms of performance and robustness requirements. These are translated to the frequency domain to give performance specifications in terms of singular values.

Chapter 4 contains a brief explanation of the LQG/LTR design method, followed by the two SISO and the single TITO designs. The performance of the closed-loop systems with and without flaperon control are compared in Chapter 5. The regulator designed in Reference 7 to stabilize pitch rate and increase the wing bending dampening is investigated in Chapter 6. Chapter 7 contains the summary, conclusions, and suggestions for further research.

CHAPTER 2: SYSTEM DESCRIPTION AND MODEL FORMULATION

2.1 Introduction

The X29 is an experimental forward swept wing aircraft. It was built by Grumman Aerospace Corp. for the U.S. Defense Advanced Research Projects Agency (DARPA). In February 1985, the X29-A completed its first phase of flight tests [13]. Figure 2.1 is a photograph of the X29 [14].

This study uses a model of a generic forward swept wing aircraft developed by M.G. Gilbert in Dynamic Modeling and Active Control of an Aeroelastic Aircraft [7]. The generic aircraft is roughly the same size as the X29. The wings are swept forward at a 30° angle. The model flight velocity is 1000 ft/s at sea level.

The linearized aircraft model is described in this chapter. The controls are explained briefly and their trim settings at the model operating point are listed. A short description of the longitudinal coordinates and the flexible wing modes is given. Finally, the linear model is analyzed from a mathematical point of view and the scaling of variables is explained.

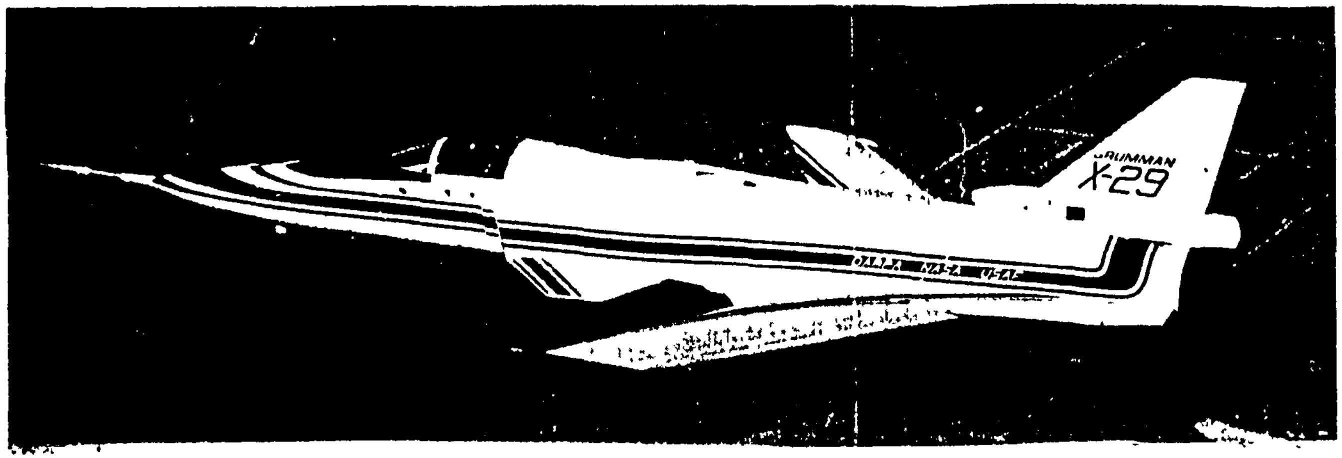

Figure 2.1 Photograph of the X-29 during flight testing.

2.2 Aircraft Model Description

The forward swept wing aircraft has four controls in the longitudinal axis: flaperon, canard, strake and thrust. Figure 2.2 shows the locations of each of the control surfaces.

The flaperons are hinged airfoils on the back of the wing, which may be used to generate lift and some pitching moment. The canards are the surfaces in front of the wing. They also generate lift and pitching moments. The third pair of control surfaces are the strake flaps. These are at the rear of the aircraft and are used with the flaperon and canard to stabilize the aircraft longitudinal axis. The strake is used primarily for trimming the aircraft [1]. For this reason we shall not use the strake as a dynamic control variable, and we shall limit our investigation to the dynamic coordinated control of the canard and flaperon surfaces.

The linear model thus uses only two of the control surfaces, flaperons and canards. The maximum canard deflections are +60° and -30° where a positive canard deflection is downward. Since the canards are in front of the center of gravity, a positive deflection causes a positive pitching moment about the cg. Figure 2.3 illustrates the effect of a positive canard deflection. The maximum flaperon deflections are -10° and +25°. The flaperons are behind the cg, therefore a positive flaperon

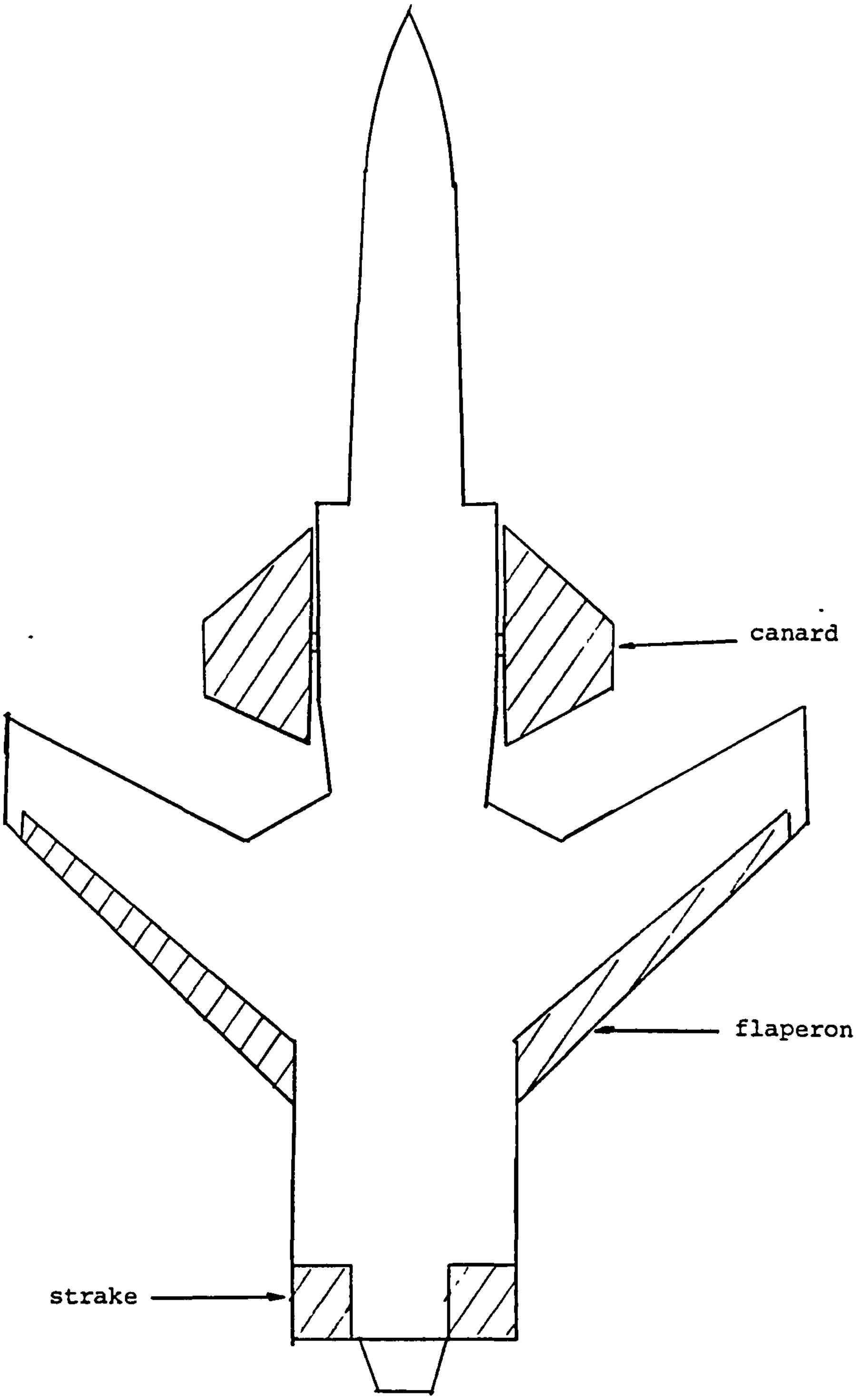

Figure 2.2 Sketch of the X29, showing control surfaces: canards, flaperons, strakes

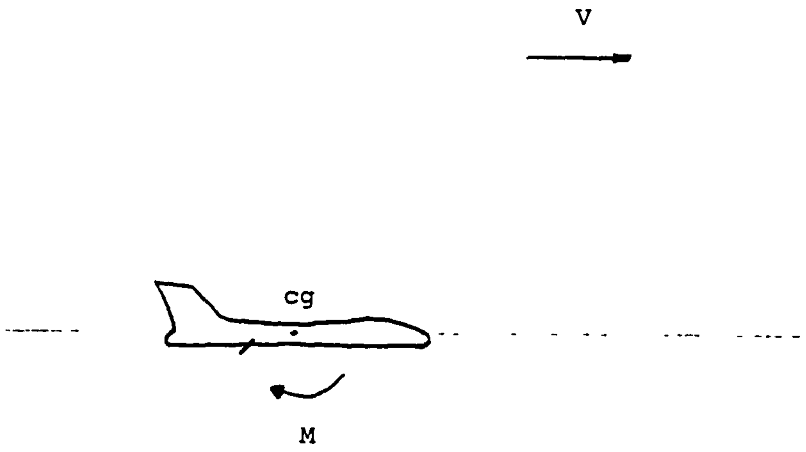

a. positive flaperon deflection causes negative pitching moment

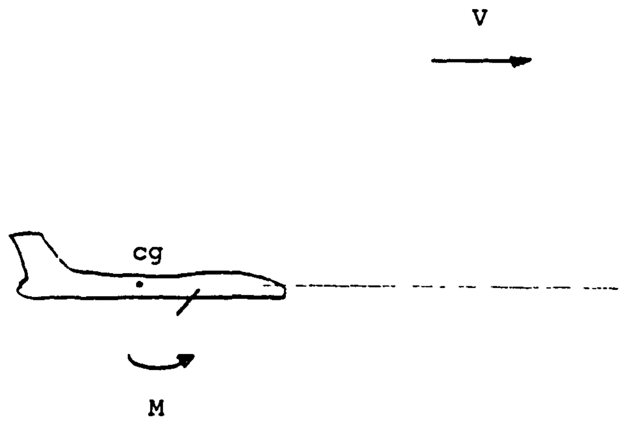

b. positive canard deflection causes positive pitching moment

Figure 2.3 Pitching moment due to positive flaperon and canard deflections deflection produces a negative pitching moment. This is also illustrated in Figure 2.3.

The longitudinal outputs of interest are the angle of attack and the pitch attitude. The angle of attack, α, is the angle between the longitudinal axis fixed to the plane and the velocity vector in the xz plane, where x points forward and z points downward. Figure 2.4 shows the angle of attack. The pitch attitude, θ, also shown in Figure 2.4, is the angle between the horizen and the longitudinal axis of the plane. The third angle of interest, which is dependent on both angle of attack and pitch attitude is the flight path angle, γ. This angle, also shown in Figure 2.4, is the difference between angle of attack and pitch attitude. It is the angle between the horizon and the velocity vector in the xz plane.

Coordinated deflection of the flaperons and canards allows limited precision control of the angle of attack and pitch angle. The three precision control modes, which are illustrated in Figure 2.5 are:

1. Vertical Translation; which provides control over vertical velocity while maintaining constant pitch attitude.
2. Pitch Pointing; where the pitch attitude is controlled at constant flight path angle by varying the angle of attack.
3. Direct Lift; in which the angle of attack remains constant and pitch angle varies [15,16].

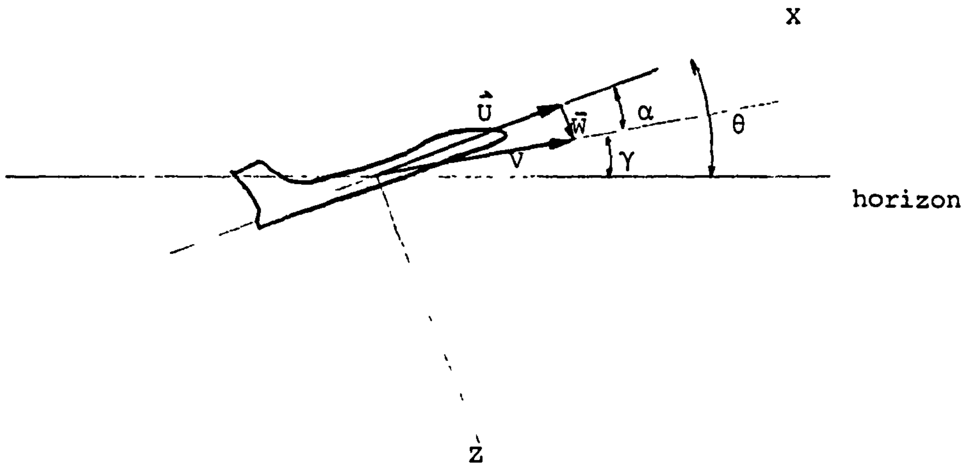

$$\alpha = \tan^{-1} W/U$$

$$\gamma = \theta - \alpha$$

Figure 2.4 Definitions of angle of attack (α), pitch attitude (θ), and flight path angle (γ)

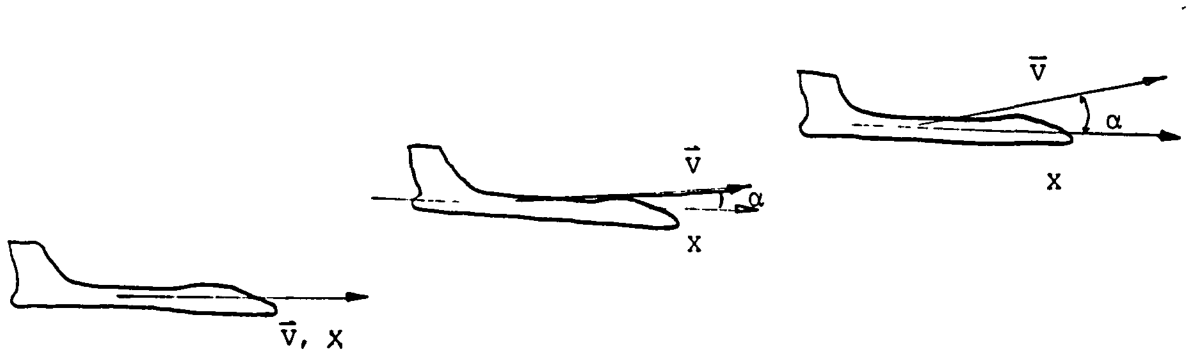

a. Vertical Translation: θ = constant

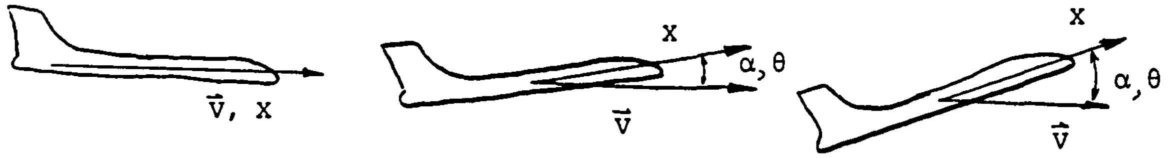

b. Pitch Pointing: γ = constant

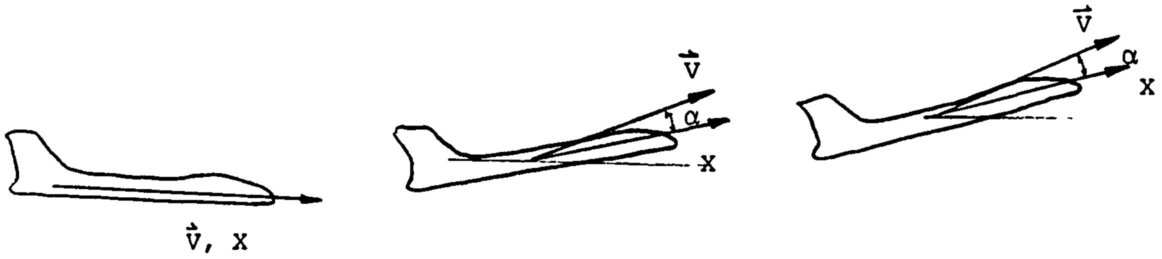

c. Direct Lift: α = constant

Figure 2.5 Longitudinal Precision Control Modes

2.3 Linear Model

2.3.1 Model Development

The linear model used in this study was developed by M.G. Gilbert [7]. The model is based on an aircraft with a rigid fuselage and flexible wings. The structural motions of the aircraft are characterized by the "in-vacuo" free-free normal vibration mode shapes and generalized structural coordinates using finite element techniques. Aircraft kinetic and potential energies and generalized forces are used in a mean reference axis coordinate system. Lagrange's method is used to obtain the aircraft equations of motion. The force terms in the equation of motion are written in terms of lift, moment, and drag coefficients assuming a quasi-steady aerodynamic representation. The non-linear equations of motion are then linearized about a steady-state reference flight condition using small perturbation theory. The equations of motion are written in state variable form in a body-fixed coordinate system [7].

The operating point used in this study is at a velocity of 1000 ft/s at sea level, which is about Mach 0.9. This corresponds to a dynamic pressure of 1189 lb/ft^2. Three models were given in Reference 7 corresponding to three different center of gravity locations. The model with the cg in the center position was used in this study.

2.3.2 Trim Settings

The generic forward swept wing aircraft is modelled about an operating point of 1000 ft/s at sea level in this study. The trim setting which corresponds to this operating point for the X29, the actual forward swept wing aircraft, is trim angle of attack of 2.51° and trim pitch angle of 2.51°. Since the flight path angle is the difference between angle of attack and pitch attitude, the aircraft is in level flight.

The flaperon trim setting is -3.05°; the canard trim setting is -2.8°. Based on these trim values the constraints in flaperon and canard deflections about the trim setting are

$$-6.95° < f(t) < 28.05°$$

and

$$-27.2° < c(t) < 62.8°.$$

2.3.3 State Variable Model

The model, in state variable form is

$$\dot{\underline{x}}(t) = \underline{A}\ \underline{x}(t) + \underline{B}\ \underline{u}\ (t) \qquad (2.1)$$

where $\underline{x}(t)$ is the state vector and $\underline{u}(t)$ is the control vector. See Table 2.1 for definitions.

The four states are the usual rigid dynamic state variables. The first flexible mode represents the <u>wing tip bending</u>; $N_1(t)$ is the wing tip deflection from its undeformed position in ft, $\dot{N}_1(t)$ is its rate of deflection in ft/s. The second flexible mode represents <u>wing torsion</u>,

$N_2(t)$ is the wing rotation about the elastic axis in rad, $\dot{N}_2(t)$ is its rate of deflection in rad/s. Figure 2.6 is a sketch showing $N_1(t)$ and $N_2(t)$. Appendix 1.1 lists the $\underline{A}$ and $\underline{B}$ matrices, as well as the vibration mode shape for the model with its cg in its center location, two feet in front of the wing root.

The input control vector $\underline{u}(t)$ is $[f(t)\ c(t)]^T$ where $f(t)$ is the flaperon deflection from trim in radians and $c(t)$ is the canard deflection from trim, also in radians.

The output equation is of the form

$$\underline{y}(t) = \underline{C}\ \underline{x}(t) \qquad (2.2)$$

where $\underline{y}(t)$ is $[\alpha(t)\quad \theta(t)]^T$ for the TITO design. Ideal actuators and sensors have been assumed for this study.

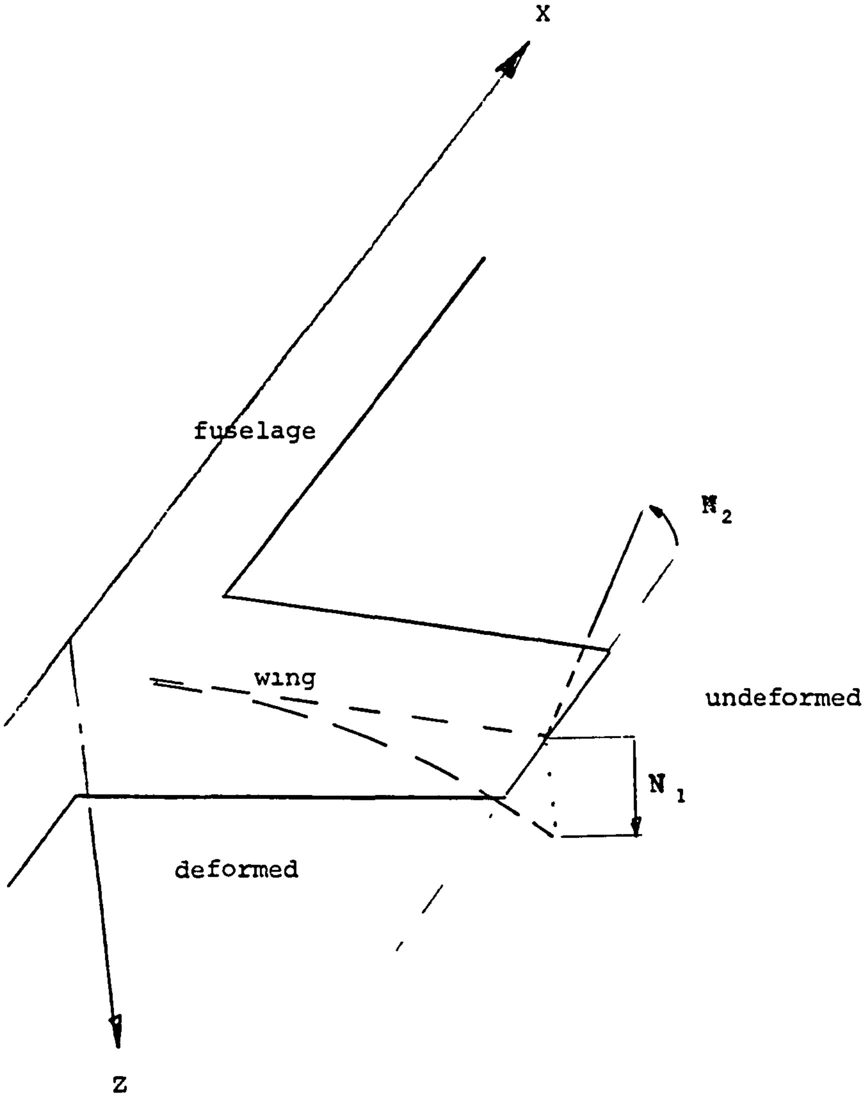

N_1 : vertical deflection at tip

N_2 : rotation about elastic axis

Figure 2.6 Flexible Wing Modes

TABLE 2.1

SUMMARY OF MODEL STATES, INPUTS AND OUTPUTS

STATE VARIABLES (DEVIATION FROM TRIM)		UNITS
$\underline{x}(t)$:		
$v(t)$	Velocity	ft/s
$\alpha(t)$	Angle of Attack	rad
$\theta(t)$	Pitch Attitudes	rad
$q(t)$	Pitch Rate	rad/s
$N_1(t)$	Wing Tip Deflection	ft
$\dot{N}_1(t)$	Wing Tip Rate	ft/s
$N_2(t)$	Wing Rotation	rad
$\dot{N}_2(t)$	Wing Rotation Rate	rad/s

INPUTS (DEVIATION FROM TRIM)		UNITS
$\underline{u}(t)$:		
$f(t)$	Flaperon Deflection	rad
$c(t)$	Canard Deflection	rad

2.3.4 Scaling

Scaling is very important in multivariable control as it influences the relative sizes of the variables. For example, comparing some variables in degrees with others in radians does not make much sense. It may or may not be reasonable to compare variables in degrees with variables in feet.

The eigenvalues will not be changed when a system is scaled, however the eigenvectors and the singular values will change.

The scaling was done in two steps. The first step was unit conversions; angle of attack, pitch angle and pitch rate were converted from radians to degrees. The second step was based on the physical limits of the controls. The canard and flaperon commands were scaled to make the deflections comparable to each other. Ideally the inputs would have the same range, i.e. from -1 to +1. Since the negative deflection range is smaller than the positive deflection range, the scaling was done to make them nearly uniform. The flaperon deflections were scaled down by 12 making the allowed commands from trim

$$-0.58 < f(t) < 2.34.$$

The canard deflections were scaled down by 30 making the allowed commands from trim

$$-0.91 < c(t) < 2.09.$$

The procedure for scaling is based on similarity transformations. The original system is

$$\dot{\underline{x}}(t) = \underline{A}\ \underline{x}(t) + \underline{B}\ \underline{u}(t) \qquad (2.1)$$

$$\underline{y}(t) = \underline{C}\ \underline{x}(t). \qquad (2.2)$$

The scaled variables $\underline{x}'(t)$, $\underline{y}'(t)$ and $\underline{u}'(t)$ are related to $\underline{x}(t)$, $\underline{y}(t)$ and $\underline{u}(t)$ as

$$\begin{aligned} \underline{x}'(t) &= \underline{S}_x\underline{x}(t) \\ \underline{u}'(t) &= \underline{S}_u\underline{u}(t) \qquad (2.3) \\ \underline{y}'(t) &= \underline{S}_y\underline{y}(t) \end{aligned}$$

Substituting (2.3) into (2.1) and (2.2) results in

$$\underline{x}'(t) = \underline{S}_x\underline{A}\underline{S}_x^{-1}\ \underline{x}'(t) + \underline{S}_x\underline{B}\underline{S}_u^{-1}\ \underline{u}'(t) \qquad (2.4)$$

$$\underline{y}'(t) = \underline{S}_y\underline{C}\underline{S}_x^{-1}\ \underline{x}'(t) + \underline{S}_y\underline{D}\underline{S}_u^{-1}\ \underline{u}'(t) \qquad (2.5)$$

Since these are scaling conversions $\underline{S}_x$, $\underline{S}_u$ and $\underline{S}_y$ are diagonal and the inverses exist.

The scaling matrices for the linear model of the FSW aircraft used in this study are given in Appendix 1.2. The scaled $\underline{A}$ & $\underline{B}$ matrices are also listed. Figure 2.7 is a block diagram which shows how the scaling matrices fit in with the original system matrices.

2.4 Summary

The forward swept wing (FSW) aircraft has been described in this chapter. The method of development of a linear model was briefly explained. A more detailed linear model development is described in reference [7].

The state variables, inputs and outputs of the linear model were all specified and units listed. Finally the trim setting was given and scaling explained.

Chapter 3 describes the analysis of the linear model in terms of modes and singular values.

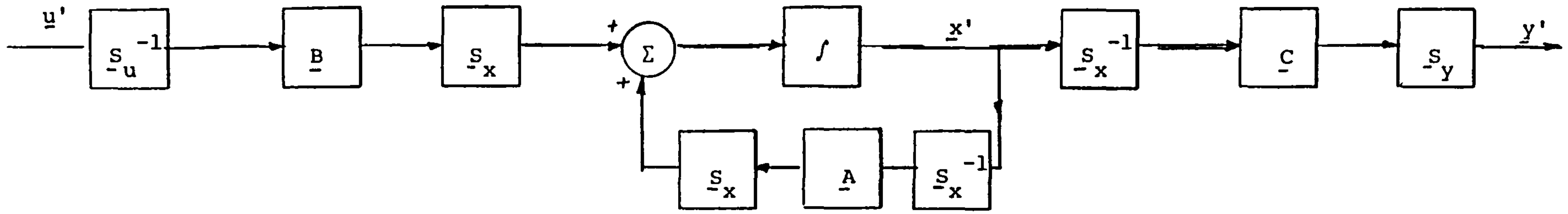

Figure 2.7 Block Diagram of Scaled Plant

CHAPTER 3: MODEL ANALYSIS AND DESIGN SPECIFICATIONS

3.1 Introduction

The linear model of Chapter 2 will be analyzed in this chapter. The analysis will be used to provide insight into the system dynamics and to form reasonable design specifications. In this chapter the pole/zero structure of the open loop system, as well as the modes, controllability, frequency response and singular value decomposition will be examined. The open loop transfer matrix, relating inputs to outputs will also be studied.

In addition to the analysis of the linear model, this chapter contains a brief explanation of the procedure for using model errors in the design process. The specific model errors based on a design model and a "truth" model, are also given. The design specifications are derived in terms of singular values based on performance requirements and robustness considerations.

It is worthwhile to remark at this stage that the "truth model" is that described in Chapter 2. For purposes of design we have defined the "design model" so as to include the wing tip bending mode but exclude the wing torsional mode. Our design procedure will then be based on stability-robustness constraints that will not destabilize the neglected wing torsional mode dynamics.

The major conclusions based on the analysis of the linear model are:

1) The flaperon (as expected) has much less command authority than the canard.
2) The bending and torsion modes are relatively unobservable when pitch attitude and angle of attack are used as output variables.
3) The maximum singular value direction of the open-loop plant at DC is primarily from the canard to angle of attack; while at a higher frequency it is from canard to pitch attitude.

Three design models will be examined: the SISO system with only canard as control and angle of attack as output, which will be referred to as Design Model A, the SISO system with canard control and pitch attitude output which will be referred to as Design Model B, and the TITO system with both canard and flaperon controls and the angle of attack and pitch attitude output, which will be referred to as Design Model C.

3.2 Truth Model Analysis

3.2.1 Pole/Zero Structure

The linear truth model has eight states, the four rigid body states v, α, θ and q, and four flexible states for the wing bending and torsion modes. Table 3.1 lists the eight eigenvalues of the $\underline{A}$ matrix which are the aircraft model open loop poles. Three of the modes are very easy to

TABLE 3.1
OPEN LOOP POLES AND ZEROES OF TRUTH MODEL

POLES:

MODE	FREQUENCY (Rad/Sec)	DAMPING	EIGENVALUES (Rad/Sec)
Short Period Mode			7.3079 -11.918
Phugoid Mode	0.0492	8.455×10^{-4}	-4.16×10^{-5} $\pm j\ 0.049226$
Wing Bending Mode	59.94	0.165	$-9.8719 \pm j\ 59.117$
Torsion	212.7	7.95×10^{-5}	$-0.0169 \pm j\ 212.7$

ZEROES:

	DESIGN A (SISO α)	DESIGN B (SISO θ)	DESIGN C (TITO)
Phugoid	8.913×10^{-5} $\pm j\ 0.0514$		
Wing Bending Mode	$-10.49 \pm j\ 59.30$	$-10.05 \pm j\ 59.05$	$-7.068 \pm j\ 65.04$
Wing Torsion Mode	$0.1106 \pm j\ 213.1$	$-0.0252 \pm j\ 212.8$	$-0.0267 \pm j\ 2.29$
	119.6	4.0859×10^{-4} -2.8304	-1.491×10^{-4}

identify: the low frequency phugoid mode at ~ 0.05 rad/s, the first wing bending mode at ~ 60 rad/s and the first wing torsion mode at ~ 213 rad/s. The fourth mode in more traditional airplanes, corresponds to the short period mode. The poles are at 7.308 and -11.918 rad/s. The unstable pole at 7.308 rad/s corresponds to the short period mode.

The phugoid mode is typically a low frequency lightly damped mode. It manifests itself as slowly varying speed with constant angle of attack over a long distance. When dealing with conventional aircraft, the short period mode is typically highly damped and at high frequency. It shows up at constant speed with varying angle of attack over a short distance. Figure 3.1 illustrates the short period and phugoid modes [17] of a conventional aircraft. The two flexible modes were described in Chapter 2.

There is an eigenvector associated with each eigenvalue. The modes of the system described by the eigenvectors govern the natural response of the system. Any motion can be described as a linear combination of the modes. One way of picturing the modes is to look at which state variables contribute to each eigenvector. In Figure 3.2 the components of the eigenvectors are shown as fractions of the total normalized to one. The actual eigenvectors are listed in Appendix 1.3. It should be recalled that the eigenvectors change with the scaling, thus the results of modal analysis may change with scaling.

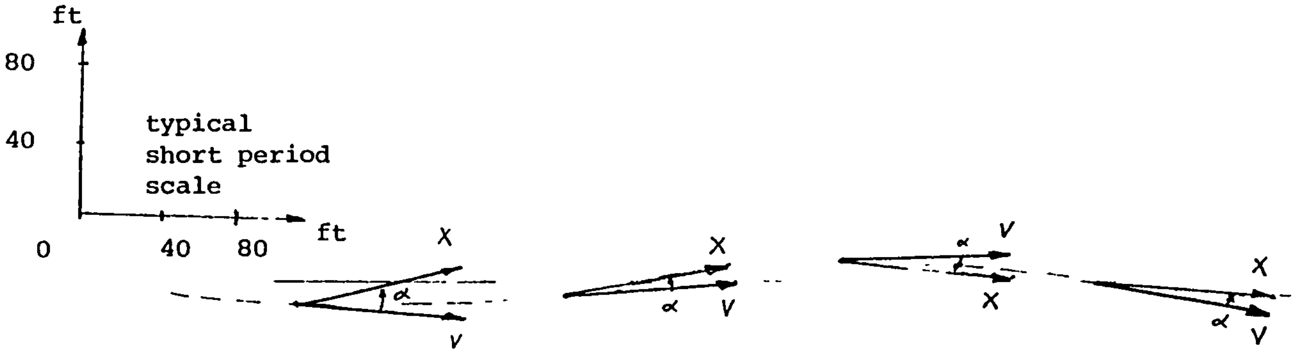

a. Short Period Mode constant speed with varying angle of attack and pitch attitude

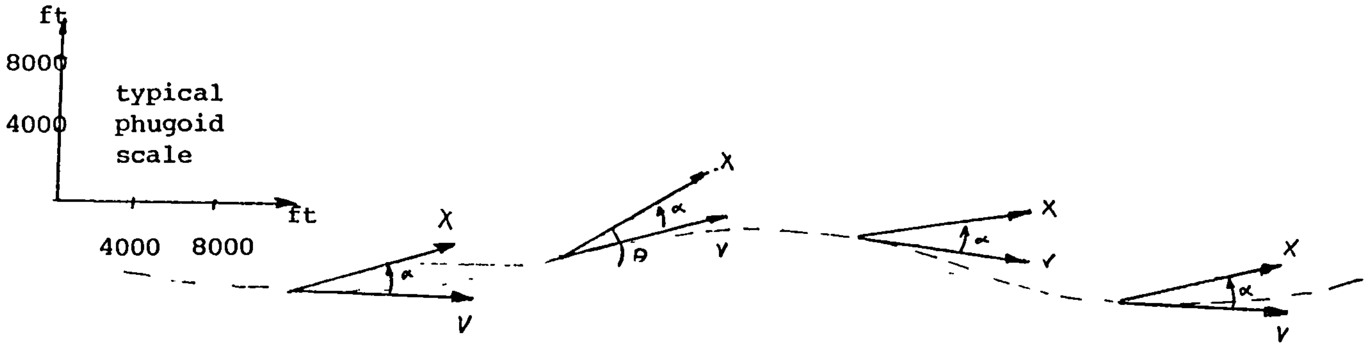

b. Phugoid Mode constant angle of attack with varying speed and pitch attitude

Figure 3.1 Phugoid and Short Period Modes [17]

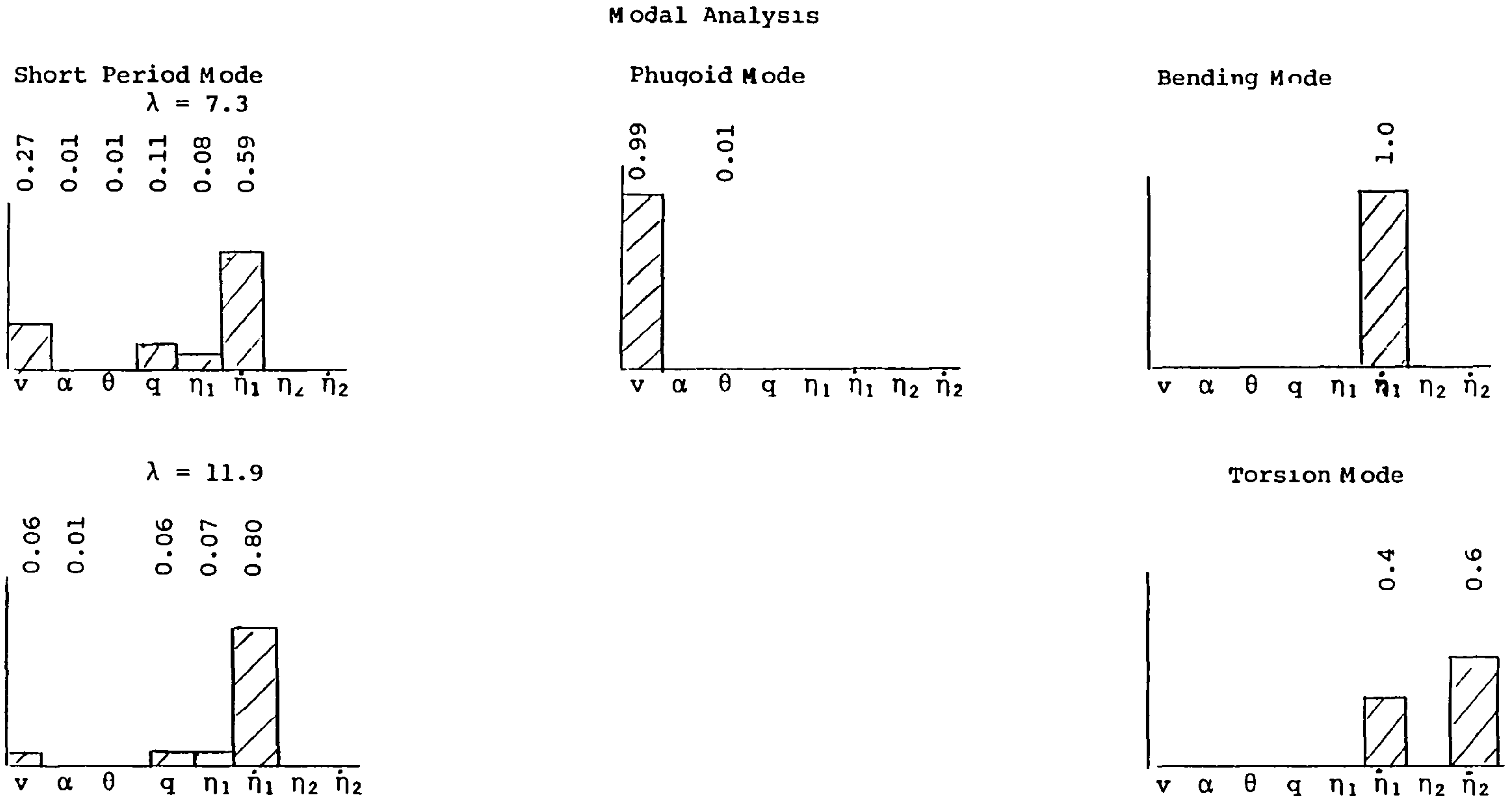

Figure 3.2 Modal Analysis of the scaled TITO truth model based on magnitude of eigenvectors normalized to unit length.

Figure 3.2 shows that the phugoid mode does indeed consist primarily of velocity components. The wing bending mode is primarily $\dot{N}_1$ and the torsion mode is a combination of $\dot{N}_1$ and $\dot{N}_2$. The so called short period mode is decoupled from the wing torsion mode, however it has a large component in $\dot{N}_1$ and smaller components in v, q, and N_1. This indicates the wing bending mode plays an important part in the rigid dynamics.

The system zeroes for the three truth models are also listed in Table 3.1. Since all the zeroes of Design Model C are in the left half plane, the system is minimum phase. This is important as it guarantees recovery with the LTR method. One of the zeroes is virtually at 0. This will cause problems with the DC performance; in order to have good steady state command following, the surfaces must continue to deflect until eventually they will saturate. The two pairs of complex zeroes are very close to complex poles corresponding to the flexible modes. Ths indicates that the flexible modes are unobservable when angle of attack and pitch attitude are the outputs.

Design Model A also has zeroes at the flexible modes. In addition, this system has a pair of zeroes at the phugoid mode and another zero in the right half plane at 120 rad/s. This indicates that the phugoid mode and both flexible modes are relatively unobservable when only angle of attack is output.

Design Model B has zeroes near the flexible modes. In addition it has two low frequency zeroes, one virtually at 0 and the other at 2.83 rad/s. In this system, the flexible modes are almost unobservable, but the phugoid mode is observable. The relative controllability and observability of the three design models is examined in more detail in the next section.

3.2.2 Controllability and Observability Analysis for Truth Design Models

One method of looking at controllability and observability is to diagonalize the system using a similarity transformation. The matrix of eigenvectors of $\underline{A}$ called $\underline{T}$ will cause $\underline{T}^{-1}\underline{AT}$ to be a diagonal matrix with the eigenvalues of $\underline{A}$ on the main diagonal.

The transformed system is

$$\dot{\underline{z}}(t) = (\underline{T}^{-1}\underline{AT})\underline{z}(t) + \underline{T}^{-1}\underline{Bu}(t) \tag{3.1}$$

$$\underline{y}(t) = \underline{CTz}(t) \tag{3.2}$$

thus the states of $\underline{z}(t)$ belong to easily identifiable modes. The columns of $\underline{T}^{-1}\underline{B}$ give the relative weights of the controllability of each mode using the corresponding control. The rows of $\underline{CT}$ give the relative observability. As with the modal analysis, the results of controllability and observability analysis are scale dependent.

Figure 3.3 is a bar-chart showing the observability and controllability of the modes of the scaled truth model. Figure 3.3a shows that the wing bending mode is the most easily controlled using the flaperon and the short period

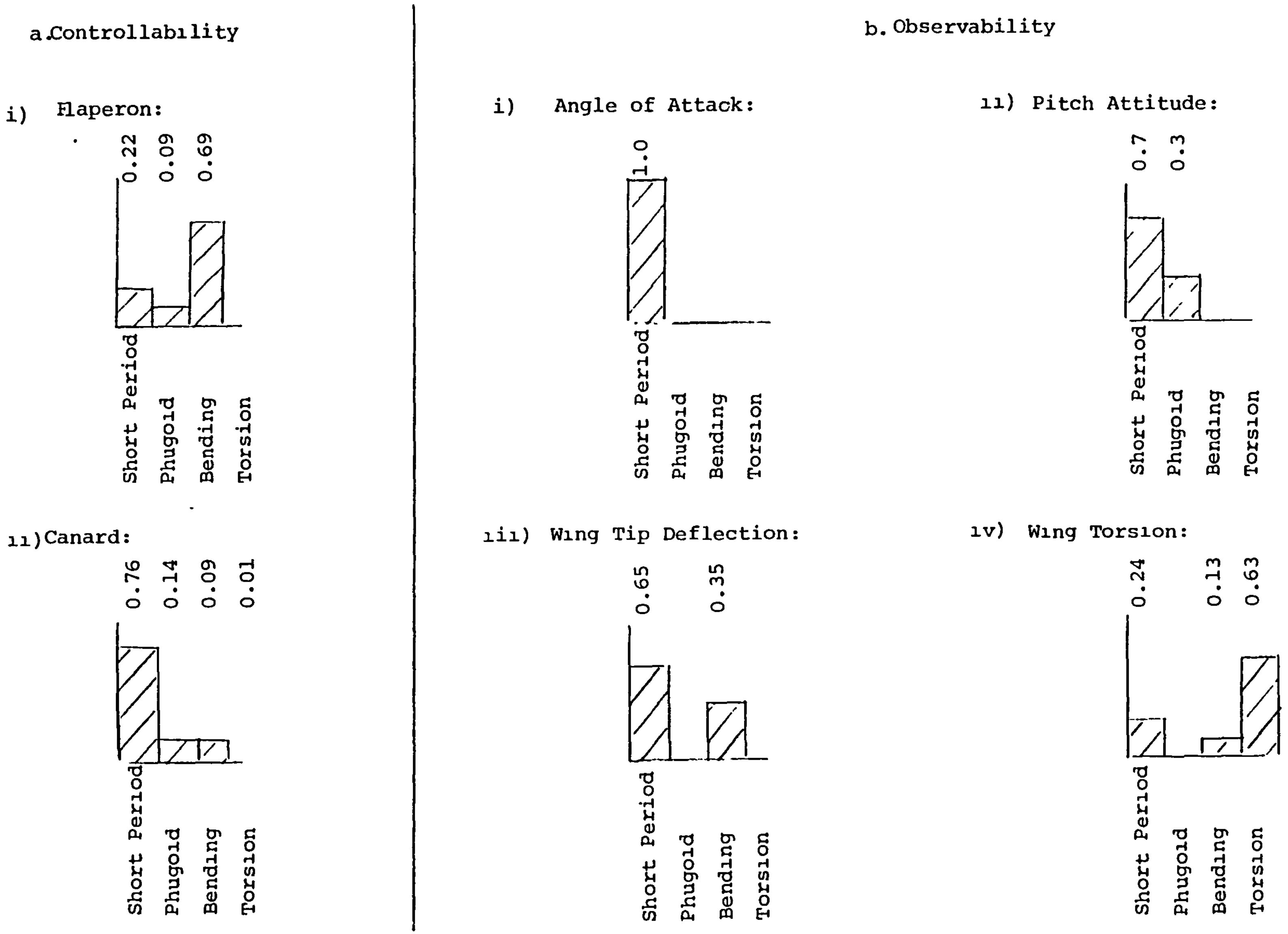

Figure 3.3 Controllability and Observability Analysis of Truth Model
a. Controllability: i) flaperon control ii) canard control
b. Observability Outputs: i) angle of attack ii) pitch attitude
iii) wing tip deflection iv) wing torsion
height of bar corrseponds to relative controllability or observability of particular mode with indicated control or output

mode is the most easily controlled using the canard. This suggests a possible output configuration of either pitch or angle of attack and wing tip bending rate in which flaperon control could be used effectively. The phugoid mode is somewhat controllable with either the flaperon or the canard as indicated in 3.3a. The wing torsion mode is virtually uncontrollable.

The observability analysis in Figure 3.3b shows that the short period mode shows in the angle of attack, pitch attitude, wing bending and wing torsion. The phugoid mode only shows up in pitch attitude.

3.2.3 Open Loop Frequency Response of Truth Model

The SISO system frequency response is often represented with a Bode plot. The frequency response for multivariable systems is usually represented by a singular value plot. Figures 3.4, 3.5, and 3.6 are the frequency responses of the three systems we are interested in. Design Model A is the SISO system with canard input and angle of attack output. The scaled and unscaled Bode magnitude plots for the open loop truth model of this system are shown in Figures 3.4 a & b. The SISO system with canard input and pitch attitude output will be referred to as Design Model B. Figure 3.5 shows the Bode magnitude plot for the scaled and unscaled open loop truth model. The TITO design model, with canard and flaperon as controls and pitch attitude and

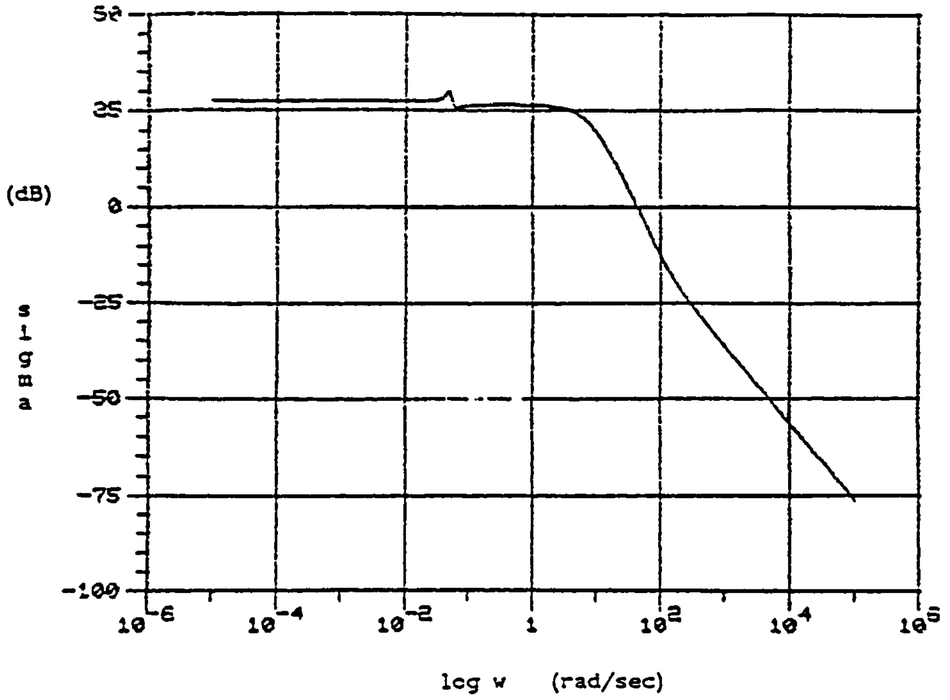

a. Scaled Aircraft Truth Model

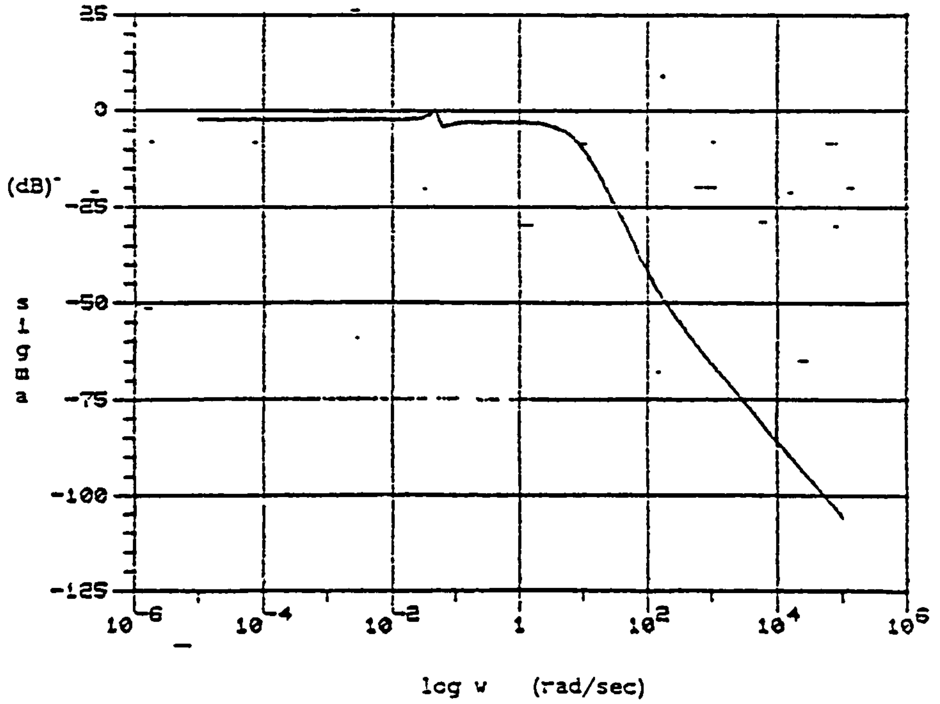

b. Unscaled Aircraft Truth Model

Figure 3.4 Design Model A: Open Loop Bode Magnitude Plot

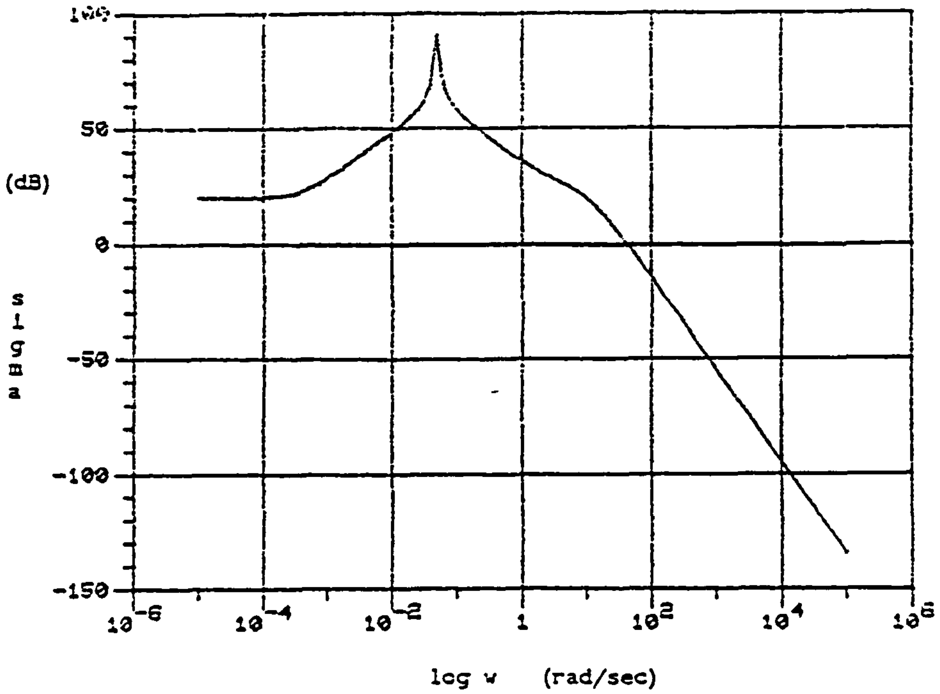

a. Scaled Aircraft Truth Model

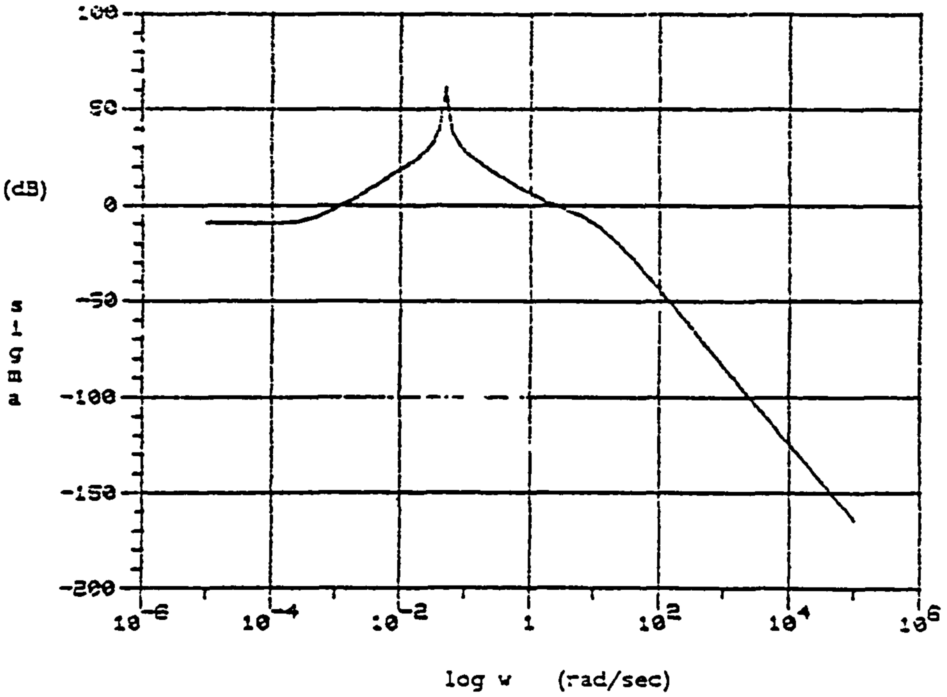

b. Unscaled Aircraft Truth Model

Figure 3.5 Design Model B: Open Loop Bode Magnitude Plot

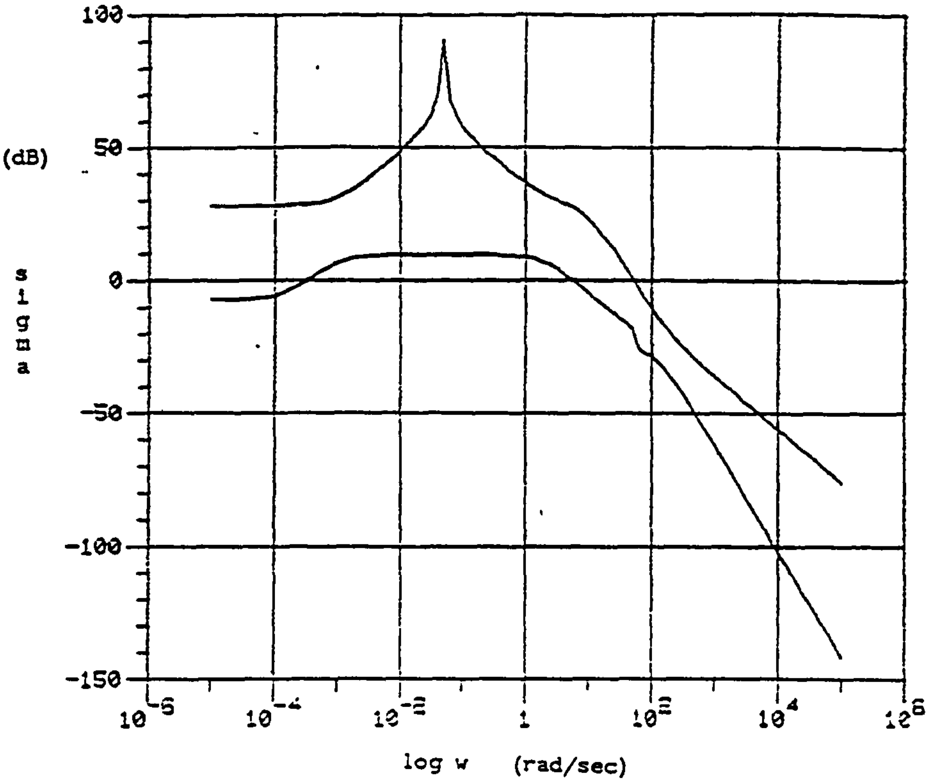

a. Scaled Aircraft Truth Model

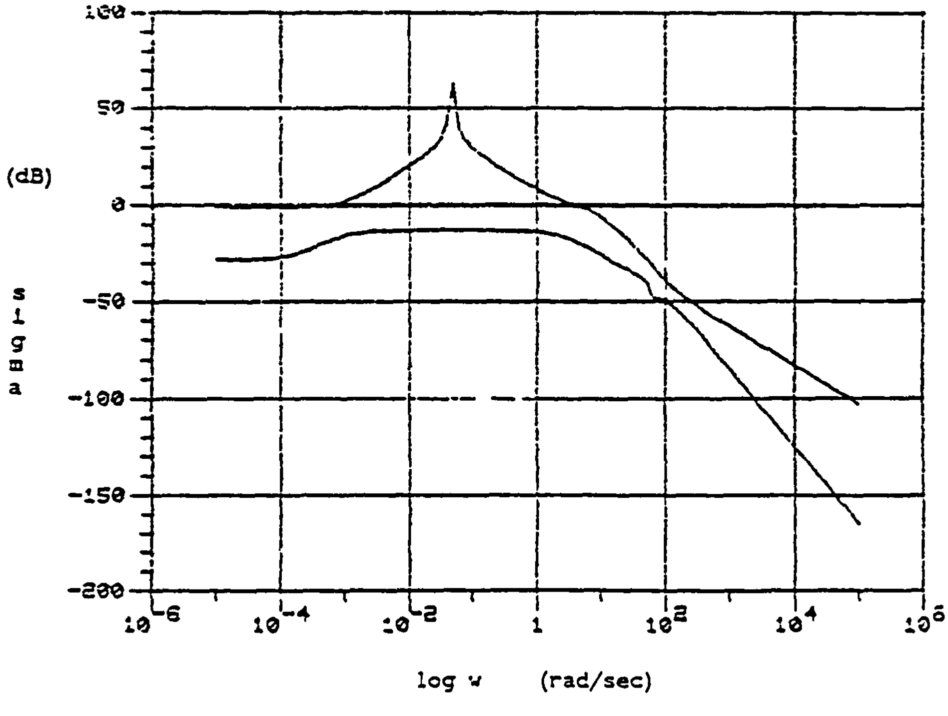

b. Unscaled Aircraft Truth Model

Figure 3.6 Design Model C: Open Loop Singular Value Plot angle of attack as outputs is Design C. The open loop singular values of its scaled and unscaled truth model are shown in Figures 3.6 a & b respectively.

There are several things to note from these plots. First, there is the comparison between the scaled and unscaled systems. The scaling has not changed the shape, it has merely increased the overall gain. Second, at low frequency all three systems have constant gains -- there are no integrators. Third, at $w \sim 10^{-4}$ rad/sec, the minimum singular value of Design C and the gain of Design B start increasing due to the low frequency zero. The peak that shows up at $w \sim 0.05$ rad/sec particularly in Design B, Figure 3.5, and the maximum singular value of Design C, Figure 3.6, corresponds to the lightly damped phugoid mode. The bump near $w \sim 60$ rad/sec is due to the first bending mode. There are two poles between the frequencies 5 and 15 rad/sec due to the short period mode. This accounts for the corner at $w \sim 10$ rad/sec.

3.2.4 Singular Value Decomposition for Design Model C

The singular value decomposition provides directional information. Essentially, the plant model can be diagonalized so that the inputs map to the outputs through the singular values.

The original system may be written

$$\underline{y}(s) = \underline{G}(s)\underline{u}(s) \tag{3.3}$$

where

$\underline{y}(s)$ = output vector

$\underline{u}(s)$ = input vector

$\underline{G}(s)$ = transfer matrix

The matrix $\underline{G}(s)$ can be decomposed, at a given frequency, such that

$$\underline{G}(jw) = \underline{U}(jw)\underline{\Sigma}(jw)\underline{V}^H(jw) \tag{3.4}$$

where $\underline{U}(jw)$ is the matrix of left singular vectors and $\underline{V}(jw)$ is the matrix of right singular vectors. $\underline{\Sigma}(jw)$ is a diagonal matrix with the singular values of $\underline{G}(jw)$ on its main diagonal.

Thus, at a given frequency,

$$\underline{y}(jw) = \underline{U}(jw)\ \underline{\Sigma}(jw)V^H(jw)\underline{u}(jw) \tag{3.5}$$

$$\underline{U}^{-1}(jw)\underline{y}(jw) = \underline{\Sigma}(jw)\underline{V}^H(jw)\underline{u}(jw) \tag{3.6}$$

The decoupled system has inputs $\underline{V}^H(jw)\underline{u}(jw)$ related to outputs $\underline{U}^{-1}(jw)\underline{y}(jw)$ through the diagonal matrix $\underline{\Sigma}(jw)$.

Let the input $\underline{u} = \underline{v}_i$, the i^{th} right singular vector of $\underline{G}(jw)$, then

$$\underline{y}_i = \underline{U}(jw)\underline{\Sigma}(jw)\underline{V}^H(jw)\underline{v}_i = \sigma_i\ \underline{u}_i \tag{3.7}$$

where $\underline{u}_i$ is the i^{th} left singular vector. This means that if the input is in the direction of the right singular vector associated with the maximum singular value, the output will have an amplification of the maximum singular value and be in the direction of the associated left singular vector.

At DC, in two dimensions this is easy to visualize since the vectors are real and the geometry is planar. Figure 3.7a shows graphically the singular value decomposition of the scaled and unscaled TITO Design Model C at DC. The inputs are the actuator deflections and the outputs are angle of attack and pitch attitude. The inputs are in a unit circle. The directions associated with the maximum and minimum singular values are shown. The outputs are an ellipse whose major axis corresponds to the length of the maximum singular value and is in the associated left singular vector. The minor axis is in the direction of the left singular vector associated with the minimum singular value. All the singular value decomposition matrices are listed in Appendix 1.4.

Figure 3.7 a and b shows that the maximum amplification direction is primarily in the canard direction and angle of attack direction at DC. The scaling changes the direction of the input somewhat. The maximum amplification direction is more in the canard direction for the scaled system than the unscaled system. By scaling the deflections such that the range of deflections are comparable, the canard and flaperon are being compared on the basis of fraction of deflection rather than degree for degree. This is a more meaningful comparison. The canard is a more effective actuator.

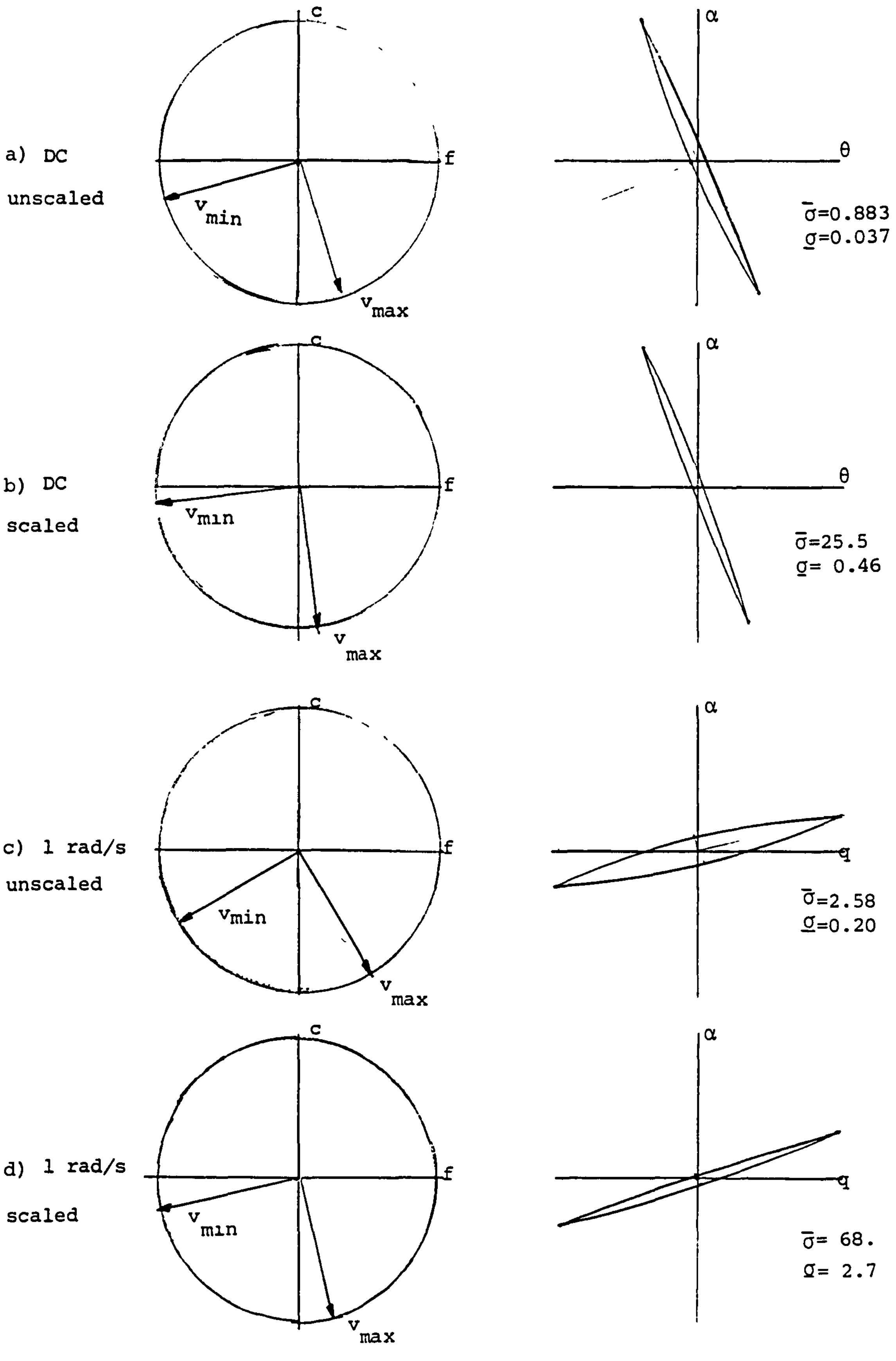

a) DC unscaled

b) DC scaled

c) 1 rad/s unscaled

d) 1 rad/s scaled

Figure 3.7 Singular Value Decopmposition
scaled maximum singular value to unit length

We also wanted to examine the singular values at a frequency above DC. However, the graphical interpretation is not as straight forward since the transfer matrix is complex. At w = 1 rad/sec, Design Model C transfer function matrix is primarily imaginary; the system with angle of attack and pitch rate output is primarily real. Since we are mainly interested in a qualitative examination of the singular value decomposition, the real part of the singular vectors of the system with angle of attack and pitch rate output at w = 1 rad/sec was plotted in Figure 3.7 c and d.

As can be seen from Figure 3.7 c and d, the direction of the input associated with the maximum singular value at w = 1 rad/sec is virtually unchanged from the system at DC. The maximum amplification direction in the output space is quite different; whereas it was predominantly in the angle of attack direction at DC, it is almost entirely in the pitch rate direction at w = 1 rad/sec.

3.3 Model Error

3.3.1 Multiplicative Error

It is very difficult to quantify modelling errors, however an estimate of the size and directionality of the model errors is necessary in order to design robust control systems that remain stable in the presence of model errors. Reference 18 contains a detailed derivation of robustness measures for multivariable systems. A brief explanation of multiplicative error will be given here.

Figure 3.8 is a block diagram of the true plant, $\tilde{\underline{G}}$, broken into components $\underline{G}$, the plant model, and $\underline{E}$, the multiplicative error.

The true plant may be expressed as

$$\tilde{\underline{G}}(s) = (\underline{I}+\underline{E}(s))\underline{G}(s), \tag{3.8}$$

which may be rearranged to give

$$\underline{E}(s) = (\tilde{\underline{G}}(s)-\underline{G}(s))\underline{G}^{-1}(s) \tag{3.9}$$

assuming $\underline{G}^{-1}(s)$ exists. This is an explicit expression for $\underline{E}(s)$ using the true plant and the reduced plant models.

Once the error is established, the multiplicative robustness test, derived in Reference 11 may be applied:

$$\underline{\sigma}\ [\underline{I}+\underline{G}^{-1}(s)] > \ \bar{\sigma}\ [\underline{E}(s)];\ s = jw \tag{3.10}$$

The same test in a slightly different form is

$$\bar{\sigma}\ [\underline{I}+\underline{G}^{-1}(s)]^{-1} < \ \underline{\sigma}\ [E(s)^{-1}];\ s = jw. \tag{3.11}$$

This requires that the maximum singular value of the closed loop transfer function matrix be less than the minimum singular value of the inverse of the multiplicative error at all frequencies.

Figure 3.9 is a sketch of the singular value plots of a typical plant $\underline{G}(s)$, the return difference $(\underline{I}+\underline{G}(s))$ and the closed loop transfer function matrix $(\underline{I}+\underline{G}(s)^{-1})^{-1}$.

The multiplicative error does not depend on the compensator. Figure 3.8b shows the plant, compensator and

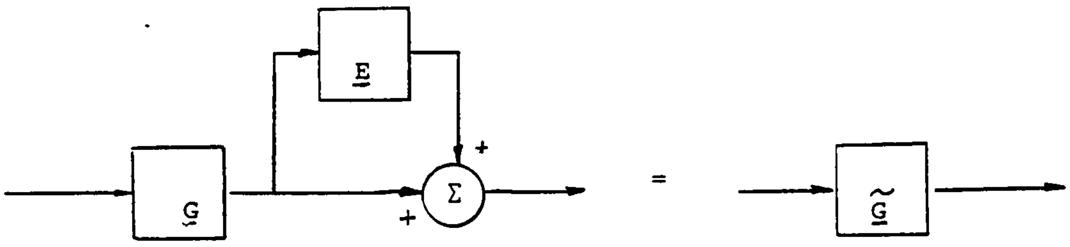

a. Block diagram of Multiplicative Error

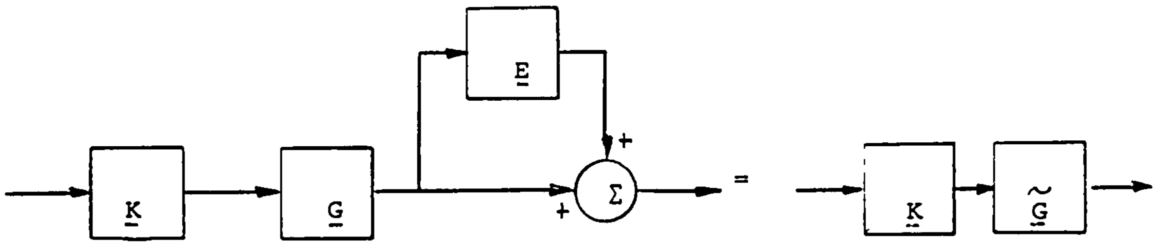

b. Block diagram of Multiplicative Error including compensator

Figure 3.8 Block Diagram of true plant modeled as plant with error for compensated and uncompensated system.

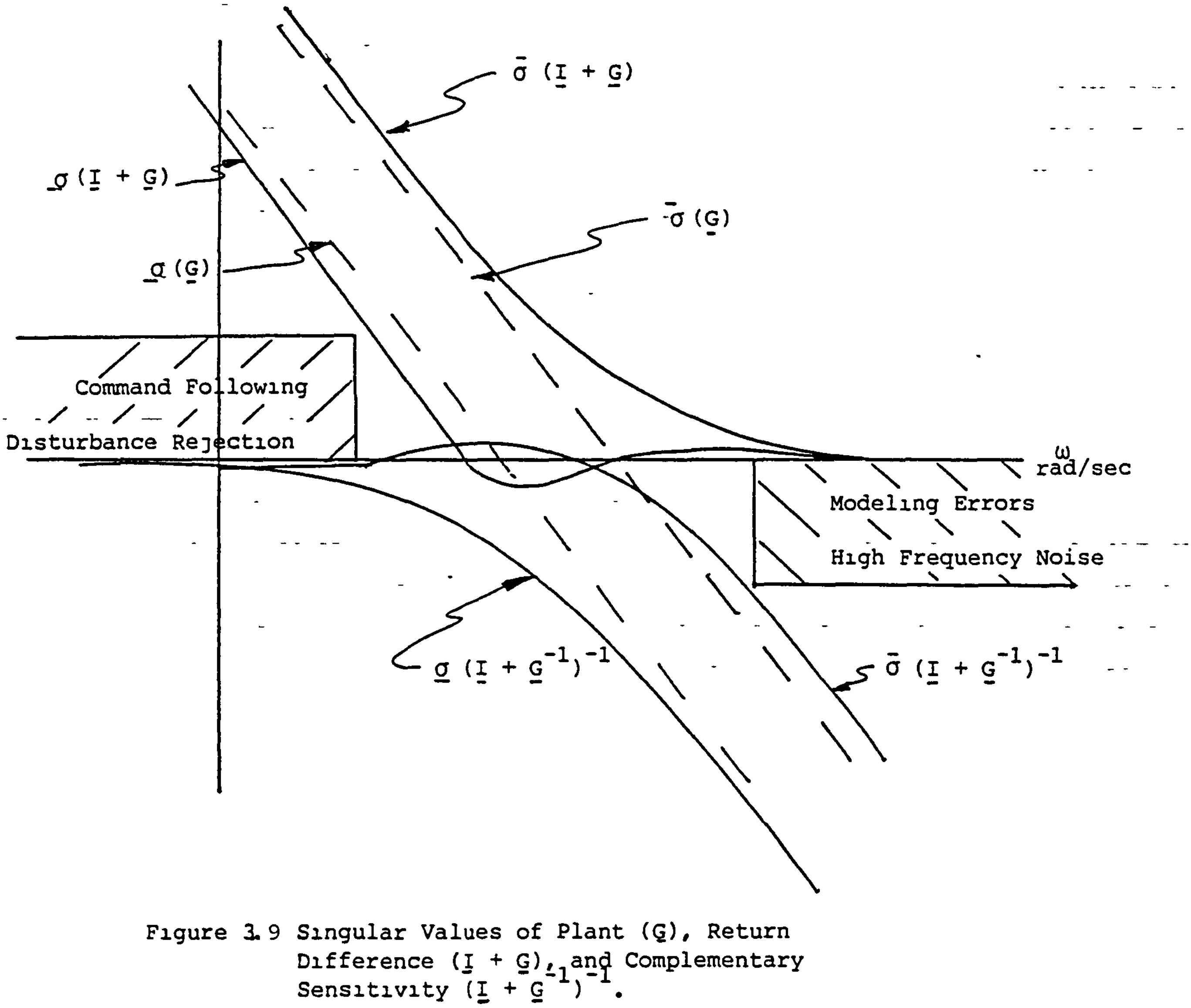

Figure 3.9 Singular Values of Plant ($\underline{G}$), Return Difference ($\underline{I} + \underline{G}$), and Complementary Sensitivity ($\underline{I} + \underline{G}^{-1})^{-1}$.

multiplicative error. Based on Figure 3.8b, the multiplicative error is

$$\underline{E}(s) = (\underline{\tilde{G}}(s)\underline{K}(s) - \underline{G}(s)\underline{K}(s))(\underline{G}(s)\underline{K}(s))^{-1}$$
$$= (\underline{\tilde{G}}(s)-\underline{G}(s))\underline{G}(s)^{-1}, \qquad (3.12)$$

which is the same as Eqn 3.9. This $\underline{E}(s)$ must be compared to $[\underline{I}+(\underline{G}(s)\underline{K}(s)^{-1}]^{-1}$ since the closed loop transfer function matrix does depend on the compensator.

3.3.2 Model Error

There are many possible sources of error in a linear model. Typically, the model is fairly accurate at low frequency, but the high frequency dynamics are not as well modelled and are often unmodelled.

In this study, the linear model from Reference 7 with the cg in its center position will be considered the truth model. The reduced model will be the truth model without the torsion mode. Table 3.2 presents the poles and zeroes of the truth model and the reduced model for all three designs.

Figure 3.10 shows the singular value plots of $\underline{E}(jw)^{-1}$ which was calculated using Eqn 3.9. All three plots exhibit a valley at the phugoid frequency $w \sim 0.05$ rad/sec, which is due to the slight difference in the poles of the two models at that frequency. The other valley at the wing torsion mode frequency is as expected, due to ignoring that mode in the reduced models.

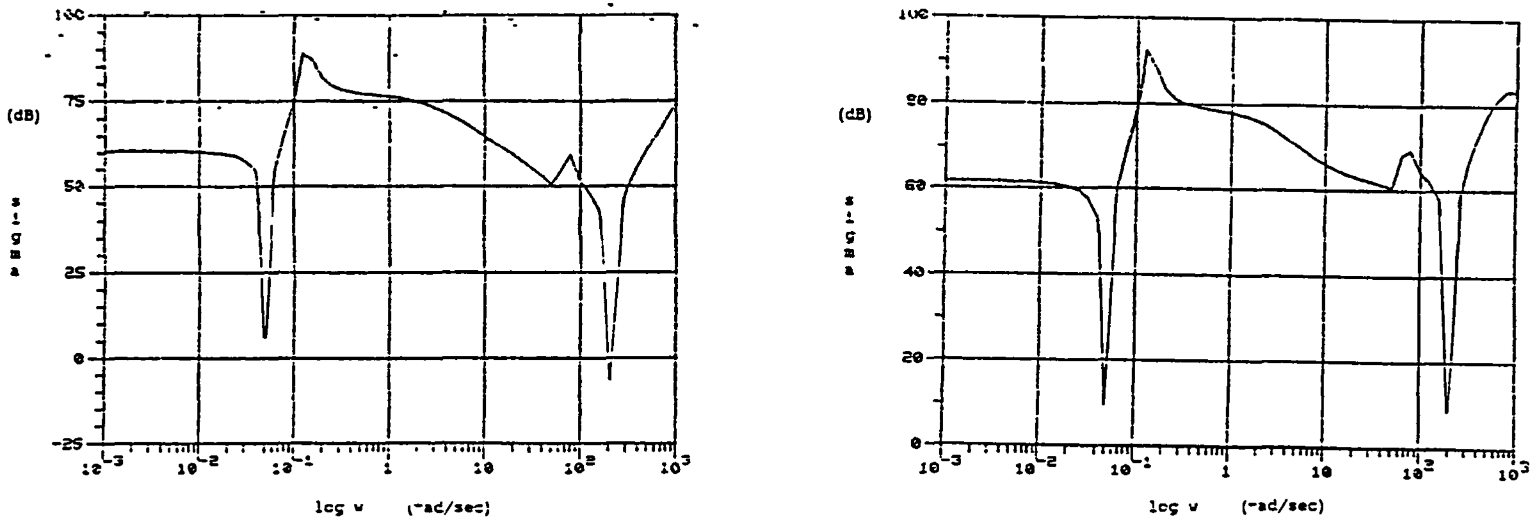

a. Design A

b. Design B

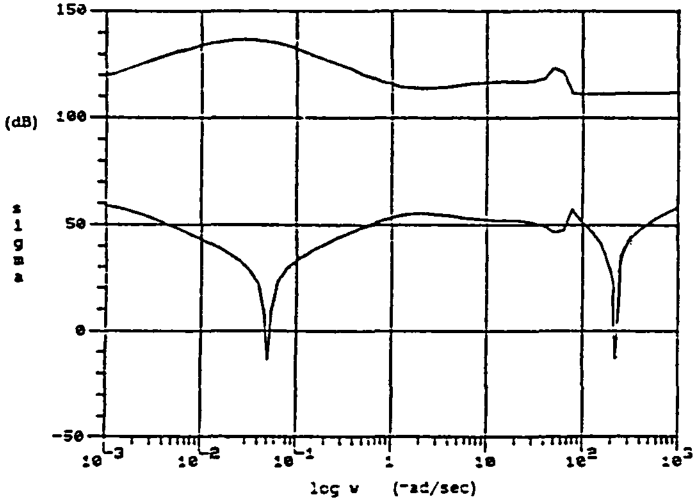

c. Design C

Figure 3.10 Inverse Model Error Reflected at the Plant Output $\underline{E}_{out}(s)^{-1}$

TABLE 3.2
POLES AND ZEROES FOR
REDUCED MODELS VS TRUTH MODELS

POLES:

	TRUTH MODEL	REDUCED MODEL
Short Period Mode	7.3079 -11.918	7.3067 -11.912
Phugoid Mode	-4.1596×10^{-5} $\pm j\ 0.049226$	-4.1673×10^{-5} $\pm j\ 0.049209$
Bending Mode	$-9.8719 \pm j\ 59.17$	$-9.8730 \pm j\ 59.118$
Torsion Mode	$-0.016946 \pm j\ 212.7$	

ZEROES:

DESIGN A (SISO α)		DESIGN B (SISO θ)	
TRUTH MODEL	DESIGN MODEL	TRUTH MODEL	DESIGN MODEL
119.6	119.9	4.0859×10^{-4}	4.077×10^{-4}
$-8.913\ C\ 10^{-5}$ $\pm j\ 0.0514$	-8.832×10^{-5} $\pm j\ 0.0514$	-2.830	-2.831
-10.49 $\pm j\ 59.30$	-10.52 $\pm j\ 59.28$	-10.05 $\pm j\ 59.05$	-10.05 $\pm j\ 59.04$
0.1106 $\pm j\ 213.1$		-0.0252 $\pm j\ 212.8$	

DESIGN C (TITO)	
TRUTH MODEL	DESIGN MODEL
$-7.068 \pm j\ 65.04$	$-7.076 \pm j\ 65.03$
$-0.0267 \pm j\ 212.9$	
$-1.491\ \ 10^{-4}$	-1.490×10^{-4}

3.4 Design Specifications

The design specifications will be based on the aircraft capabilities as reflected in the linear model. In order to have a basis for comparison, Designs A, B, and C will be designed to the same specifications.

The design specifications are based on three types of requirements: good command following, disturbance rejection where the disturbance is wind gusts, and stability robustness considerations to model errors.

First we will address the command following requirement. Due to the low frequency zero, it seems unreasonable to require zero steady state error. The accuracy requirement is that in the frequency range $0.01 < w < 1$ rad/sec the error must be less than 10% of the reference input. This requires the maximum singular value (or the Bode gain) of the sensitivity matrix, $[\underline{I}+\underline{G}(s)\underline{K}(s)]^{-1}$, be smaller than -20 db for $0.01 < w < 1$ rad/sec. This specification can be approximated by the loop transfer matrix, $\underline{G}(s)\underline{K}(s)$, requiring its minimum singular value be greater than 20 db for $0.01 < w < 1$ rad/sec.

The second issue is disturbance rejection. Typical wind gust disturbances are in the low frequency range, less than 1 rad/sec. Good disturbance rejection requires that the sensitivity matrix $[\underline{I}+\underline{G}(s)\underline{K}(s)]^{-1}$ be "small"; or equivalently $[\underline{I}+\underline{G}(s)\underline{K}(s)]$ be large. For this design we will require disturbance be attenuated by a factor of 1.5 for frequencies below 1 rad/sec. Again, this requirement can be approximated using the loop transfer matrix, $\underline{G}(s)\underline{K}(s)$. In this case, the minimum singular value of the loop transfer matrix $\underline{G}(s)\underline{K}(s)$ (or the Bode gain) must be greater than 3.5 db for $w < 1$ rad/sec.

Finally, we will consider robustness requirements. The minimum crossover frequency, dictated by the unstable pole, is 7.3 rad/sec. The bandwidth of the system should be less than 60 rad/sec in order to avoid exciting the wing bending mode. In addition, the model error shown in Figure 3.10 shows the large downward spike at the wing torsion mode. The closed loop frequency response $(I+[\underline{G}(s)\underline{K}(s)]^{-1})^{-1}$ should have its maximum singular value less than -20 db at $w \sim 200$ rad/sec for the TITO design. The robustness requirements for the SISO designs are

$$\bar{\sigma}\,(\underline{I}+[\underline{G}(s)\underline{K}(s)]^{-1})^{-1} < \begin{cases} -10 \text{ db} & \text{Design A} \\ & \text{(SISO } \alpha) \\ 10 \text{ db} & \text{Design B} \\ & \text{(SISO } \theta) \end{cases}$$

for $w > 200$ rad/sec.

Figure 3.11 shows the performance, disturbance rejection and robustness boundaries for the loop transfer function. It should be noted that the requirements are consistent; if the minimum singular value is falling at -20 db/decade and is 20 db at $w = 1$ rad/sec, the bandwidth will be 10 rad/sec which is larger than the unstable pole. The requirement that the maximum singular value crossover before 60 rad/sec imposes a maximum separation requirement on the singular values.

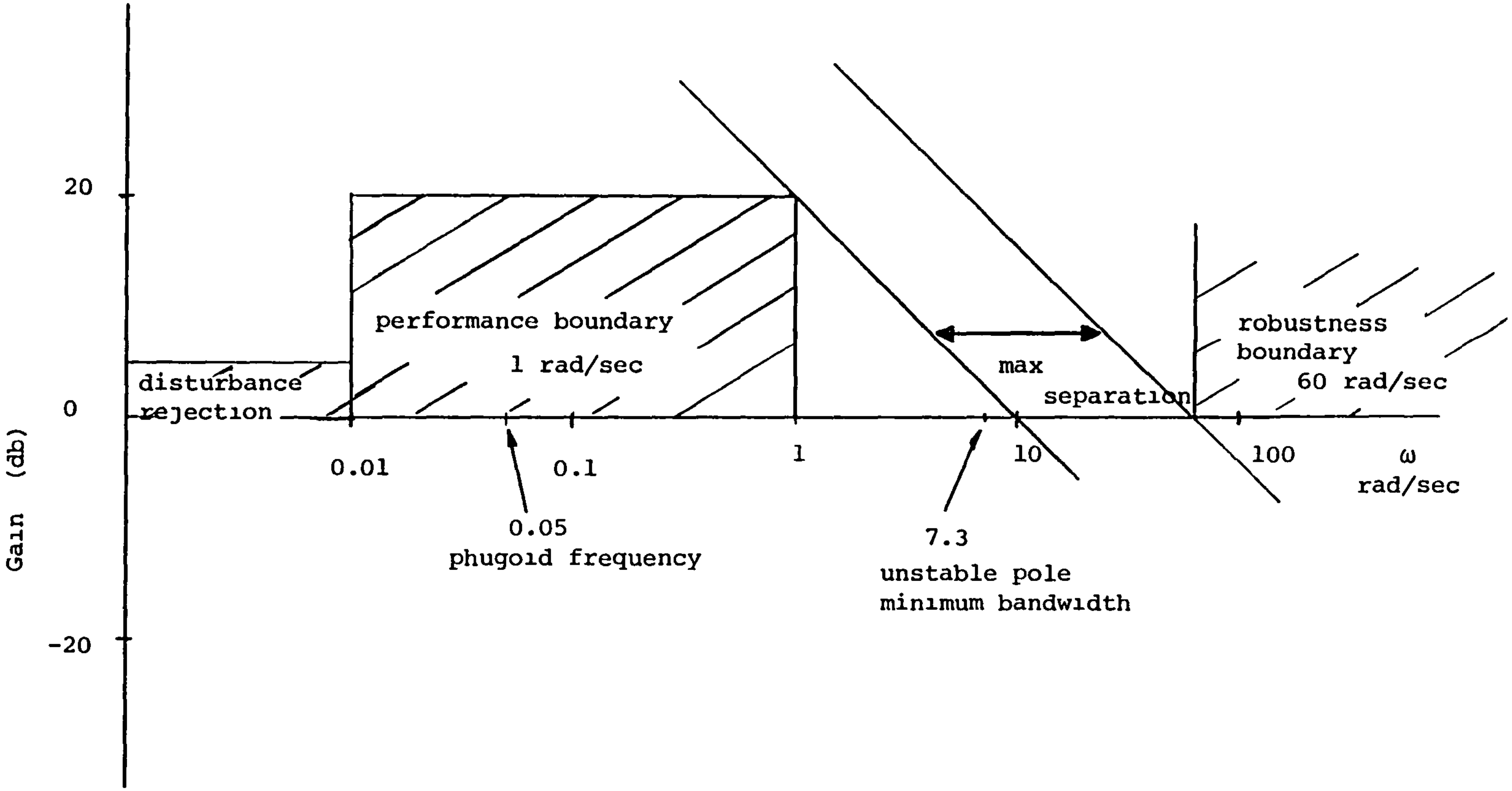

Figure 3.11 Frequency response desired to meet specifications
approximate requirements on $\underset{\sim}{G}(s)\underset{\sim}{K}(s)$

3.5 Summary

This chapter started with a linear model, applied the methods useful in understanding the model, and based on that understanding developed reasonable design specifications. The important things learned were the identity of the modes, the location of the unstable pole and the existence of the very lightly damped phugoid mode. In addition, the low frequency zero gave an indication of potential poor DC performance. Finally, the singular value decomposition and the transfer matrix showed that the canard has more command authority than the flaperon. The flaperon has somewhat more command authority at 1 rad/s than at DC.

The next step was to evaluate the multiplicative error based on the truth model and the design model. This highlighted the problem with the very lightly damped, low frequency phugoid mode. The design specifications were formed, based on the desired performance and aircraft dynamics.

CHAPTER 4: LQG/LTR DESIGNS

4.1 Introduction

The goal in this chapter is to design a compensator which uses the flaperon and canard to independently control angle of attack and pitch attitude. The system must meet the specifications given in Chapter 3. As a preliminary step two single-input-single-output (SISO) controllers will be designed, one for angle of attack output and canard input, the so called Design A. The other for pitch attitude output and canard input, Design B. These two systems will be used to give insight into the two-input-two-output (TITO) control problem which is Design C. The three controllers will be designed to meet essentially the same specifications. Their time-domain performance will be compared in the next chapter in order to establish the usefulness of the flaperon in this configuration.

Section 4.2 contains a brief review of the LQG/LTR method. The SISO designs are described in Section 4.3. The TITO design is explained in Section 4.4. Section 4.5 contains a discussion of the three designs.

4.2 Review of the LQG/LTR Design Method

The LQG/LTR method is described much more thoroughly in References 12 and 21; only a brief description is given here. The compensator is based on the plant model. Figure 4.1 shows the structure of the plant and compensator. The designer controls the gain matrix $\underline{G}$ and the filter matrix $\underline{H}$.

The design plant model is:

$$\underline{\dot{x}}(t) = \underline{A}\,\underline{x}(t) + \underline{B}\,\underline{u}(t) \qquad (4.1)$$

$$\underline{y}(t) = \underline{C}\,\underline{x}(t)$$

$$\underline{G}(s) = \underline{C}(sI-\underline{A})^{-1}\underline{B} \qquad (4.2)$$

The LQG compensator model is:

$$\underline{K}(s) = \underline{G}(sI-\underline{A} + \underline{B}\,\underline{G} + \underline{H}\,\underline{C})^{-1}\,\underline{H} \qquad (4.3)$$

According to the LTR theory,

$$\sigma_i\ [\underline{G}(jw)\underline{K}(jw)] \longrightarrow \sigma_i\ [\underline{C}(jw\underline{I}-\underline{A})^{-1}\underline{H}] \qquad (4.4)$$

as $q \rightarrow \infty$ for fixed $\underline{H}$ and

$$\underline{G} = \underline{R}^{-1}\,\underline{B}^T\underline{K} \qquad (4.5)$$

where $\underline{K}$ is the solution to the control algebraic Ricatti equation (CARE):

$$\underline{K}\,\underline{A} + \underline{A}^T\underline{K} + q\underline{C}^T\underline{C} - \underline{K}\,\underline{B}\,\underline{R}^{-1}\underline{B}^T\underline{K} = \underline{0} \qquad (4.6)$$

with $\underline{R} = \underline{I}$ and a minimum phase system.

Thus if $\underline{C}(jw\underline{I}-\underline{A})^{-1}\underline{H}$ has the desired loop shape, the gain matrix can be designed so that $\underline{G}(s)\underline{K}(s)$ has the same loop shape. $\underline{H}$ can be designed using the Kalman filter where

$$\underline{H} = \underline{\Sigma C}^T\,\underline{\Xi}^{-1} \qquad (4.7)$$

such that $\underline{\Sigma}$ is the solution to the filter algebraic Ricatti equation (FARE):

$$\underline{\Sigma A} + \underline{A}^T\underline{\Sigma} + LL^T - \frac{1}{\mu}\,\underline{C}^T\underline{C} = \underline{0}, \qquad (4.8)$$

and

$$\sigma i\ [\underline{C}(s\underline{I}-\underline{A})^{-1}\underline{H}] \cong \frac{1}{\mu}\ \sigma i\ [\underline{C}(s\underline{I}-\underline{A})^{-1}\underline{L}] \qquad (4.9)$$

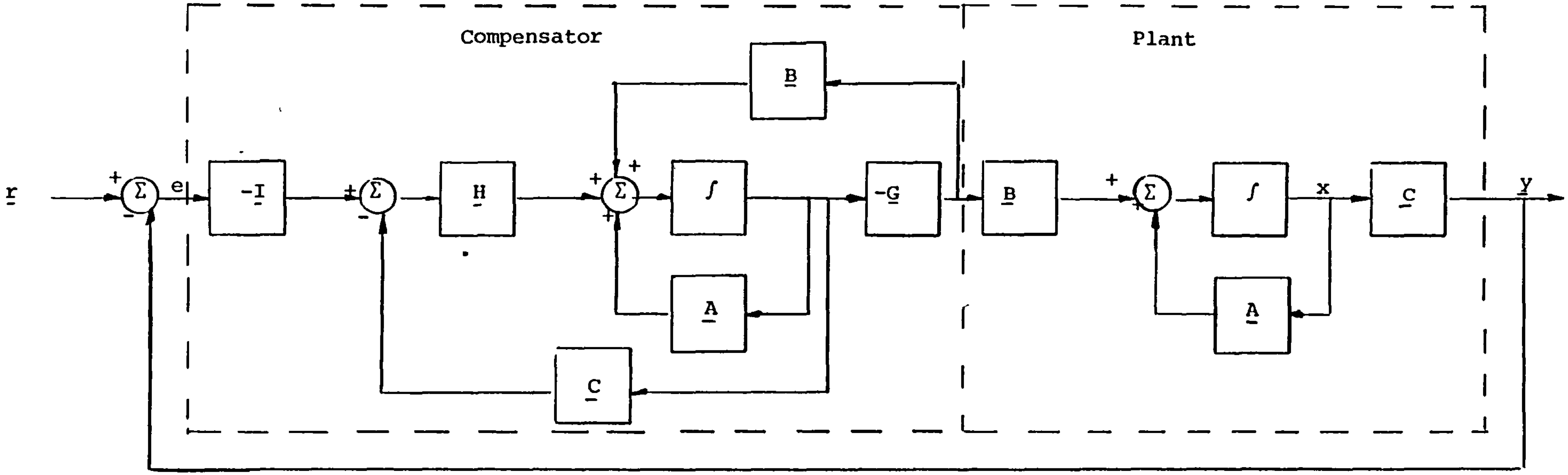

Figure 4.1 Structure of Model-Based Compensator

Thus the problem of designing $\underline{G}$ and $\underline{H}$ reduces to shaping the singular values of $\frac{1}{\mu}\,\underline{C}(s\underline{I}-\underline{A})^{-1}\underline{L}$ by selecting $\underline{L}$ and μ and using the FARE. Then using CARE with q large enough to recover $\underline{C}(s\underline{I}-\underline{A})^{-1}\underline{H}$.

A step-by-step procedure applicable to both SISO and MIMO design is:

1) Choose $\underline{L}$ and μ such that

   $\frac{1}{\mu}\sigma i\ [\underline{C}\ (sI-\underline{A})^{-1}\underline{L}]$ meets

   the specifications.

2) Use FARE to solve for

   $\underline{H} = \frac{1}{\mu}\ \underline{\Sigma}\,\underline{C}^T$

   $\sigma_i\ [\underline{C}(sI-\underline{A})^{-1}\underline{H}]$ should meet the

   the desired specifications.

3) Use CARE with $\underline{Q} = q\ \underline{C}^T\underline{C}$ and $\underline{R} = \underline{I}$ to solve for $\underline{G} = \underline{R}^{-1}\ \underline{B}^T\underline{K}$.

4) Examine singular values of $\underline{G}(jw)\underline{K}(jw)$ to insure q is large enough to recover and that the singular values of $\underline{G}(jw)\underline{K}(jw)$ meet the specifications.

4.3 Single-Input-Single-Output Designs

4.3.1 Design A: Angle of Attack Output

The basic four steps described in the previous section were followed in the designs presented here. The truth model is the linear model which includes the wing torsion mode. The design model is the scaled version of the original model without the wing torsion mode. The only actuator used for this design is the canard. Angle of attack is the controlled output. Table 4.1 lists the open loop poles and zeroes of the design model. Since one of the zeroes is not minimum phase, recovery is not guaranteed.

TABLE 4.1

DESIGN MODEL A OPEN LOOP POLES & ZEROES

Open Loop Poles:

$-4.16 \times 10^{-5} \pm j\,0.0492$ $\quad -9.873 \pm j\,59.12$ $\quad -11.9$ $\quad 7.31$

Open Loop Zeroes:

$-8.83 \times 10^{-5} \pm j\,0.0514$ $\quad -10.52 \pm j\,59.28$ $\quad 119.9$

Following the steps in Section 4.2:

1) Select $\underline{L} = \underline{B}$ and $\mu = 1$

2) Solve for $\underline{H}$. The magnitude of $\underline{C}\,(s\underline{I}-\underline{A})^{-1}\underline{H}$ is shown in Figure 4.2a. The bandwidth is 60 rad/sec and the gain is 27 db at $w = 1$ rad/sec, thus the design specifications are met.

3) Solve for $\underline{G}$, with $q = 10^4$. The $\underline{G}$ and $\underline{H}$ matrices are given in Appendix 2.1. Figure 4.2b is a plot of the Bode magnitude of the compensator $\underline{K}(s)$.

4) Examine the singular values of $\underline{G}(s)\underline{K}(s)$. Since the true plant, $\tilde{\underline{G}}(s)$, is available, Figure 4.2c is a plot of the gain of $\tilde{\underline{G}}(s)\underline{K}(s)$. Perfect recovery was not achieved, however the resulting loop does meet the specifications. The crossover frequency is 40 rad/sec and

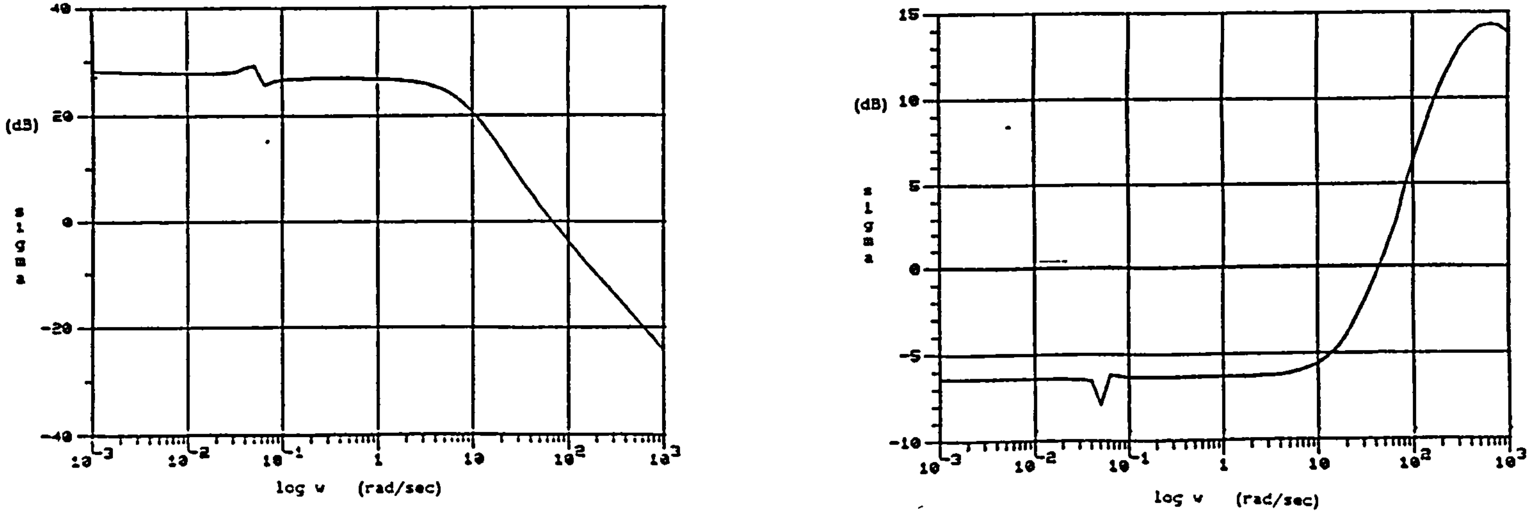

a. Target Loop: $\underline{C}(s\underline{I}-\underline{A})^{-1}\underline{H}$

b. Compensator Loop: $\underline{K}(s)$

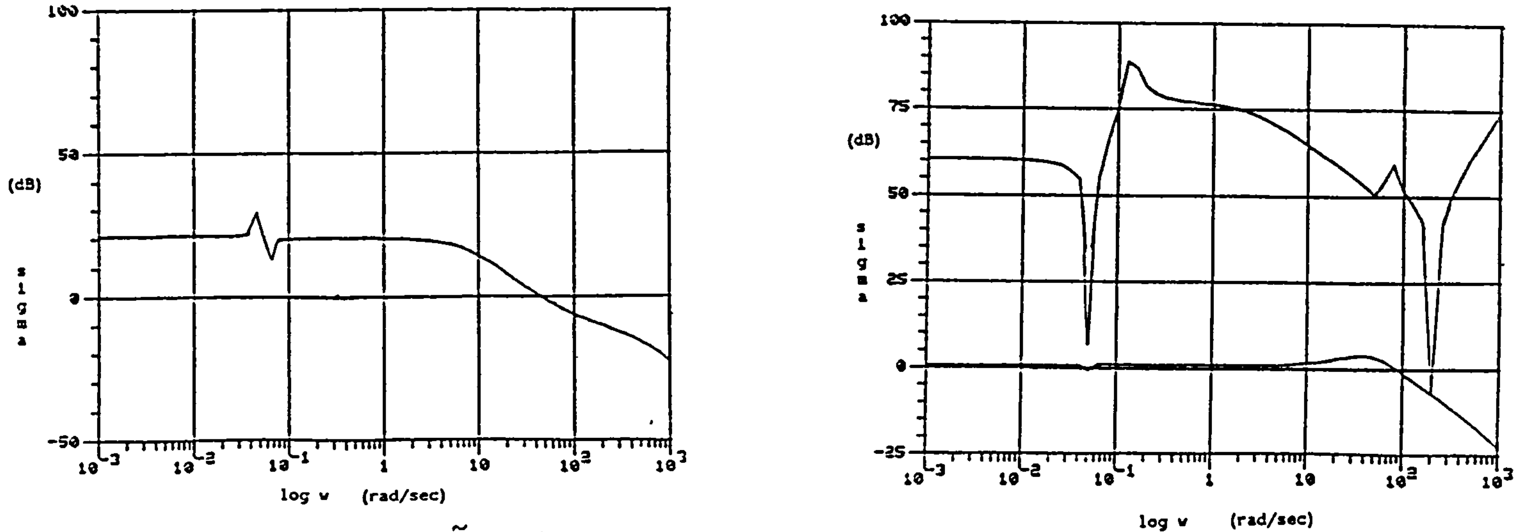

c. Open Loop TFM: $\underline{\tilde{G}}(s)\underline{K}(s)$

d. Robustness Test

Figure 4.2 Design A

the gain is 20 db at w = 1 rad/sec. The upward gain margin is 2.5 and the downward gain margin is 0.1. The phase margin is 30°.

It is also important to compare the closed loop transfer matrix with the model error to check for robustness. Figure 4.2d is a plot of the Bode gain of $(\underline{I} + [\underline{G}(s)\underline{K}(s)]^{-1})^{-1}$ and $\underline{E}_{out}(s)^{-1}$. Since the magnitude of the inverse error is greater than that of the closed loop transfer function matrix, the design is guaranteed stable in the face of this model error.

Table 4.2 lists the closed loop poles. They are all stable, as expected. The torsion mode is slightly more damped than it was in the open loop system

TABLE 4.2

DESIGN A CLOSED LOOP POLES

$-1.08 \times 10^{-4} \pm j\ 0.0515$	$-9.98 \pm j\ 59.24$	$-32.38 \pm j\ 28.57$
$-1.14 \times 10^{-4} \pm j\ 0.0513$	$-10.54 \pm j\ 59.21$	$-119.7 \quad -1527$
$-0.132 \pm j\ 212.6$		

Figure 4.3 shows the Bode gains of a) the loop sensitivity, $(\underline{I} + \underline{G}(s)\underline{K}(s))^{-1}$, b) the transfer matrix from reference input ($\underline{r}$) to actuator deflections ($\underline{u}$), $\underline{K}(s)(I + \underline{G}(s)\underline{K}(s))^{-1}$ and c) the closed loop transfer function.

The loop sensitivity gain below frequencies of 1 rad/sec is nearly -20 db. Thus the system should show 10% error in command following. We would also expect to attenuate disturbances with this frequency content by a factor of 10.

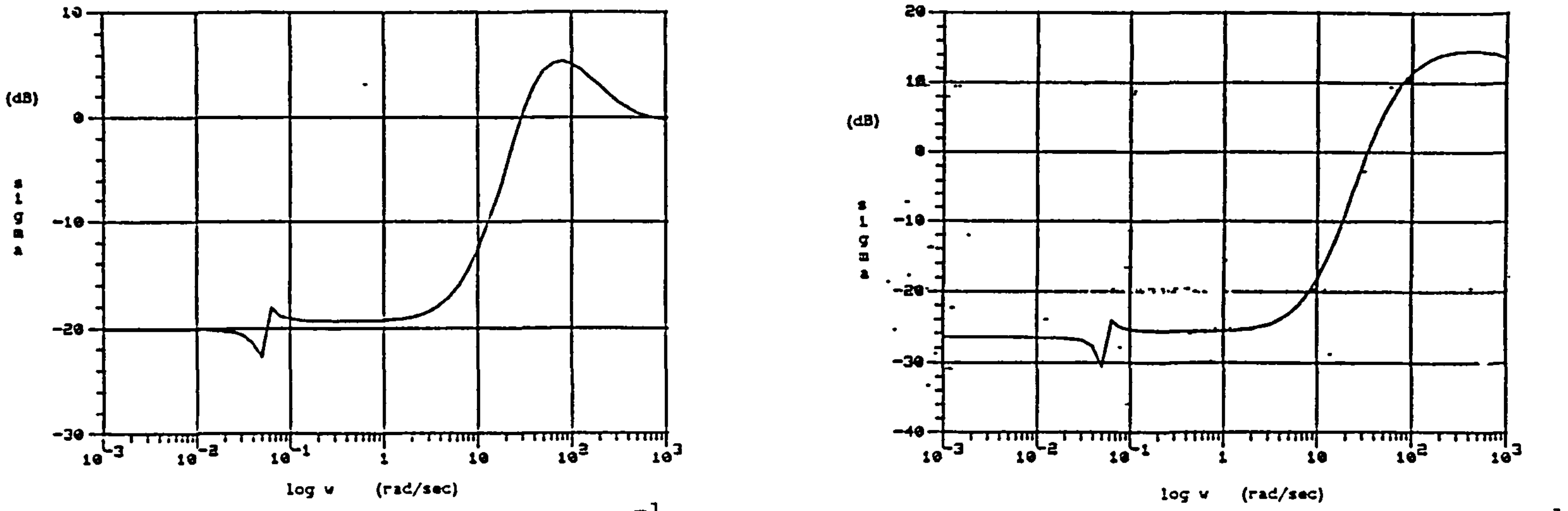

a. Loop Sensitivity: $(\underline{I}+\underline{\tilde{G}}(s)\underline{K}(s))^{-1}$

b. Loop from $\underline{r}$ to $\underline{u}$: $\underline{K}(s)(\underline{I}+\underline{\tilde{G}}(s)\underline{K}(s))^{-1}$

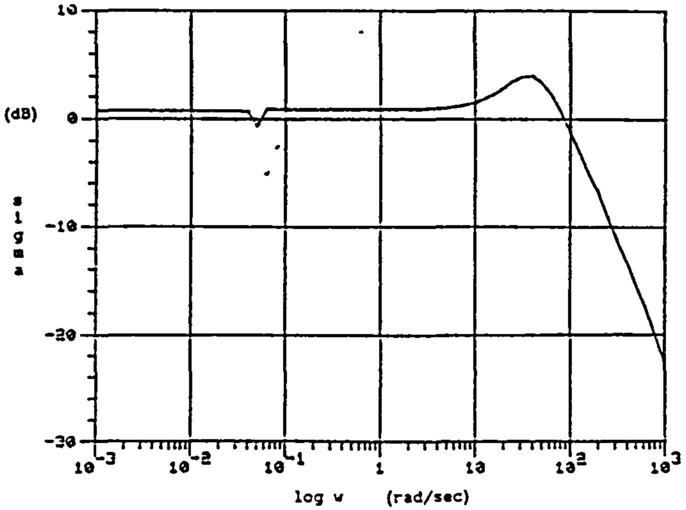

c. Closed Loop TFM

Figure 4.3 Design 1: System Summary

4.3.2 Design B: Pitch Attitude Output

The same four step procedure was followed for the system with pitch attitude output and canard input. As with Design A, the truth model includes the wing torsion mode, while the design model does not. The design model is scaled, as described in Chapter 2. Table 4.3 lists the open loop poles and zeroes of the design model.

TABLE 4.3

DESIGN MODEL B OPEN LOOP POLES & ZEROES

Open Loop Poles			
$-4.16 \times 10^{-5} \pm j\,0.0492$	$-9.873 \pm j\,59.12$	-11.9	7.31
Open Loop Zeroes			
4.08×10^{-4}	$-10.05 \pm j\,59.04$	-2.83	

Following the four step procedure outlined in Section 4.2:

1) Select $\underline{L} = \underline{B}$ and $\mu = 0.01$

2) Solve for $\underline{H}$. Figure 4.4a is a plot of the Bode magnitude of $\underline{C}(s\underline{I}-\underline{A})^{-1}\underline{H}$. The crossover frequency is 60 rad/sec and the gain is 36 db at w = 1 rad/sec, thus the loop meets the design specifications.

3) Solve for $\underline{G}$ with $q = 10^4$. The $\underline{H}$ and $\underline{G}$ matrices are listed in Appendix 2.2. Figure 4.4b is a plot of the Bode magnitude of the compensator, $\underline{K}(s)$.

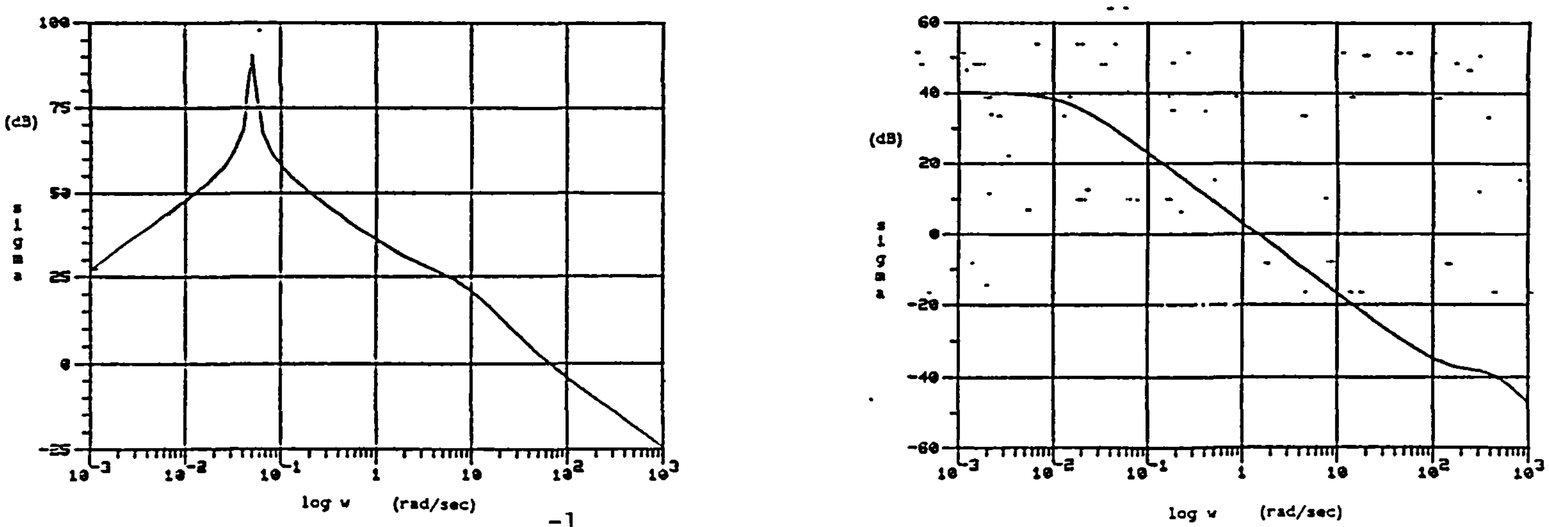

a. Target Loop : $\underline{C}(s\underline{I}-\underline{A})^{-1}\underline{H}$

b. Compensator Loop: $\underline{K}(s)$

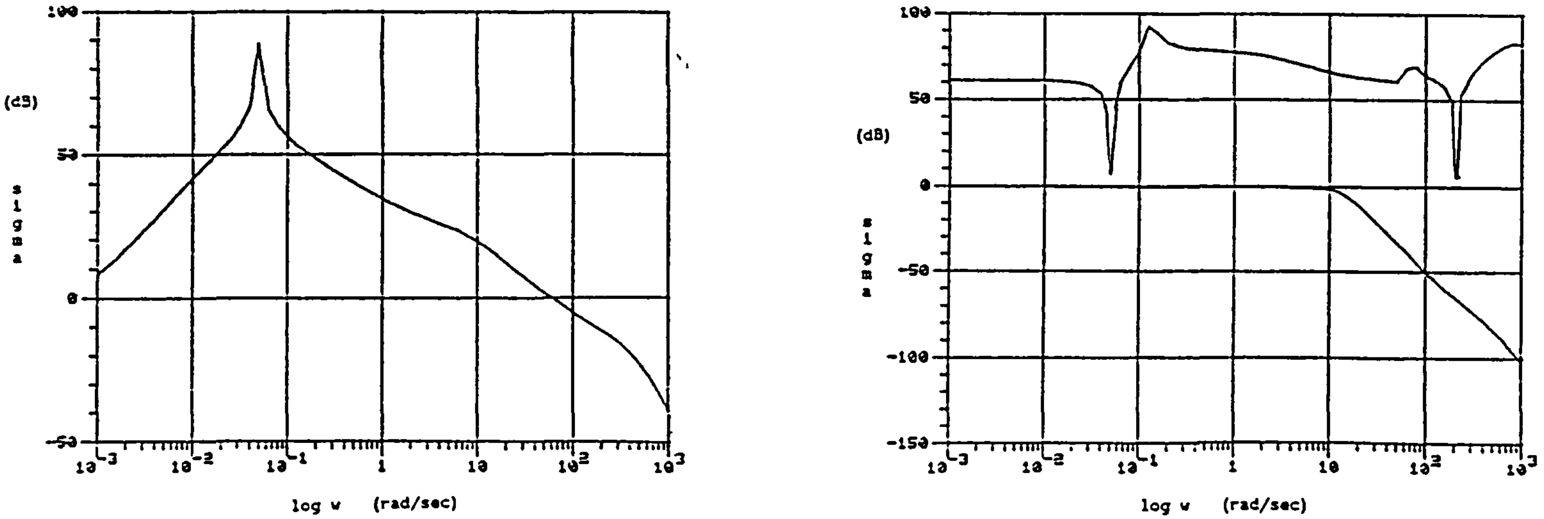

c. Open Loop TFM: $\tilde{\underline{G}}(s)\underline{K}(s)$

d. Robustness Test

Figure 4.4 Design B

4) Figure 4.4c is a plot of the gain of $\underline{G}(s)\underline{K}(s)$. The loop is very nearly recovered; the crossover frequency is 60 rad/sec and the gain is 34 db at 1 rad/sec. The upward gain margin is 10 and the downward gain margin is 0.06. The phase margin is 60°.

Figure 4.4d is a plot of the Bode magnitude of the closed loop transfer function matrix and the model error inverse. Since the gain of $\underline{E}_{out}(s)^{-1}$ is always greater than $(\underline{I} + [\underline{G}(s)\underline{K}(s)]^{-1})^{-1}$. The design is guaranteed robust with this model error.

The closed loop poles of the compensator with the true plant are listed in Table 4.4. The poles are all in the left half plane; the system is stable. The wing torsion mode is actually more lightly damped than it was in the open loop plant.

TABLE 4.4
DESIGN B CLOSED LOOP POLES

$-4.09 \times 10^{-4} \pm j\, 2.52 \times 10^{-5}$	$-9.91 \pm j\, 59.13$	$-2.83 \pm j\, 0.0121$
$-3.97 \times 10^{-4} \pm j\, 212.7$	$-10.04 \pm j\, 59.03$	$-31.14 \pm j\, 29.53$
		$-303 \pm j\, 303$

Figure 4.5 gives an overview of the design characteristics: Figure 4.5a is a plot of the gain of the loop sensitivity, $(\underline{I}+\underline{G}(s)\underline{K}(s))^{-1}$, Figure 4.5b is a plot of the gain from reference input to actuator deflection, $\underline{K}(s)(\underline{I}+\underline{G}(s)\underline{K}(s))^{-1}$, and Figure 4.5c is a plot of the closed loop frequency response.

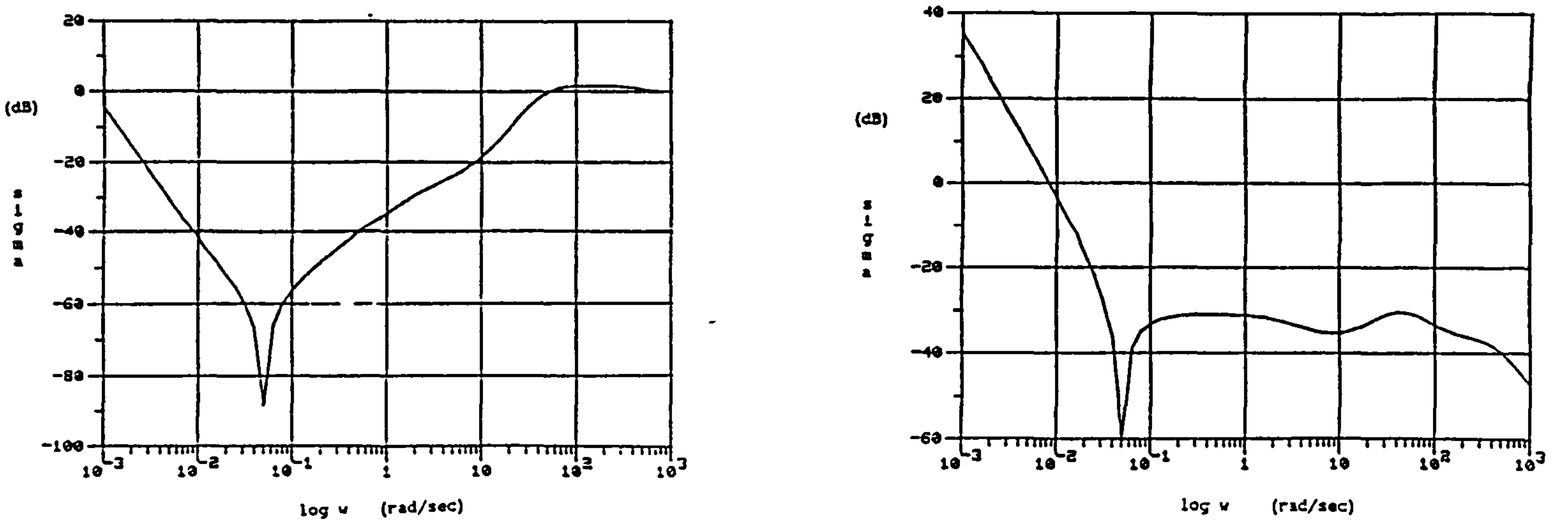

a. Loop Sensitivity: $(\underline{I}+\tilde{\underline{G}}(s)\underline{K}(s))^{-1}$

b. Loop from $\underline{r}$ to $\underline{u}$: $\underline{K}(s)(\underline{I}+\tilde{\underline{G}}(s)\underline{K}(s))^{-1}$

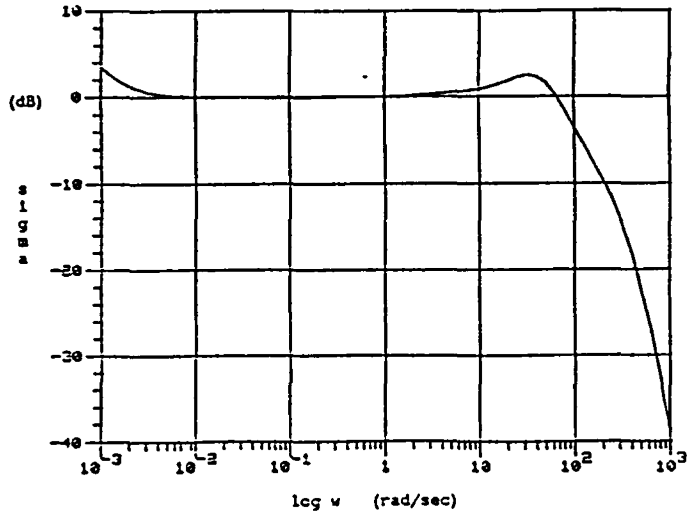

c. Closed Loop TFM

Figure 4.5 Design B: Design Summary

The sensitivity loop has a gain of less than -30 db in the frequency range between 0.01 and 1 rad/sec. The command following error for reference inputs in that frequency range will be less than 5% and may be as small as 0.01%. The sensitivity matrix of frequencies below 0.001 rad/sec is greater than zero; at DC it is approximately 10 db. This design has not met the low frequency disturbance rejection requirements. However, since the performance and robustness characteristics are very good, the design will be useful to give insight into the impact of flaperon control.

4.4 Design C: Two-Input-Two-Output

The same four step procedure followed in the SISO design will be followed here. As with the SISO designs, the scaled model without the wing torsion mode is the design model. The controls are flaperon and canard; the outputs are angle of attack and pitch attitude. Table 4.5 lists the open loop poles and zeroes of the design model.

TABLE 4.5
DESIGN MODEL C OPEN LOOP POLES & ZEROES

Open Loop Poles:

$-4.16 \times 10^{-5} \pm j\,0.0492 \qquad -9.873 \pm j\,59.12 \qquad -11.9 \qquad 7.31$

Open Loop Zeroes

$-1.49 \times 10^{-4} \qquad - 7.076 \pm j\,65.03$

This system is minimum phase, but as with Design B, there is a low frequency zero.

Following the four steps outlined in Section 4.2:

1) Select $\underline{L}$. In this case it was necessary to bring the singular values closer together near the crossover frequency in order to make the bandwidth less than 60 rad/sec. Since the expected crossover frequency was near 10 rad/sec, we tried to match the maximum and minimum singular values at that frequency. The idea is to make

$$\underline{C}(jw\underline{I}-\underline{A})^{-1}\underline{L} = \underline{I} \tag{4.10}$$

at w = 10 rad/sec. Allowing $\underline{L} = \underline{Bm}$ where $\underline{m}$ is the so called matching matrix give

$$\underline{m} = [\underline{C}(j10\underline{I}-\underline{A})^{-1}\underline{B}]^{-1}, \tag{4.11}$$

which exists, but is complex. In order to find a matrix we could use, we took the "best real inverse":

$$\underline{m} = \text{Re}\ [\underline{C}(j10\underline{I}-\underline{A})^{-1}\underline{B}]^{-1} \tag{4.12}$$

and let $\underline{L} = \underline{Bm}$. The matching matrix, $\underline{m}$, is listed in Appendix 2.3. We used $\mu = 0.01$.

2) Solve for $\underline{H}$. Figure 4.6a is a plot of the singular values of $\underline{C}(s\underline{I}-\underline{A})^{-1}\underline{H}$. The minimum singular value is 18 db at w = 1 rad/sec and its crossover frequency is 16 rad/sec. The maximum singular value has a crossover frequency at 60 rad/sec and a gain of 33 db at w = 1 rad/sec. The specifications are not quite met as the gain is 2 db too low at w = 1 rad/sec, however it is quite close.

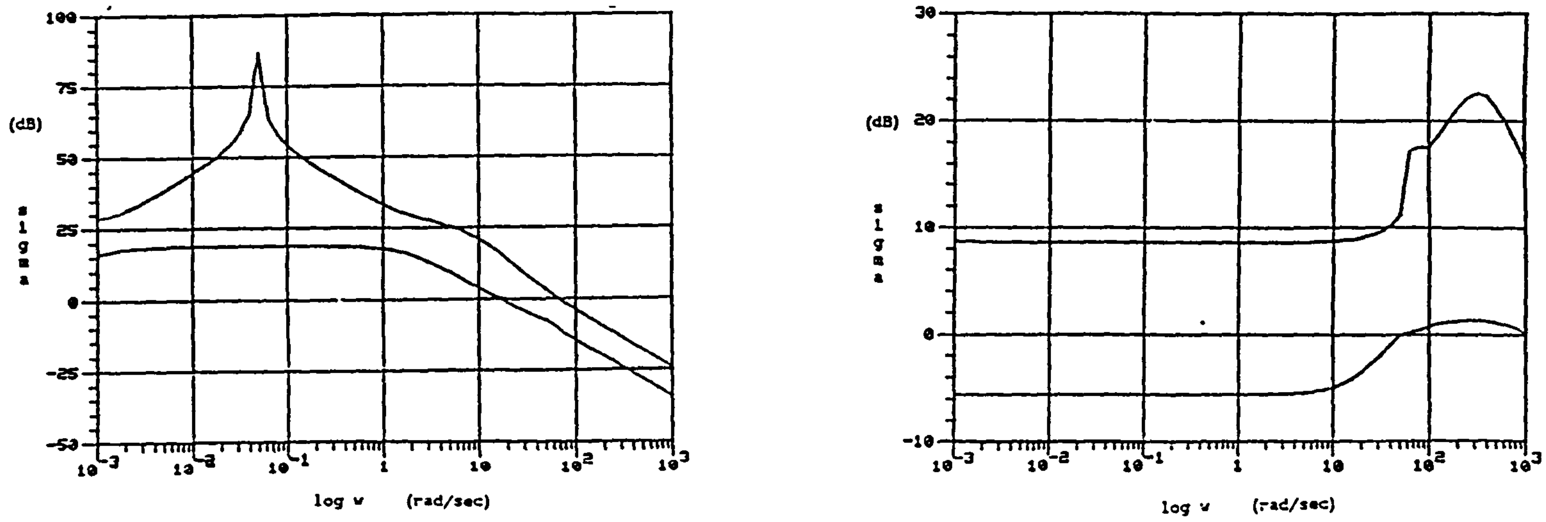

a. Target Loop: $\underline{C}(s\underline{I}-\underline{A})^{-1}\underline{H}$

b. Compensator Loop: $\underline{K}(s)$

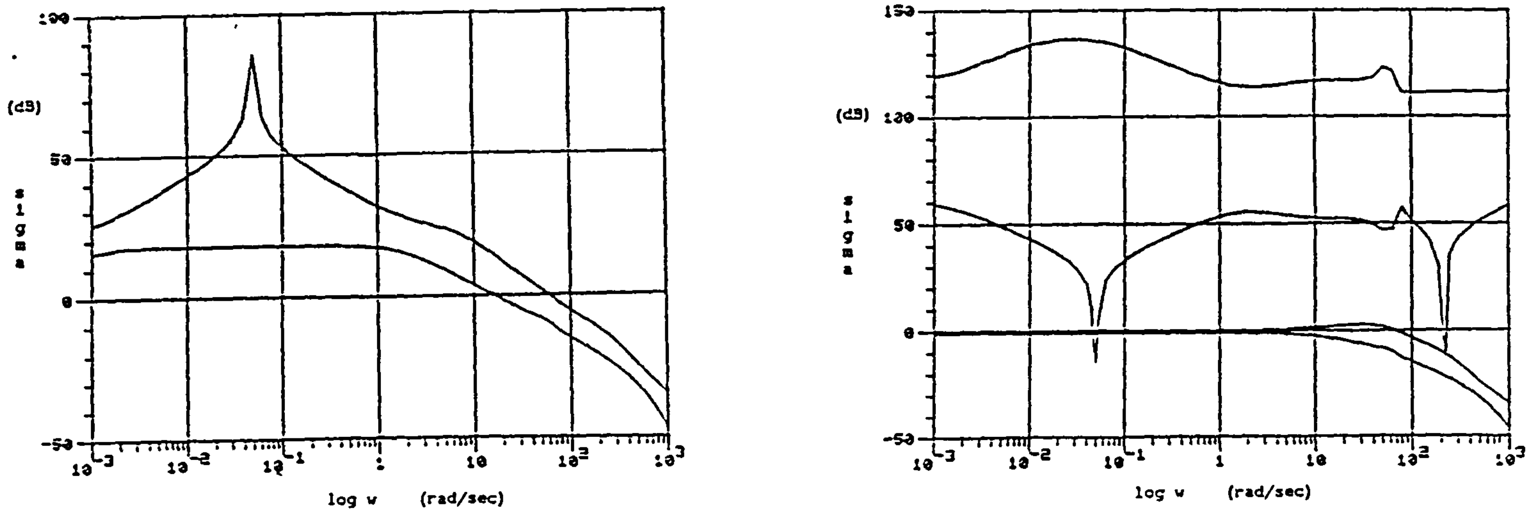

c. Open Loop TFM: $\underline{\tilde{G}}(s)\underline{K}(s)$

d. Robustness Test

Figure 4.6 Design C

3) Solve for $\underline{G}$ with $q = 10^4$. The $\underline{H}$ and $\underline{G}$ matrixes are listed in Appendix 2.3. Figure 4.6b is a plot of the compensator singular values.

4) Figure 4.6c is a plot of $\underline{G}(s)\underline{K}(s)$ singular values. The $\underline{C}(s\underline{I}-\underline{A})^{-1}\underline{H}$ loop is almost perfectly recovered. The minimum singular value at w = 1 rad/sec dropped slightly to 17 db.

Figure 4.6d is a plot of the robustness test, $\underline{E}_{out}(s)^{-1}$ and $(\underline{I} + [\underline{G}(s)\underline{K}(s)]^{-1})^{-1}$. The robustness test is not passed due to the notch at the phugoid frequency, 0.05 rad/sec. However, for this study the emphasis is on the high frequency dynamics. In order to get rid of the notch, the low frequency phugoid mode must be modelled more accurately. The mode is very lightly damped. A slight error in the model frequency shows up as a very large error in the model. In this case, by dropping the wing torsion mode the phugoid frequency was changed slightly, from 0.04923 rad/sec to 0.04921 rad/sec. This is really a problem with the computation of the eigenvalues of the $\underline{A}$ matrix of the truth model and the design model.

The closed loop poles are listed in Table 4.6. The poles are all stable. The wing torsion mode damping happens to have improved slightly.

TABLE 4.6

DESIGN C CLOSED LOOP POLES

-1.49×10^{-4}	$-7.16 \pm j\,33.7$	-17.6	$-33.7 \pm j\,25.8$
-1.90×10^{-4}	$-9.46 \pm j\,60.0$	-1623	$-221 \pm j\,191$
$-0.0314 \pm j\,212.7$			

The design is summarized in Figure 4.7: 4.7a is a plot of the singular values of the loop sensitivity, 4.7b shows the singular values of the transfer matrix from the reference input, $\underline{r}$, to the actuator deflections, $\underline{u}$, and 4.7c is a plot of the singular values of the closed loop transfer function matrix.

The loop sensitivity function shows the maximum singular value is -18 db in the frequency range $0.005 < w < 1$ rad/sec. The command following error will be less than 10% for inputs in that frequency range, depending on the direction of the reference input. Since the minimum singular value is less then -80 db, the error may be as small as 0.01%. At very low frequencies the loop sensitivity is at -5 db. This indicates that disturbances in that frequency range will be attenuated by a factor of 1.7.

4.5 Discussion

The maximum and minimum singular values of a transfer matrix need not be aligned with either angle of attack or pitch attitude. It appears, however, that the maximum

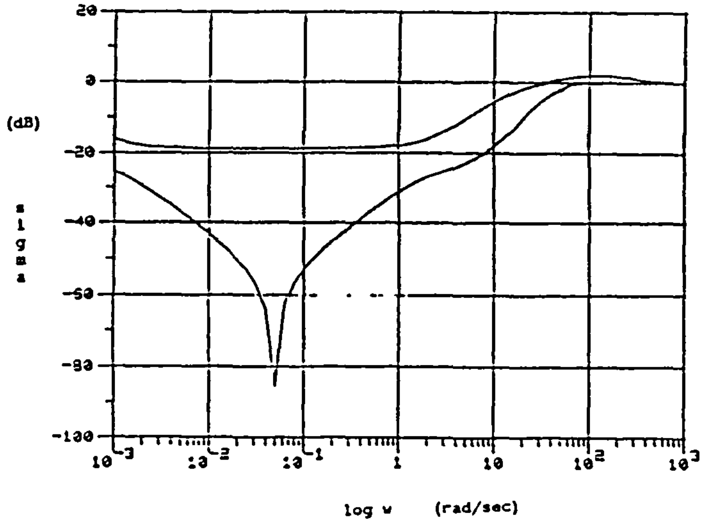

a. Loop Sensitivity: $(\underline{I}+\underline{\hat{G}}(s)\underline{K}(s))^{-1}$

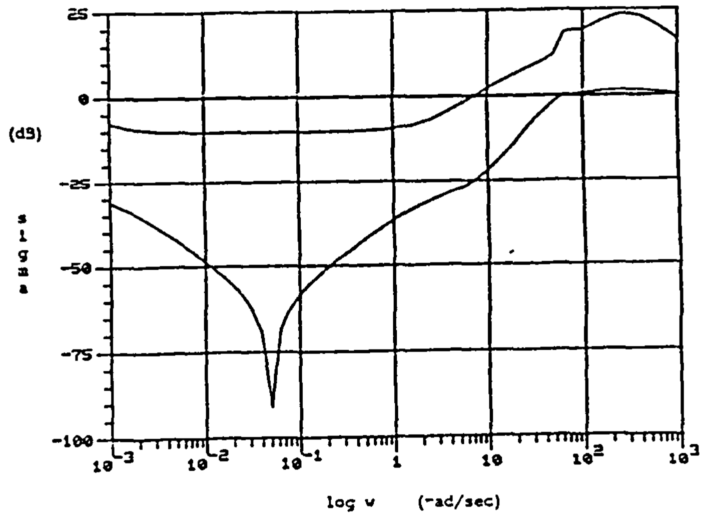

b. Loop from $\underline{r}$ to $\underline{u}$: $\underline{K}(s)(\underline{I}+\underline{\check{G}}(s)\underline{K}(s))^{-1}$

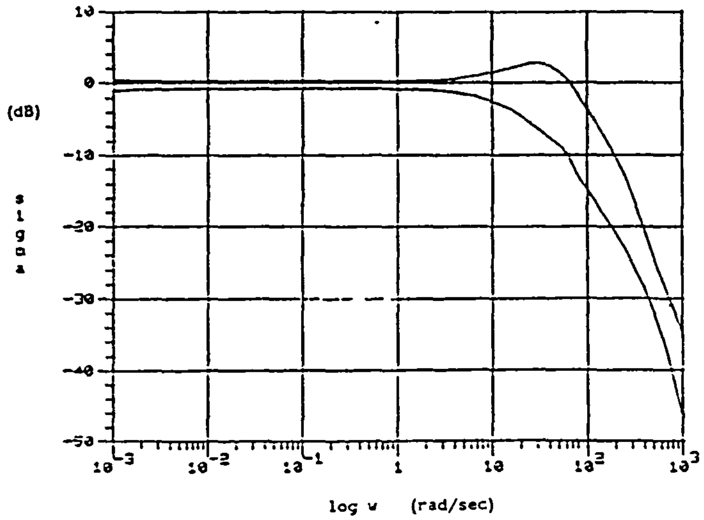

c. Closed Loop TFM

Figure 4.7 Design C: System Summary

singular value of the loop sensitivity is in the angle of attack direction and the minimum singular value in the pitch attitude direction. We plan to illustrate this at a particular frequency with a time simulation in which the reference input is a sinusoid.

Figure 4.8 is a comparison of the three designs. Figure 4.8a shows the singular values of $\underline{G}(s)\underline{K}(s)$ for all three designs, 4.8b shows the loop sensitivity and 4.8c is a plot of the closed loop frequency responses.

There are several things to note from this comparison. Both the minimum singular value and Design B (SISO θ) have a large notch at the phugoid frequency, (0.05 rad/sec) in the loop sensitivity. The gains of both for frequencies greater than 0.01 rad/sec are very similar. On the other hand, the minimum singular value and Design A have very similar loop sensitivity functions. The maximum singular value of the loop sensitivity appears to be in the angle of attack direction while the minimum singular value is in the pitch attitude direction, for frequencies above 0.01 rad/sec.

In order to illustrate this, sinusoidal reference inputs for angle of attack and pitch attitude were used in a time simulation of Design C. The commands are 1° peak at 0.3 rad/sec. The angle of attack and pitch attitude are 90° out of phase. In other words, the inputs trace out a unit circle in the command input (α_c, θ_c) plane. The minimum singular value of the loop sensitivity at 0.3 rad/sec is -40 db. The minimum error should be 1%,

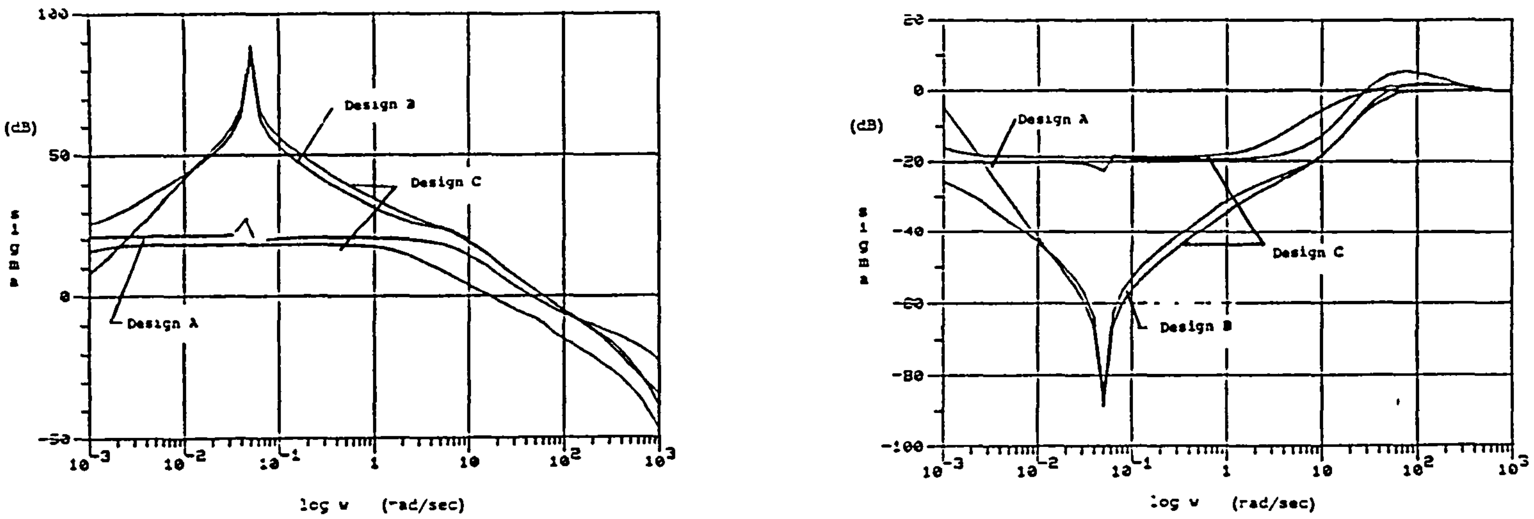

a. Open Loop TFM: $\underline{\tilde{G}}(s)\underline{K}(s)$

b. Loop Sensitivity: $(\underline{I}+\underline{\tilde{G}}(s)\underline{K}(s))^{-1}$

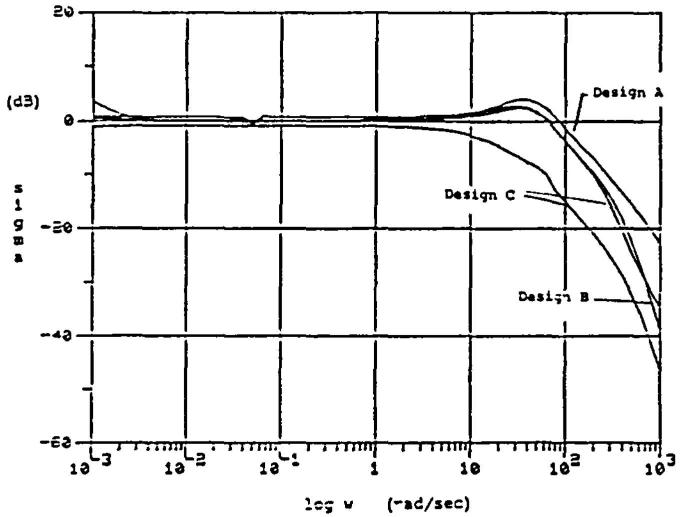

c. Closed Loop TFM

Figure 4.8 Design Comparison

and we expect it to occur when the reference input is in the θ direction i.e. $\theta_c = 1^\circ$, $\alpha_c = 0^\circ$. The maximum singular value of the loop sensitivity at 0.3 rad/sec is -18 db. The maximum error should be 12%; it should occur when the reference input is in the angle of attack direction, i.e. $\theta_c = 0^\circ$, $\alpha_c = 1^\circ$.

In terms of the time simulation, the reference inputs are in the θ direction at $t = 0$ and $t = \pi/w = 10.5$ sec. The error should be a minimum at those times. The maximum error should occur when the reference inputs are in the angle of attack direction at $t = 5.25$ sec. Figure 4.9 shows the results of the time simulation. The command inputs are shown in 4.9a, 4.9b shows the angle of attack ard 4.9c shows the pitch attitude. The plot in 4.9d shows the square error; this is the sum of the deviation in angle of attack squared and the deviation in pitch attitude squared.

Figure 4.9d shows the peak error occurs $t = 5.1$ sec, slightly before the prediction of $t = 5.25$ sec. The error is 0.13° or -18 db which is the maximum singular value of the loop sensitivity. The minimum error occurs at $t = 10.3$ sec, again slightly before the predicted time of $t = 10.5$ sec. The error is $8 \text{ X } 10^{-3^\circ}$ which is -42 db, slightly less than the minimum singular value of 0.3 rad/sec. Figure 4.10 is a plot of the accuracy ellipse in the α, θ output space based on the time simulation. The length of the vectors in each direction corresponds to the reciprocal

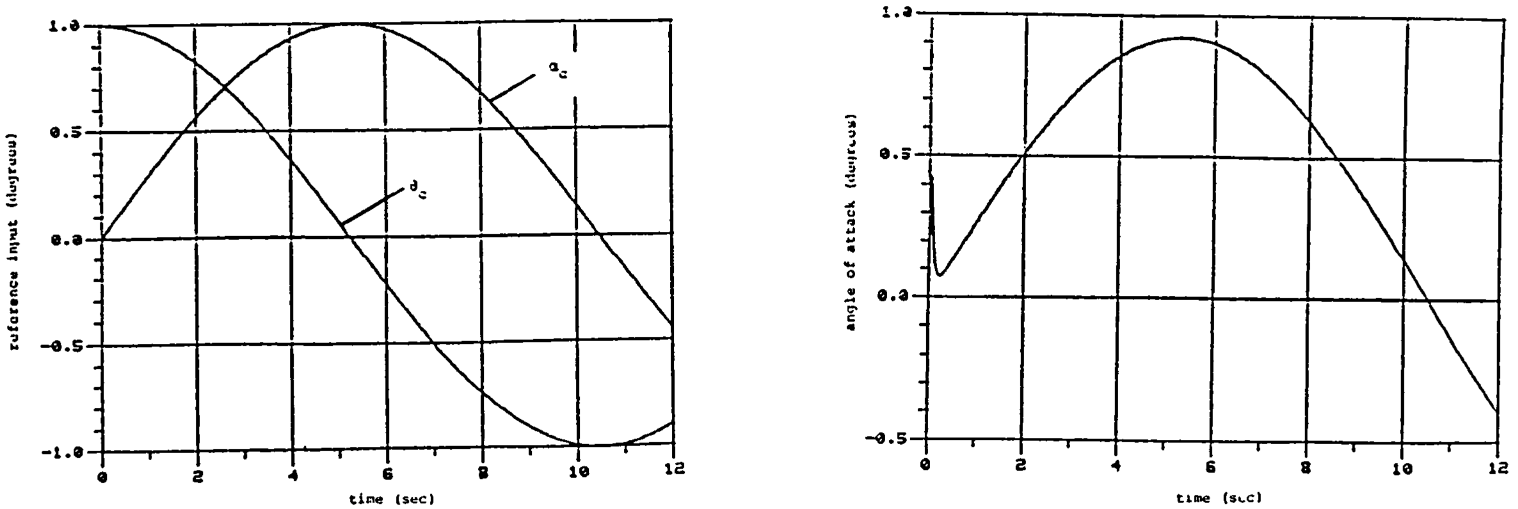

a. Reference Input Commands

b. Angle of Attack

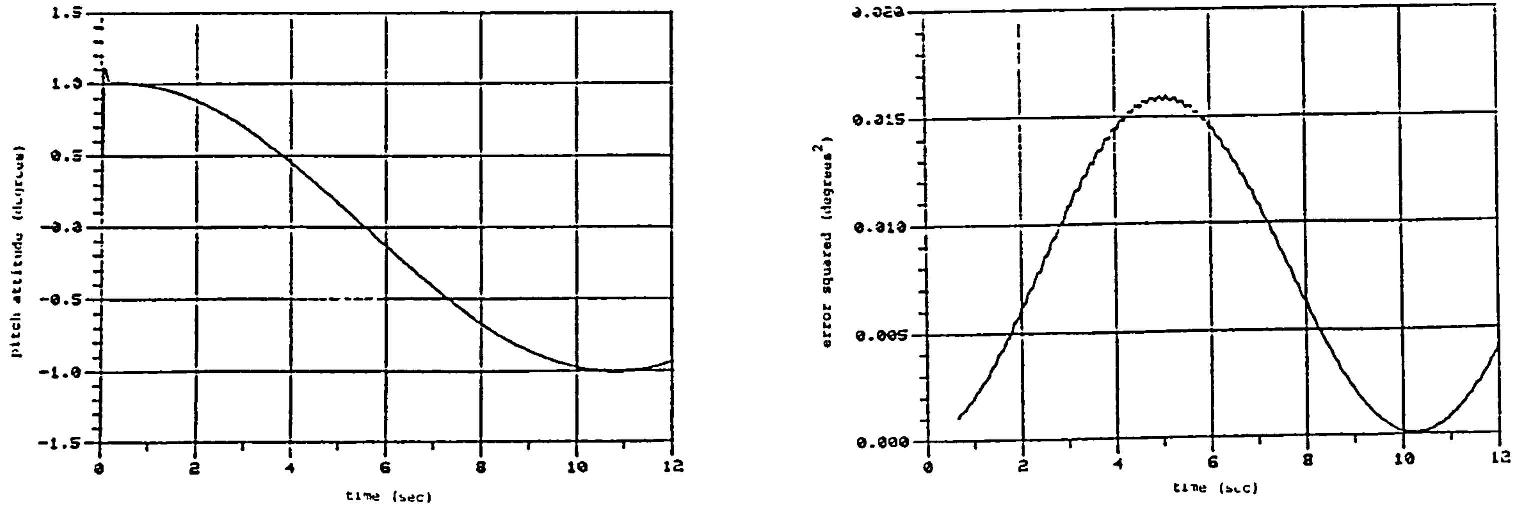

c. Pitch Attitude

d. Error Squared: $(\theta-\theta_c)^2+(\alpha-\alpha_c)^2$

Figure 4.9 Design C: Response to Sinusoidal Commands

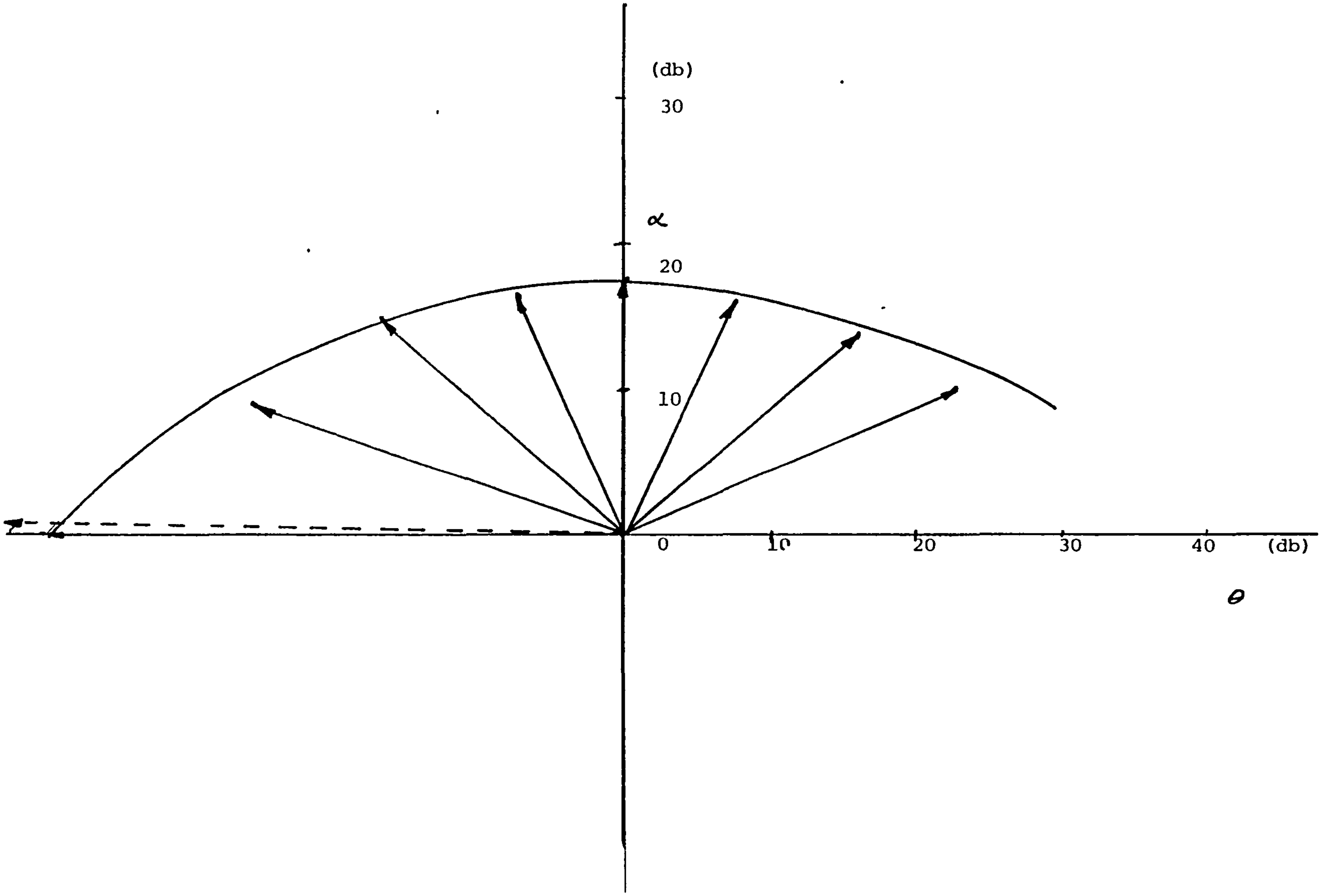

Figure 4.10 Accuracy Ellipse in the angle of attack and pitch attitude plane based on the simulation results.

of the error in db. We see that the most accurate direction is primarily in the pitch attitude direction. The major axis is 3° above the pitch attitude axis. The minor axis is primarily in the angle of attack direction, 2° off the angle of attack axis.

For purposes of comparison, the SISO designs were also simulated with a sinusoidal reference input. Figure 4.11 shows the results for Design A: 4.11a is the reference input, 4.11b is the angle of attack output, 4.11c is the pitch attitude output and 4.11d is the deviation of the angle of attack output from the reference input. Two things to note are the peak error is approximately 0.11° or 11% as predicted and the pitch attitude has a peak of 20°.

Design B was also simulated with a sinusoidal reference input. The results are shown in Figure 4.12: 4.12a shows the reference input, 4.12b shows the pitch attitude, 4.12c shows the angle of attack and 4.12d is a plot of the difference between the command input and the pitch attitude output. The maximum error in this case is 0.006° which is much smaller than the error in Design A.

The response of the aircraft to angle of attack commands with only canard control, illustrated by Design A, is much worse than its response to pitch attitude commands as shown with Design B. First, the command following error is much larger in angle of attack for Design A than the pitch attitude error of Design B. In addition, the

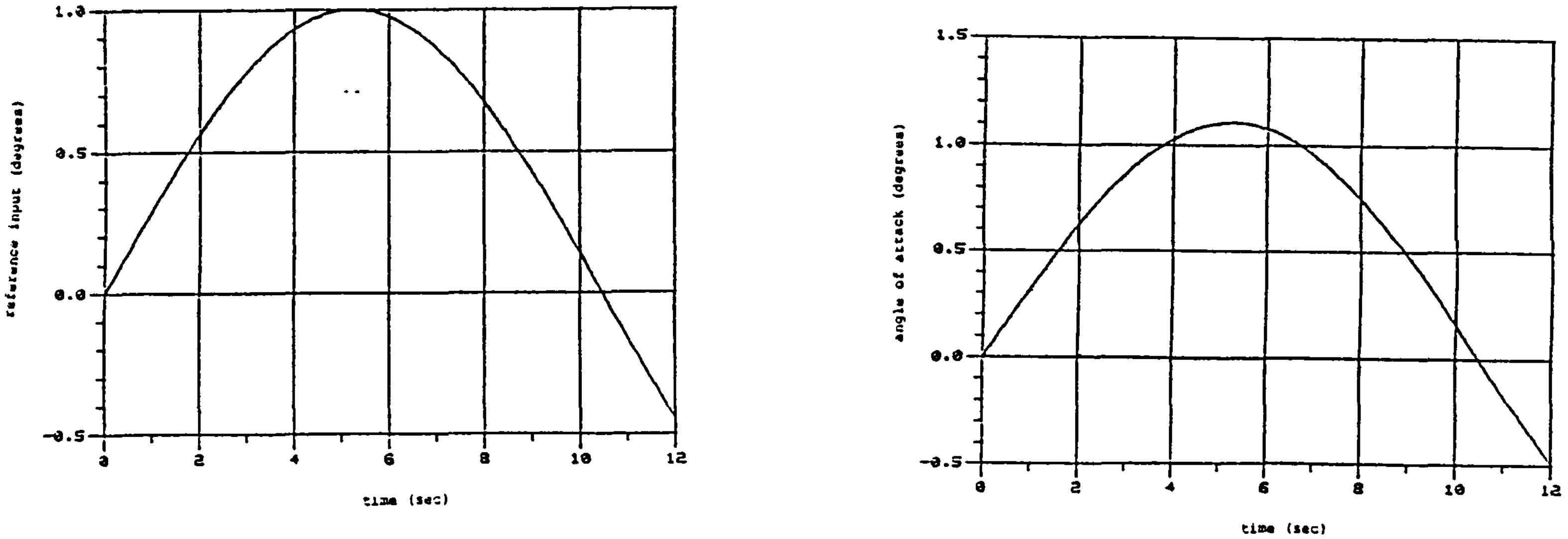

a. Reference Input Command: α_c

b. Angle of Attack

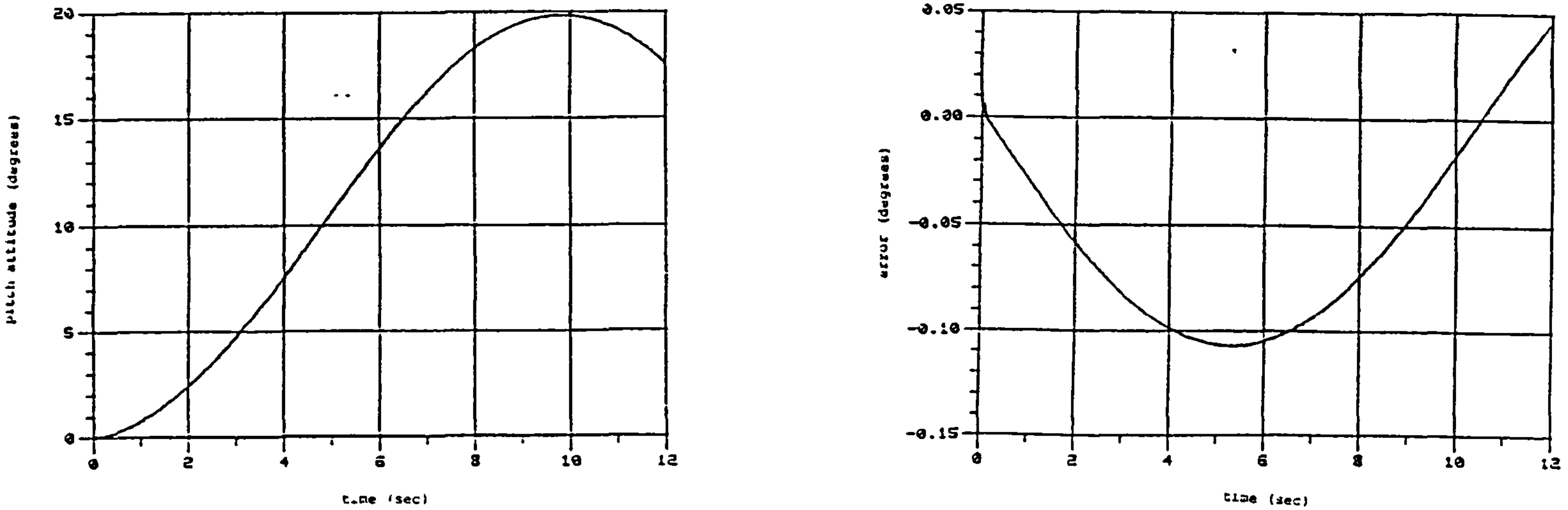

c. Pitch Attitude

d. Command Following Error: $\alpha_c - \alpha$

Figure 4.11 Design A: Response to Sinusoidal Command

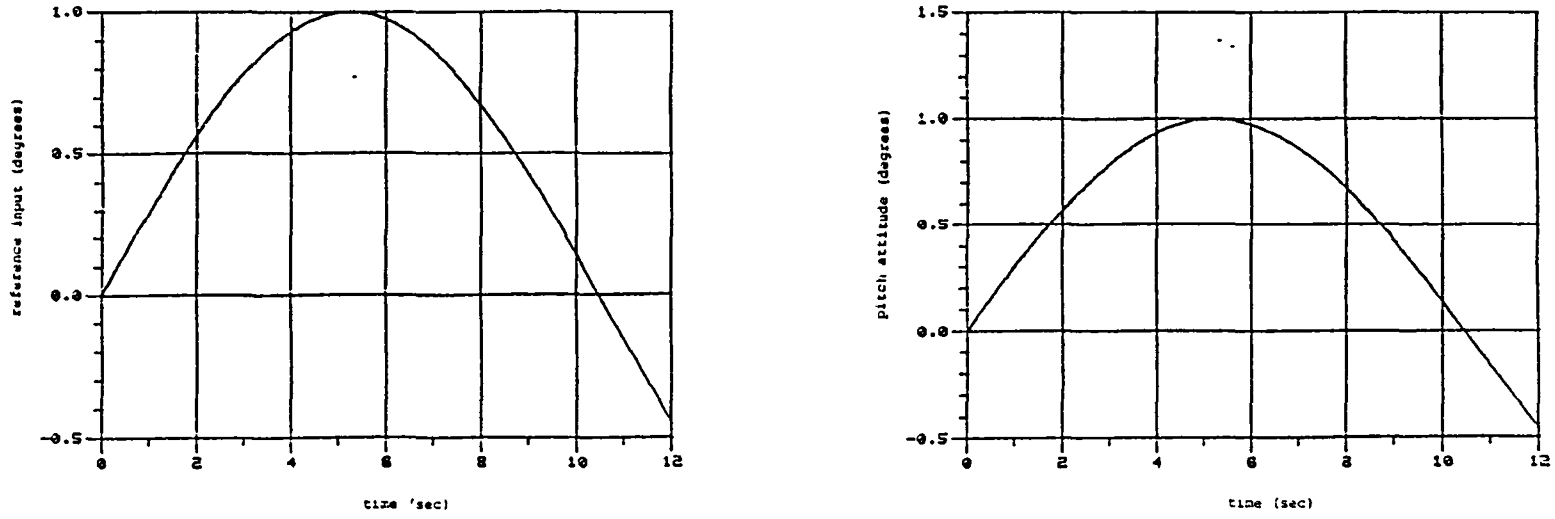

a. Reference Input Command: θ_c

b. Pitch Attitude

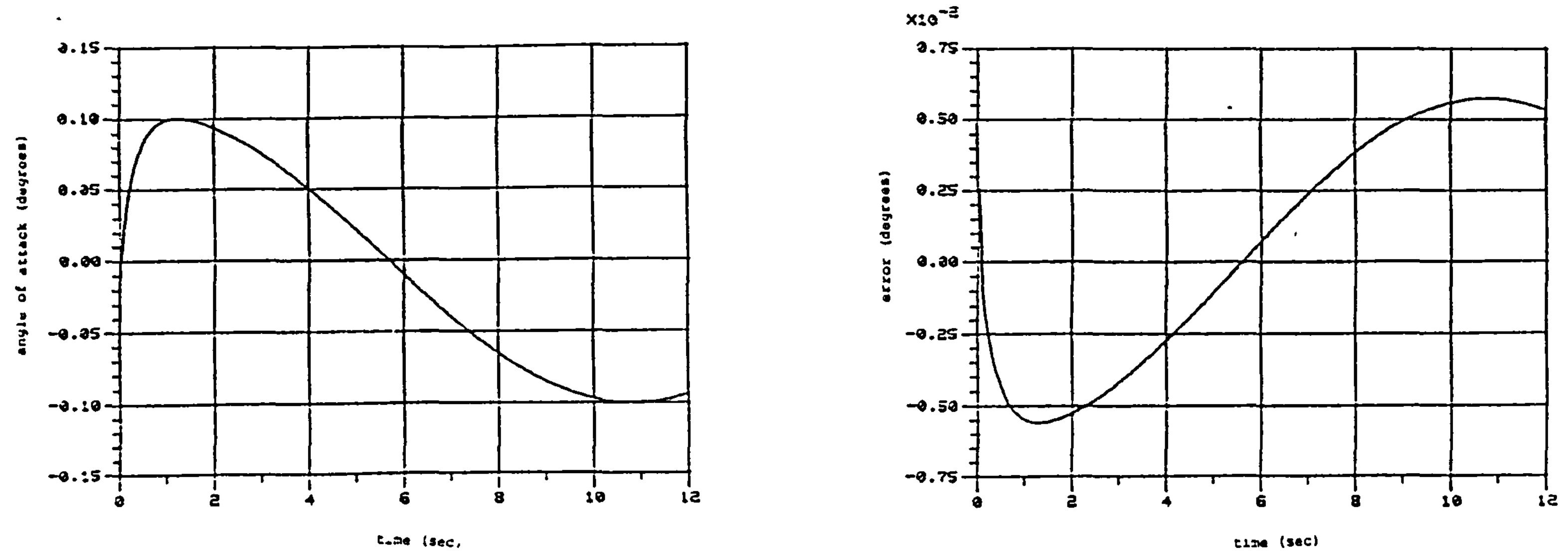

c. Angle of Attack

d. Command Following Error: $\theta_c - \theta$

Figure 4.12 Design B: Response to Sinusoidal Command controlled output, in pitch attitude for Design A and angle of attack for Design B, exhibits much larger excursions for Design A than Design B. Comparing the SISO designs to the TITO designs, we see that here too, the command following in angle of attack is much worse than the command following performance of the pitch attitude.

4.6 Summary

In this chapter, three compensators were designed using the LQG/LTR method:

Design A: SISO canard control, angle of attack output

Design B: SISO canard control, pitch attitude output

Design C: TITO canard and flaperon control, angle of attack and pitch attitude outputs.

The three compensators were designed to meet roughly the same specifications. The design process was described in Section 4.3 and 4.4.

The directionality of the transfer matrix from command inputs to controlled outputs for the TITO system was illustrated using a time simulation. The reference inputs were sinsoids at w = 0.3 rad/sec. The SISO designs were also simulated with reference inputs at w = 0.3 rad/sec.

Commands to the TITO system in the pitch attitude direction were followed very accurately, as were commands to the SISO θ system. Commands to the TITO system in the angle of attack direction and to the SISO α system were not followed nearly as accurately. This will be further illustrated in the next chapter where we simulate the vertical translation mode ($\theta_c = 0$, $\alpha_c > 0$), the direct lift mode ($\theta_c > 0$, $\alpha_c = 0$) and the pitch pointing mode ($\theta_c = \alpha_c \neq 0$, $\gamma_c = 0$).

CHAPTER 5: FLAPERON EFFECTIVENESS IN THE PRECISION CONTROL MODES

5.1 Introduction

The impact of using the flaperon in the precision control modes will be examined in this chapter. The performance of the two SISO Designs (A and B), which only have control through the canard, will be compared with the performance of the TITO system (Design C), which uses both the canard and flaperon as controls.

In the previous chapter we established that the TITO system exhibits more accurate command following when the sinusoidal commands are in the pitch attitude direction. Alternately, the command following performance was not very good when the sinusoidal reference inputs are in the angle of attack direction. In this chapter, the performance of the SISO angle of attack system (Design A), will be compared to the performance of the TITO system operating in the vertical translation mode, which requires a change in angle of attack at constant pitch attitude. The performance of the SISO pitch attitude output system (Design B) will be compared to the TITO system operating in the direct lift mode, which involves a change in pitch attitude at constant angle of attack. In addition, the performance of the TITO system in the pitch pointing mode will be examined. This mode requires the same change in angle of attack as in pitch attitude, leaving the flight path angle unchanged. Finally the performance of the TITO system will be examined with the commanded input $\theta_c = -\alpha_c$, thus the flight path angle should be twice the commanded pitch angle.

5.2 Precision Control Modes

5.2.1 Vertical Translation Mode

The loop sensitivity plot (Figure 4.8a) showed the maximum singular value of the TITO system and the gain of the SISO α system (Design A) are very similar. Since the maximum singular value is in the angle of attack direction, we expect the command following performance of Design A to be comparable to the performance of the TITO system in the vertical translation mode. Both systems should exhibit command following error on the order of 10%. However, Design A has no control over the pitch attitude, which will be allowed to drift off. Figure 5.1a is a schematic of the aircraft response to the SISO command in angle of attack. Each sketch represents the aircraft coordinates at succeeding time intervals. Figure 5.1b shows the aircraft operating in the vertical translation mode. The aircraft maintains its pitch attitude as it flies downward.

The SISO system is using the canard to control the angle of attack. However, at the same time the deflected canard is causing the aircraft to pitch up. When flaperon

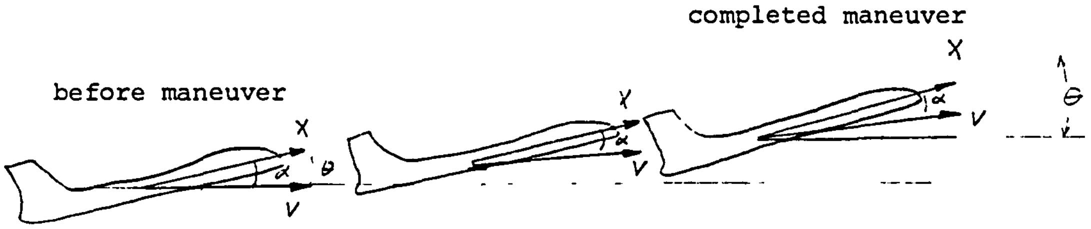

a. SISO command angle of attack only; continuously increasing pitch attitude (Design A)

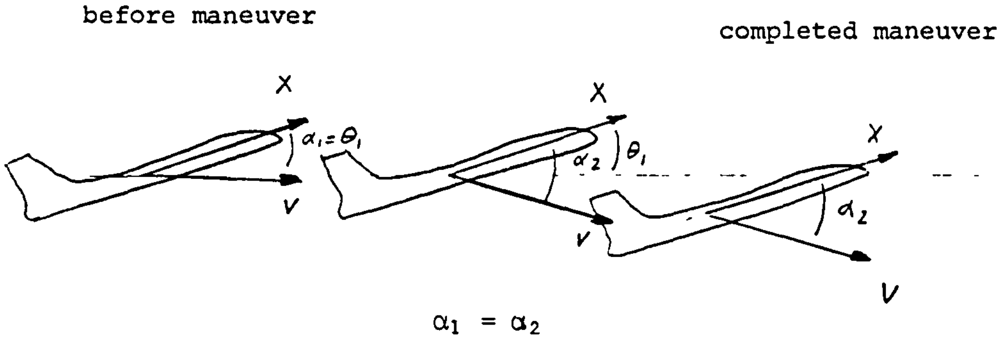

b. TITO Vertical Translation Mode (Design C)

Figure 5.1 Schematic of Aircraft Response comparing Design A and Design C control is included, the canard deflection can be balanced by the flaperon deflection and the desired pitch attitude maintained.

In order to illustrate the systems' performance, Design A was simulated with a reference input in angle of attack. The commanded angle of attack was ramped-up for 0.1 sec from 0° to 1° where it was held. Similarly, Design C was simulated with the same angle of attack command, but a zero command in pitch attitude. Figure 5.2 shows the simulation results: 5.2a is the angle of attack responses, 5.2b is the pitch attitudes, 5.2c is the canard deflections for both systems. Figure 5.2d is the TITO flaperon deflections.

As can be seen from Figure 5.2a, the angle of attack responses are somewhat different. The SISO system has quite a bit of overshoot and after 0.5 sec it is at 1.1°. The TITO response is highly damped; after 0.5 sec it is at 0.93°. The steady state error magnitudes are quite similar.

The pitch attitudes in Figure 5.2b are very different. The pitch attitudes of Design A drifts up to 2.5° after only 0.5 sec, with a pitch rate of 3 deg/sec. The TITO system, which has commanded pitch attitude of 0°, has a steady state error in pitch attitude of only 0.1° after 0.5 sec.

The canard deflections, shown in Figure 5.2c are similar in that a negative deflection is followed by a positive peak in deflection and both level out to a constant positive deflection. The transient deflections are much larger for the SISO system than the TITO system,

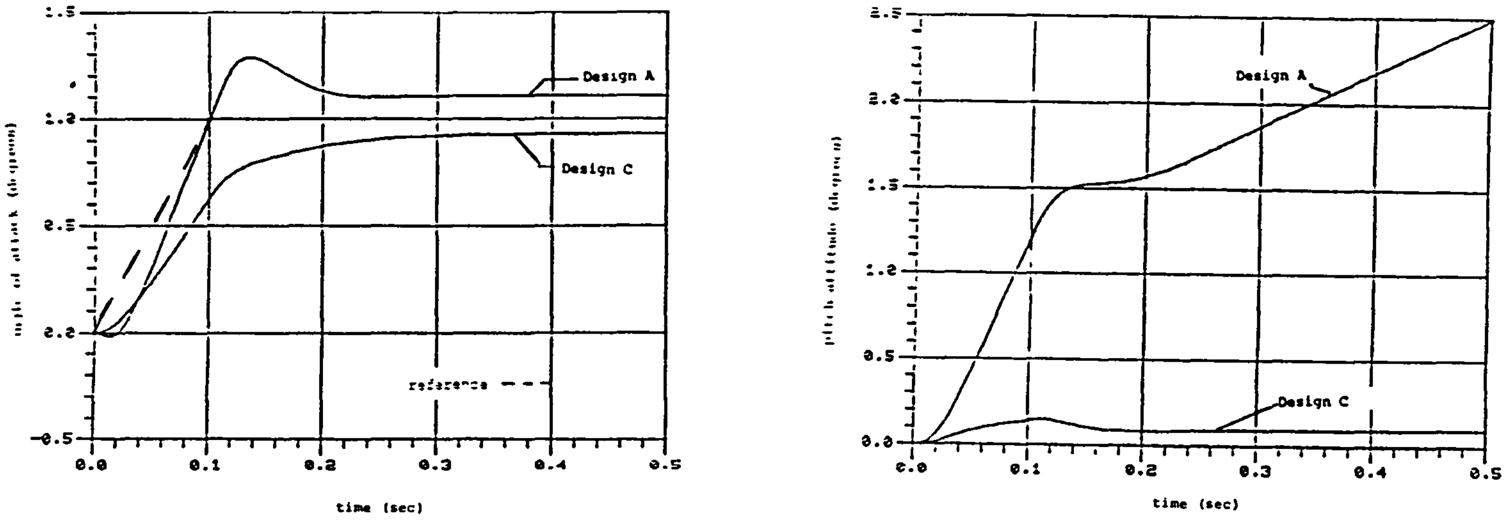

a. Angle of Attack

b. Pitch Attitude

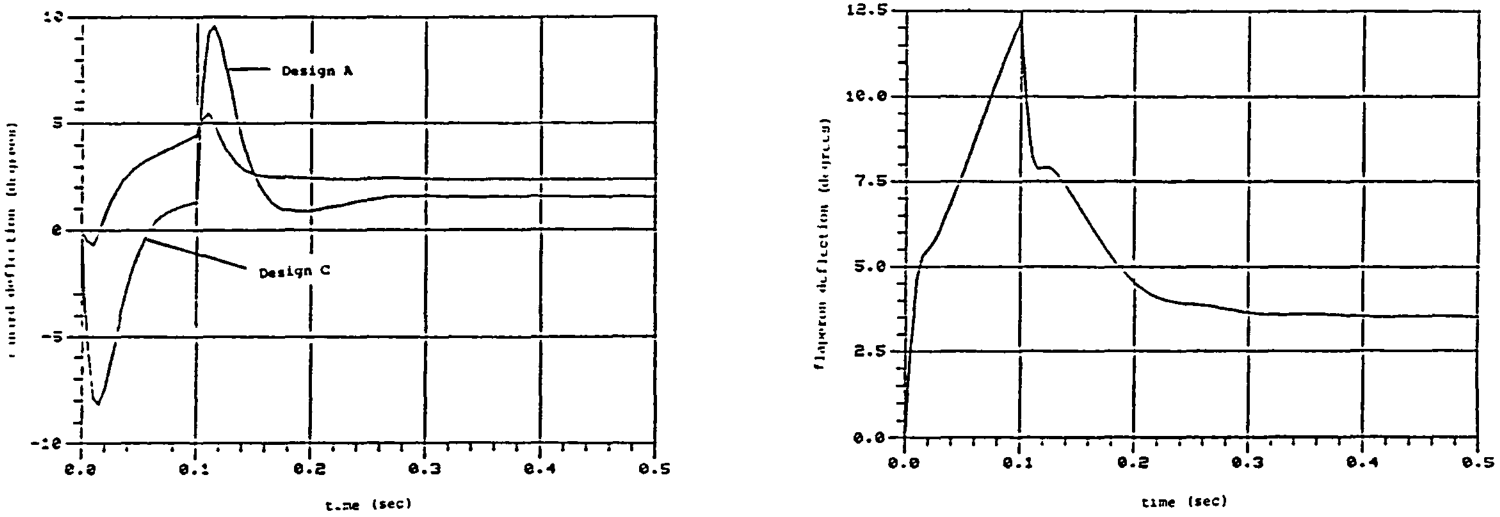

c. Canard Deflections

d. Flaperon Deflections

Figure 5.2 Vertical Translation Mode
Compare Performance of Designs A and C

however the TITO system has a larger steady state deflection.

The flaperon deflections are shown in Figure 5.2d. We can see how the canard and flaperon are working together. The positive canard deflection causes positive pitching of the aircraft. This is balanced by the positive flaperon deflection which generates a negative pitching moment.

The linear operating range of the aircraft is limited by the allowed flaperon deflections. Based on the results of the TITO simulation, reference input commands in the range of $-0.6° < \alpha_c < 1.2°$ in the vertical translation mode would not saturate the flaperon. In other words, the peak transient of flaperon change in deflection would be within the range $-6.95° < f(t) < 28.05°$ when the reference inputs are between -0.6° and 1.2°.

5.2.2 Direct Lift Mode

The minimum singular value of the TITO loop sensitivity and the gain of Design B are very similar as was indicated in Figure 4.8b. Since the minimum singular value is in the pitch attitude direction, we expect the command following performance of Design B to be similar to the performance of the TITO system in the direct lift mode. Both systems should exhibit command following errors smaller than 5% and possibly as small as 0.01%. Design B has no control over angle of attack, which will be allowed to drift off. In addition, the system has a low frequency zero which means the actuator must continuously increase its deflection in order to maintain the commanded pitch attitude.

Figure 5.3a is a schematic of the aircraft response to a pitch attitude command with only canard control. The direct lift mode is sketched in Figure 5.3b. We see from the schematic that in the direct lift mode the aircraft pitches up, increasing the flight path angle without changing the angle of attack. Without flaperon control, the aircraft pitches up, and the angle of attack continuously decreases causing the flight path angle to increase steadily.

Figure 5.4 shows the transient response of Designs A and C to a pitch attitude command. The reference input is ramped-up from 0° to 1° over 0.1 sec after which it remains constant. The angle of attack command is 0° for the TITO system. Figure 5.4a shows the pitch attitude response, 5.4b shows the angle of attack response, 5.4c shows the canard deflections and 5.4d shows the flaperon deflections.

The pitch attitude responses in Figure 5.4a are very similar as we predicted. The TITO response has slightly less overshoot and smaller steady state error. The angle of attack responses, shown in Figure 5.4b, are quite different. The TITO system has virtually zero angle of attack after 0.5 sec, while the angle of attack for the SISO system is drifting off at approximately 1 deg/sec.

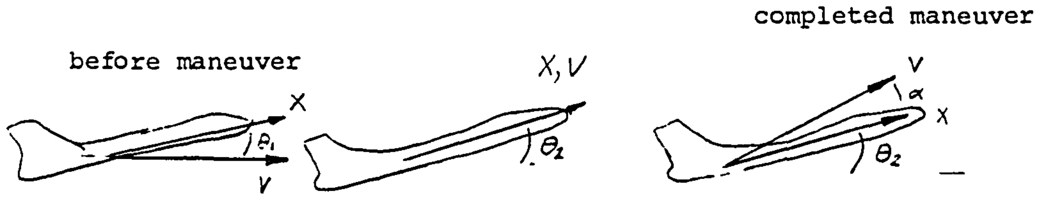

a. SISO command pitch attitude only; continuously decreasing angle of attack (Design B)

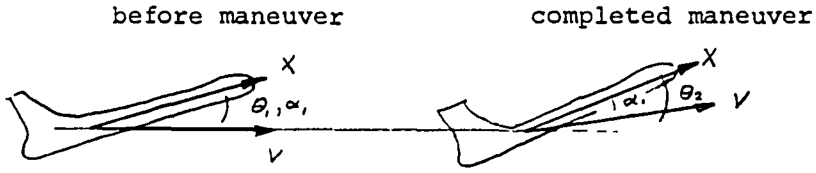

$\theta_1 = \theta_2$

b. TITO Direct Lift Mode (Design C)

Figure 5.3 Schematic of Aircraft Response comparing Design B and Design C

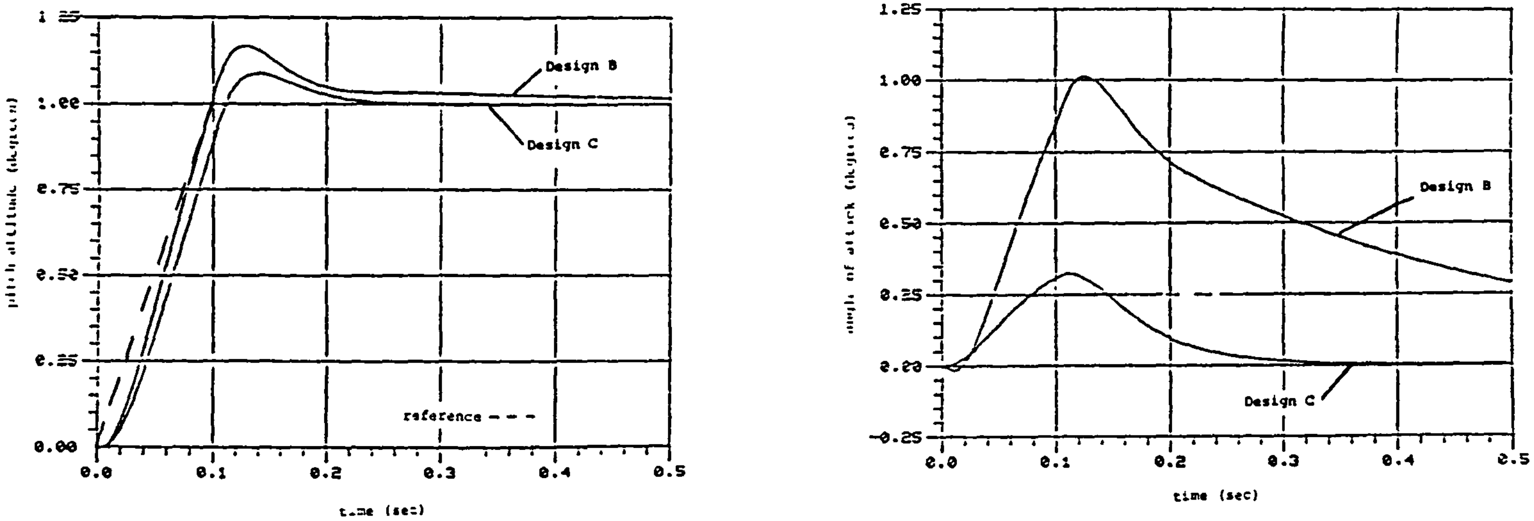

a. Pitch Attitude

b. Angle of Attack

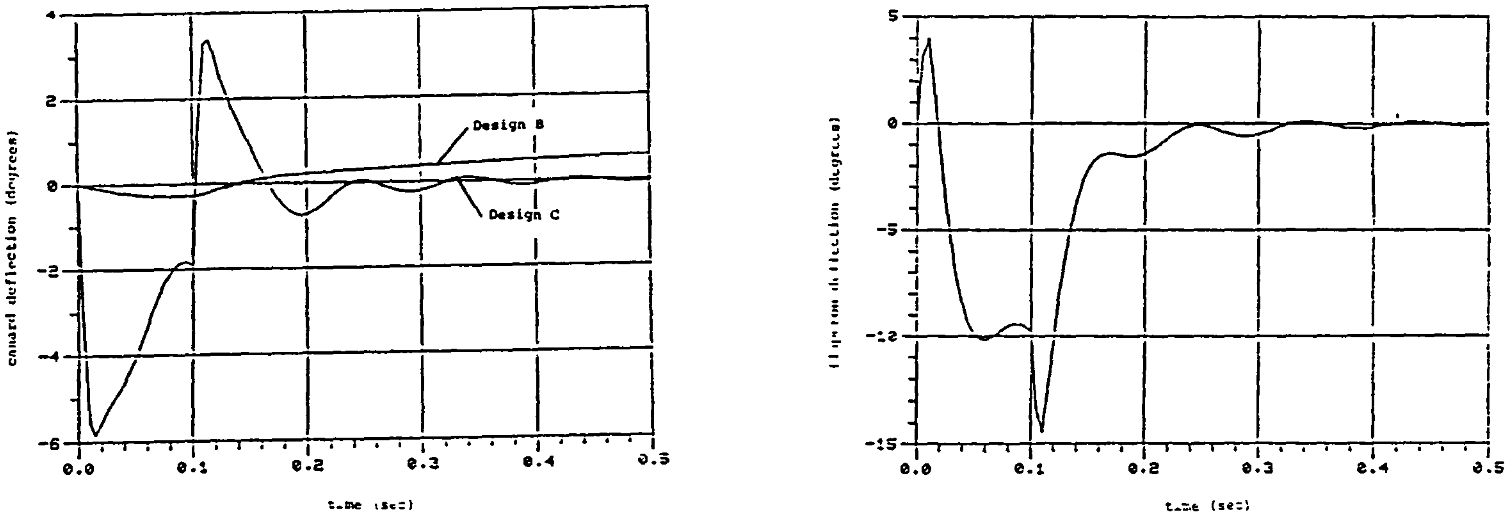

c. Canard Deflections

d. Flaperon Deflections

Figure 5.4 Direct Lift Mode
Compare Performance of Designs B and C

The canard deflections of the two systems are quite different. In Design B in order to maintain the commanded pitch attitude, the canard must continuously increase its deflection and will eventually saturate. This in turn causes the angle of attack to continuously decrease and the flight path angle to increase. Since the angle of attack is decreasing, the additional lift is being generated by the canard. The behavior of the TITO system (Design C) is quite different. Figure 5.4c and 5.4d show the canard and flaperon deflections. Initially the canard has a large negative deflection and the flaperon a small positive deflection followed by a very large negative flaperon deflection and a relatively large canard deflection. After some small oscillations, both acutators virtually return to their trim deflections. In this case, once the aircraft is pitched up to its commanded attitude by the coordinated flaperon and canard deflections, only a slight change in deflection is necessary to generate the additional lift needed for the aircraft to continue to fly up. All the action takes place in changing the attitude, very little is needed to maintain the new attitudes.

In order to follow these commanded inputs the flaperon had to deflect beyond its allowed range. The maximum change in deflection in the negative direction is -6.95°. Based on this simulation, the allowed input commands in the direct lift mode are in the range $-1^\circ < \theta_c < 0.5^\circ$. Larger commands will cause the flaperon to saturate.

5.2.3 Pitch Pointing Mode (Design C Only)

The pitch pointing mode requires the simultaneous command of angle of attack and pitch attitude. The same commands are given in both channels, thus the flight path angle does not change. The pitch pointing mode is neither in the angle of attack direction or the pitch attitude direction, but at 45° in the α_c, θ_c plane. Based on the directionality ellipse in Figure 4.10, we expect the command following error to be approximately 9%.

Figure 5.5 shows the simulation results for commanded pitch and angle of attack inputs which were ramped for 0.1 sec up from 0° to 0.7071° where they remained. Over the simulation $\theta_c = \alpha_c$ and $\gamma = 0°$, and for $t > 0.1$ sec, $\theta_c = \alpha_c = 0.7071°$. Figure 5.5a shows the angle of attack response, 5.5b shows the pitch attitude, 5.5c shows the canard deflections and 5.5d shows the flaperon deflection.

The square root of the sum of the squared angle of attack deviation and the squared pitch attitude deviation is 0.082° or 8%, which is near the predicted error of 9%. Figures 5.5a and b show that the steady state angle of attack is slightly below the commanded input while the pitch attitude is slightly above it.

The coordination of the flaperon and canard can be seen in Figures 5.5c and d. Initially, the canard deflects negatively and the flaperon positively followed by positive canard deflection and negative flaperon deflection. The maneuvers give the aircraft a positive pitching moment and

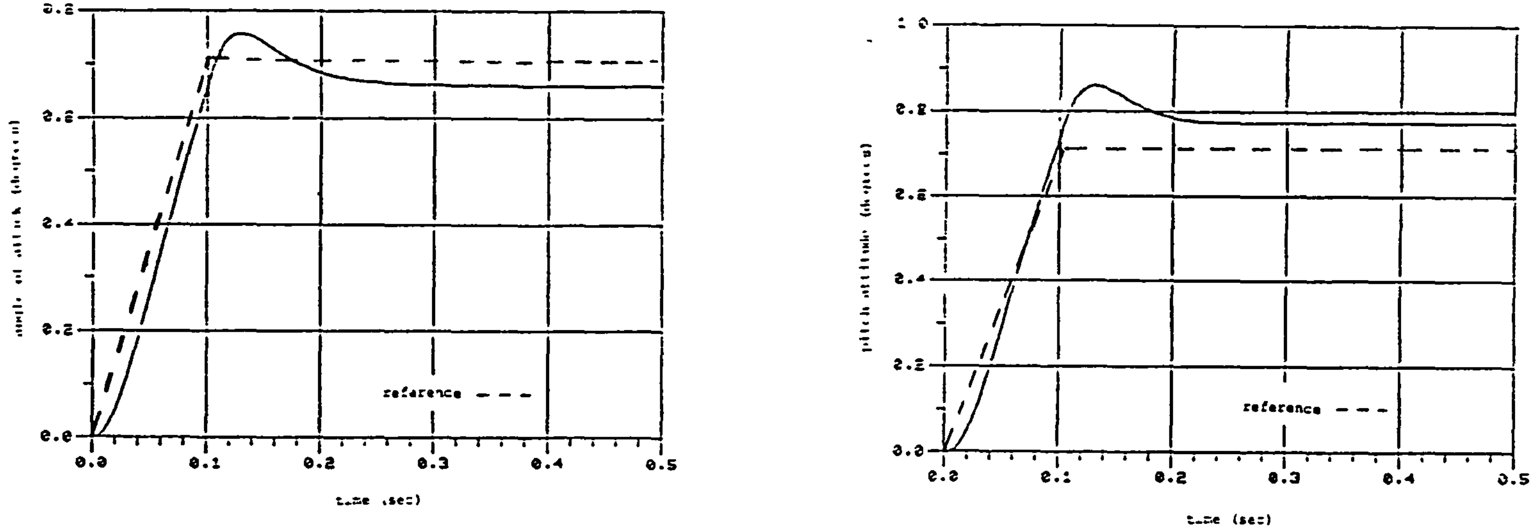

a. Angle of Attack

b. Pitch Attitude

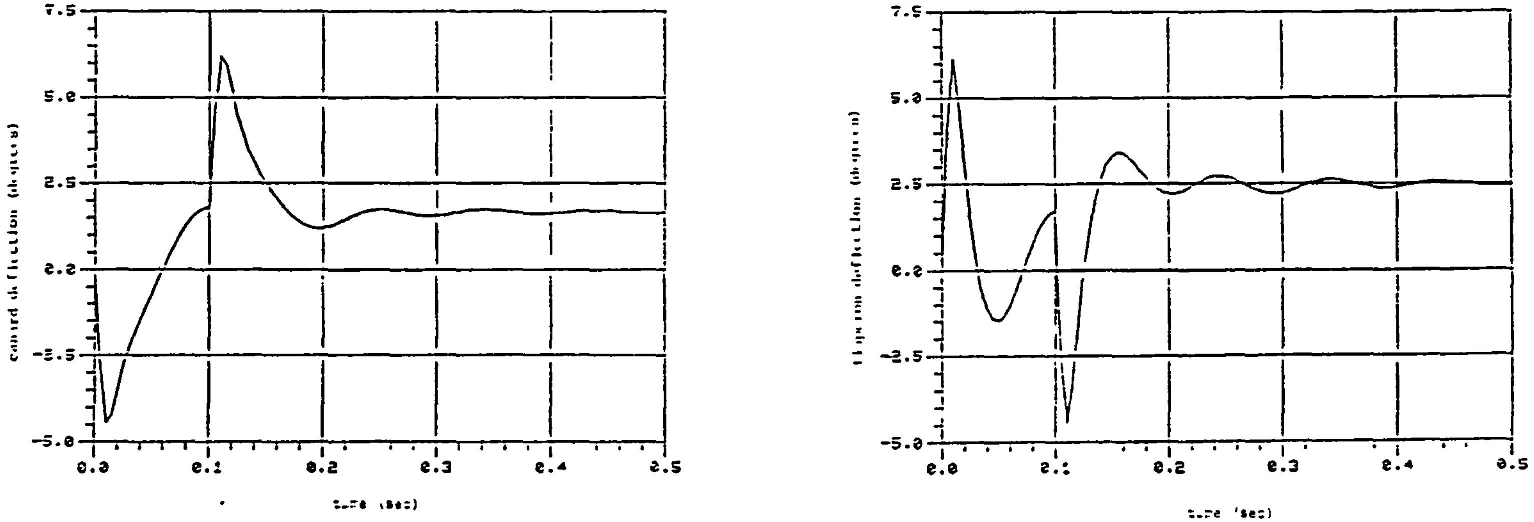

c. Canard Deflections

d. Flaperon Deflections

Figure 5.5 Pitch Pointing Mode (Design C only) a positive angle of attack. In order to maintain the commanded pitch attitude, both actuators deflect positively, balancing their pitching moments about the cg. In order to maintain the flight path despite the increased angle of attack, the control surfaces must also generate a negative lift.

The allowed command inputs, in the pitch pointing mode, which will not saturate the flaperon are $-0.8° < \alpha_c = \theta_c < 1.2°$. Larger command inputs will require too large a change in the flaperon deflections.

5.2.4 Alternate Mode (Design C Only)

For completeness, we also examined a mode whose reference inputs are 90° from the pitch pointing mode in the α_c, θ_c plane. In this case $\alpha_c = -\theta_c$ and the flight path angle is twice the commanded pitch attitude. Figure 5.6a is a sketch of the aircraft coordinates in this mode.

The reference inputs were ramped for 0.1 sec from 0° to their final values of -0.7071° for pitch command and +0.7071° for angle of attack. The responses are shown in Figures 5.6b and c, angle of attack and pitch attitude respectively. The canard and flaperon deflection are shown in Figure 5.6d.

The mean square error is 8%, as it was in the pitch pointing case. This is consistent with the singular value directionality analysis. Since both this mode and the

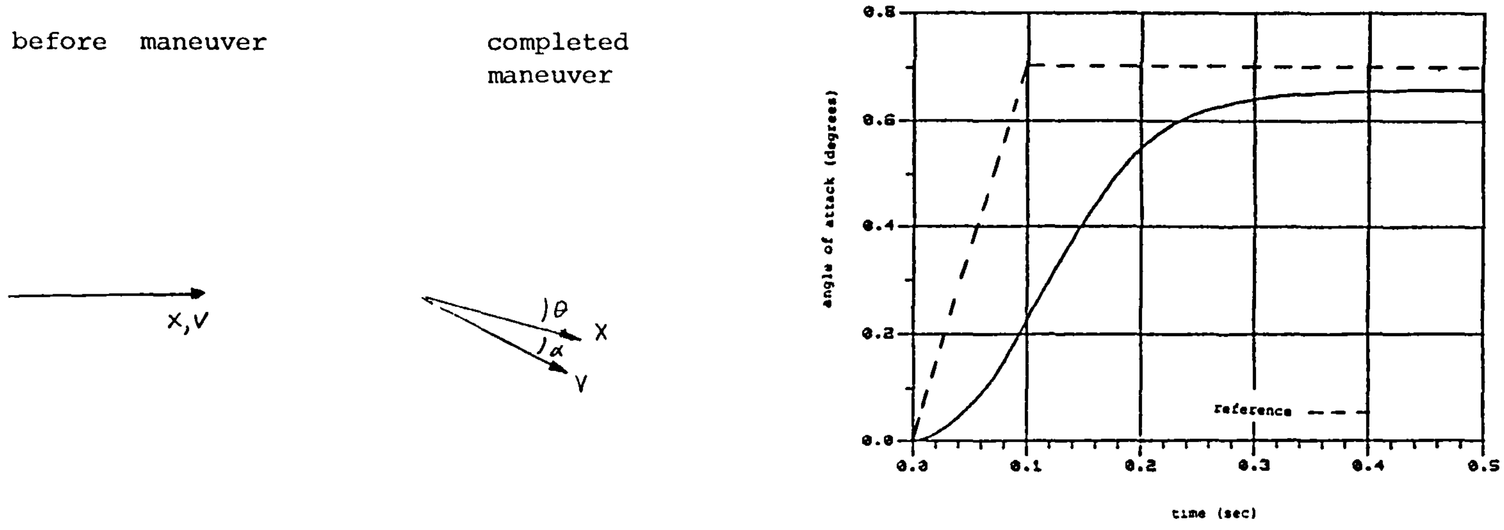

a. Schematic of Aircraft Response

b. Angle of Attack

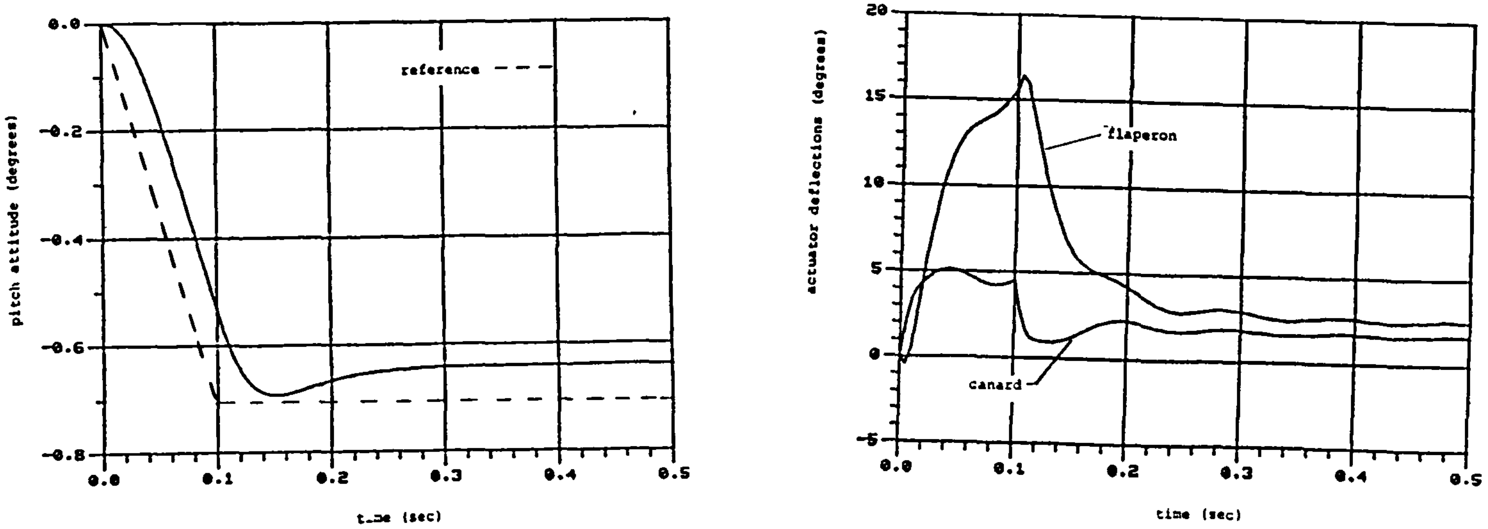

c. Pitch Attitude

d. Actuator Deflections

Figure 5.6 Alternate Mode (Design C only) pitch pointing mode are halfway between the maximum and minimum accuracy directions as shown in Figure 4.10, the command following error should be the same, and it is. Figure 5.6b shows that the angle of attack does not reach the commanded value of 0.7071°. Comparing the angle of attack response in this mode to the angle of attack response in the pitch pointing mode (Figure 5.5a), we see that after 0.5 sec, both have reached the same angle 0.66°. The pitch attitude in Figure 5.6c does not quite reach its commanded input, but levels off at -0.64°.

Figure 5.6d shows both the canard and flaperon deflections. In this case, both actuators have a large positive deflection initially and settle out at smaller positive deflections. The positive canard and flaperon deflections balance each other thus the net pitching moment is zero. As in the pitch pointing mode, the actuator surfaces must also generate a negative lift in order to balance the increased lift due to the larger angle of attack. This explains why the steady state actuator deflections of this mode and the pitch pointing mode are so similar. In both cases, the pitching moment must be zero and the same increase in angle of attack (0.7071°) must be offset by negative lift generated by the control surfaces. The initial transients are somewhat different due to the different pitch attitude commands.

In this case, the allowed range of reference input commands, which will not cause the flaperon to saturate, are $-1.2° < (-\theta_c = \alpha_c) < 0.3°$. Larger commands will require the flaperon to deflect beyond its allowed range of $-6.95° < f(t) < 28.05°$.

In addition to the coordinates, the response of the flexible wings was plotted for this mode. Figure 5.7a is the wing tip deflection and 5.7b is its bending rate. The peak deflection is ~6 inches; after 0.5 sec the wing is still bending, but the amplitude is less than 0.5 inches. The peak rate is less than 15 ft/sec; after 0.5 sec the rate drops to 0.5 ft/sec. Figure 5.7c shows the wing rotation about its elastic axis, and 5.7d shows the rate of rotation. The wing is twisting at its natural frequency of 212 rad/sec with a peak to peak amplitude of approximately 0.013° and a rate of 2.9 deg/sec. The wings displayed similar behavior in the other modes, but it was decided not to show their transients.

5.3 Summary

The usefulness of coordinated canard and flaperon control was demonstrated in this chapter. The SISO sytems with only canard control and either angle of attack (Design A) or pitch attitude (Design B) output were compared to the TITO system (Design C) in which both angles are controlled. The main conclusion is the TITO system can do what each SISO design could do as well as control the other output.

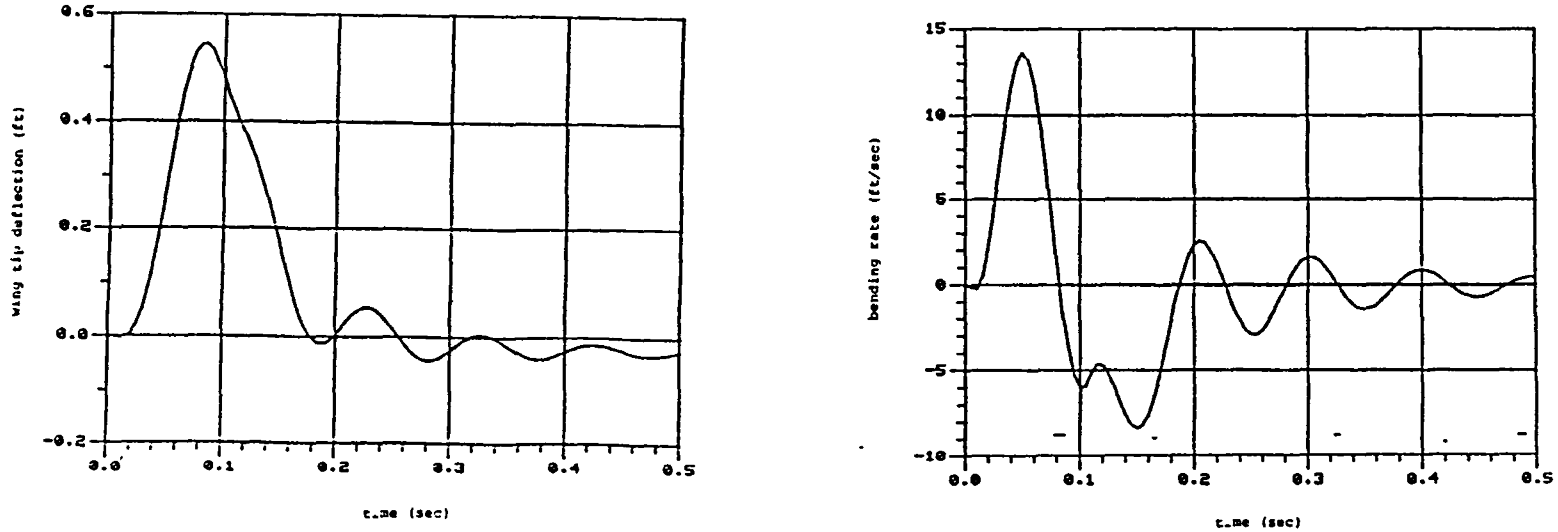

a. Wing Tip Deflection

b. Wing Tip Bending Rate

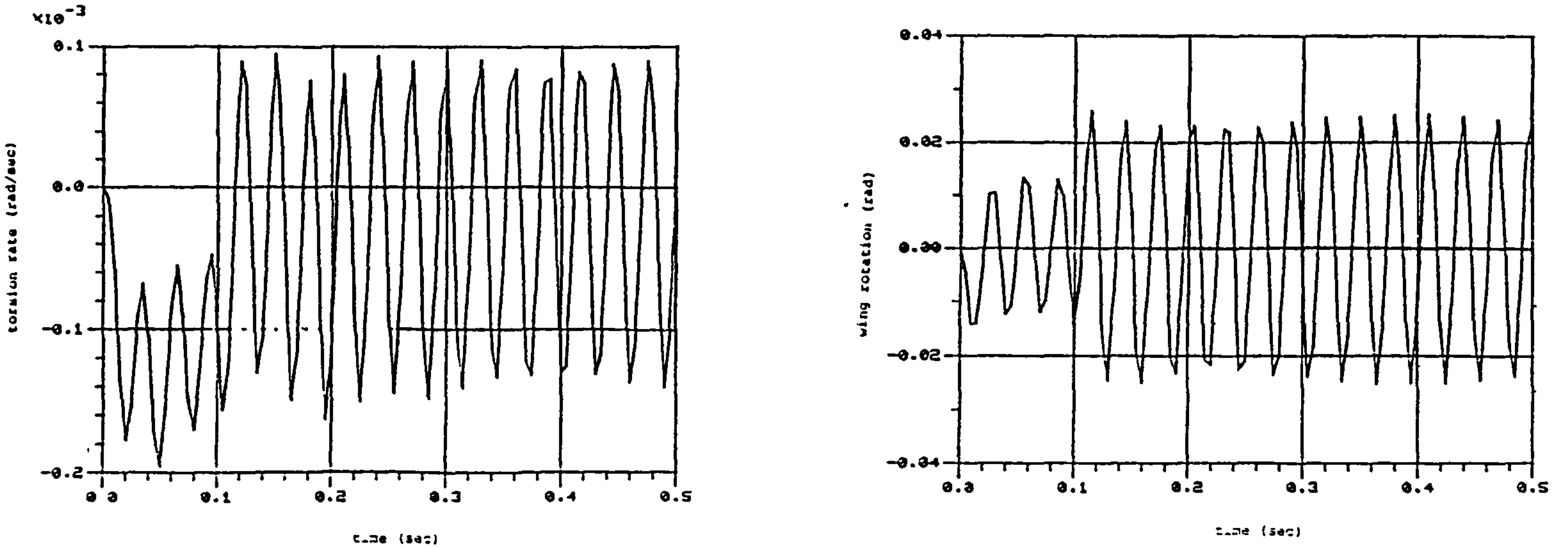

c. Wing Torsion

d. Wing Rotation Rate

Figure 5.7 Flexible Wing Response

The performance of the TITO and SISO systems were compared based on time simulations. Since the maximum singular value is in the θ direction, the SISO θ design was compared to the TITO design in the direct lift mode. Alternately the SISO α design was compared to the TITO design in the vertical translation mode. In both cases, the command following accuracies are comparable. The SISO systems could only control one output, thus the uncontrolled output tended to drift off. Any commands to the SISO systems could only be held for a short time before retrimming the aircraft.

Finally, the ranges of reference inputs which would not saturate the flaperon were estimated for the three precision control modes and the alternate mode:

vertical translation mode: $-0.6° < \alpha_c < 1.2°$
direct left mode: $-1° < \theta_c < 0.5°$
pitch pointing mode: $-0.8° < \alpha_c = \theta_c < 1.2°$
alternate mode: $-1.2° < (-\theta_c = \alpha_c) < 0.3°$

The small command range is due to the low flaperon command authority which was noted in Section 3.2.5. If the flaperon was redesigned to have more authority, the ranges would increase.

Thus, by adding flaperon control, the aircraft is able to perform in the precision control modes. The direct lift mode can be followed very accurately, while the vertical translation mode cannot be followed with much better than 10% steady state accuracy. The command input range is somewhat restricted due to the low command authority of the flaperon.

An alternate use for the flaperon is to control the wing tip bending rate. This will be briefly investigated in the next chapter.

CHAPTER 6: CONTROL OF WING TIP BENDING RATE

6.1 INTRODUCTION

The only outputs considered up to this point in the TITO design have been angle of attack and pitch attitude. It may be that the flaperon control is more effective in an alternate configuration. One such possibility is to use the flaperon and canard to actively control the wing tip bending rate and another output. The controllability analysis in Section 3.2.2 indicated that the short period mode could be controlled by the canard and the bending mode by the flaperon.

A full-state feedback (not LQG) regulator, designed to stabilize the pitch rate and control the wing tip bending rate, was described in Reference 7. The performance of this design will be examined more closely. In addition, its performance will be compared to the performance of Design C. First the performance of the two systems will be compared in the face of a wind gust, which is what the regulator in Reference 7 was designed for. Next, we will look at the regulator design from a command following point of view, examining its singular values in the frequency domain and its response to a command in pitch rate.

6.2 Control of Pitch Rate and Wing Tip Bending Rate

6.2.1 Regulator Design

The regulator design henceforth referred to as Design D, described in Reference 7 will be considered in this chapter. The design goals (in [7]) were to stabilize pitch rate and actively control the wing tip bending rate; thus no attempt was made to design a command following system. The design model used is what we have been calling the truth model. The torsion mode was not ignored. In addition, the system was not rescaled; the original system described in Section 2.3.3 was used. We should also emphasize that the compensator design was a standard LQ regulator; the LQG/LTR method was not used.

The feedback gains are listed in Appendix 2.4. Table 6.1 lists the closed loop poles. The wing bending mode damping ratio has been improved from 0.165 in the open loop plant to 0.31 in the closed loop system. The wing torsion mode damping has also increased slightly, although the mode is still very lightly damped. The plant has been stabilized. In terms of pole locations, the design goals of [7] were met.

TABLE 5.1
REGULATOR CLOSED LOOP POLES DESIGN D

		Frequency	Damping
Phugoid	$-0.0104 \pm j\ 0.0456$	0.047	0.22
Short Period	-5.256, -18.243		
Bending Mode	$-18.5 \pm j\ 57.2$	60.1	0.31
Torsion Mode	$-0.0174 \pm j\ 212.7$	212.7	8×10^{-5}

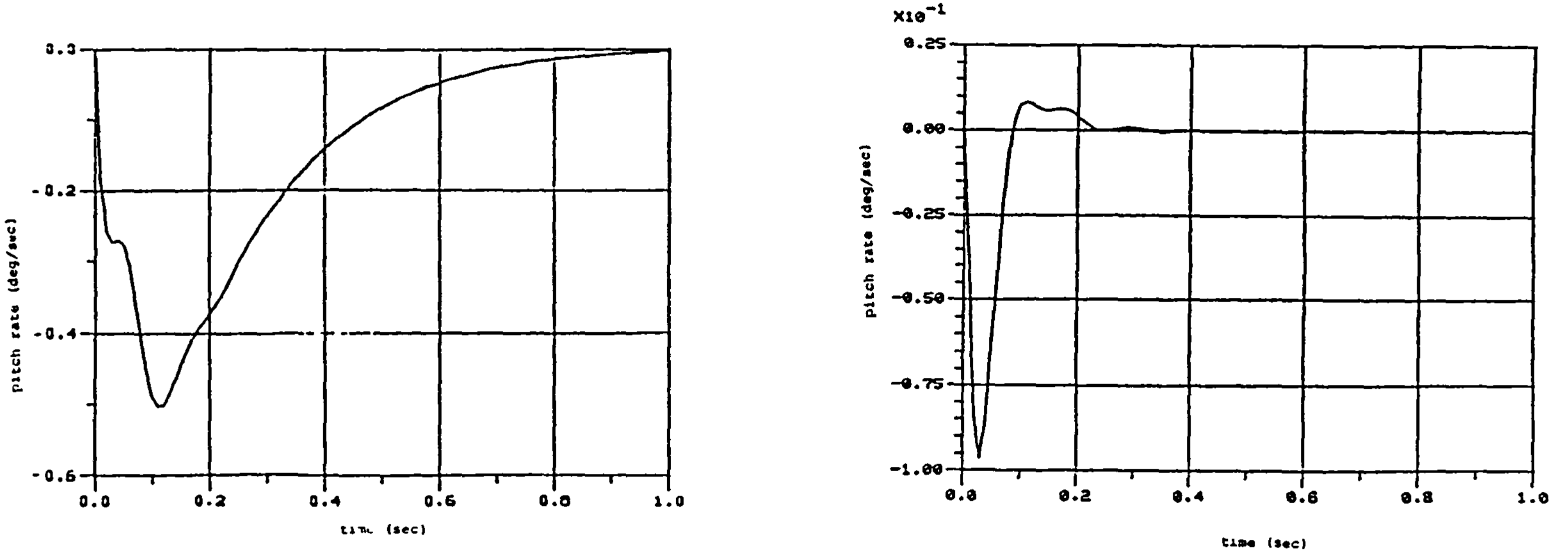

a. Design D: Pitch Rate

b. Design C: Pitch Rate

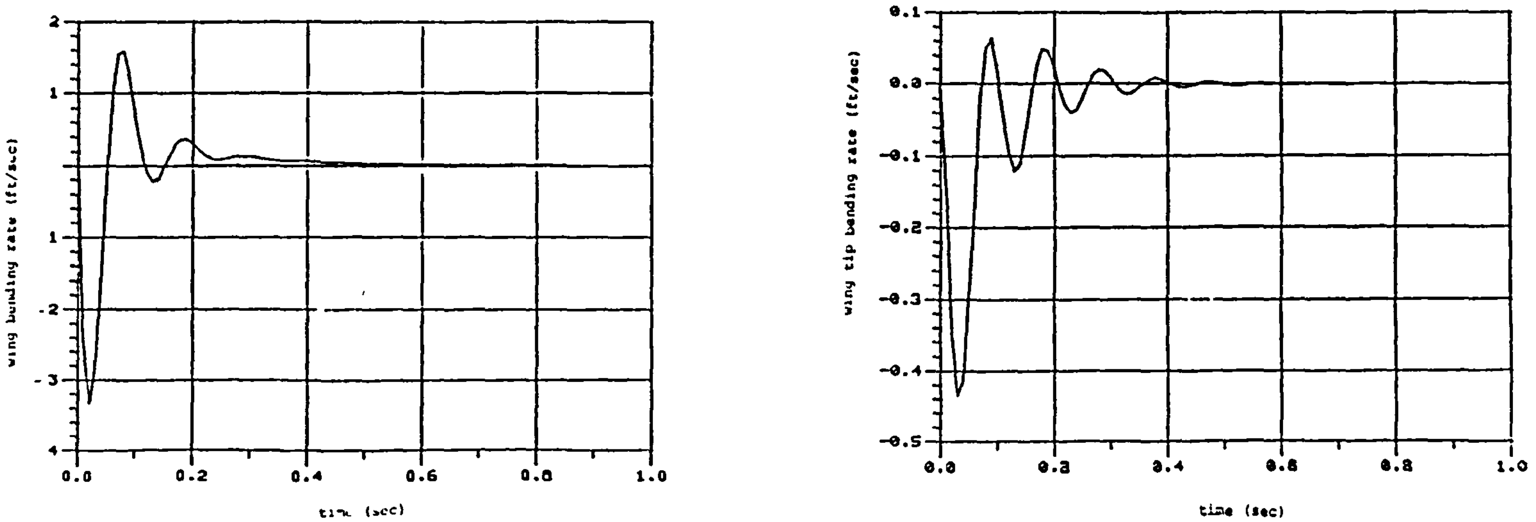

c. Design D: Wing Tip Bending Rate

d. Design C: Wing Tip Bending Rate

Figure 6.1 Response to Wind Gust
Compare Performane of Designs C and D

6.2.2 Wing Gust Response

The responses of Designs C and D to a wind gust are examined next. The wind gust was modelled as an 8.73 ft/sec vertical impulse. This translates to an initial angle of attack of 0.5°.

Figures 6.1a and b show the pitch rate response of Designs C and D . Notice, first of all, the scales are very different. Design D yields a peak pitch rate of -0.5 deg/sec, while the peak pitch rate for Design C was -0.1 deg/sec. Within approximately 0.3 sec, the pitch rate is virtually zero for Design C, although there is some overshoot. Design D exhibits a more highly damped response. The pitch rate returns to zero in about 1 sec without any overshoot.

Figure 6.1c and d show the wing tip bending rate response for Designs C and D respectively. Again, note the different scales, the wing tip for Design D reaches a peak rate of -3 ft/sec. The wing tip for Design C reaches a peak rate of -0.4 ft/sec. As with the pitch rate, the Design D response is more damped than Design C's response.

Figures 6.2a and b show the angle of attack responses for Designs C and D. The angle of attack is back to zero within 0.3 sec for Design C while it takes slightly more than 1 sec for the Design D angle of attack to return to zero.

Finally, Figures 6.2c and d show the flaperon and canard deflection for Designs C and D. Note once more the

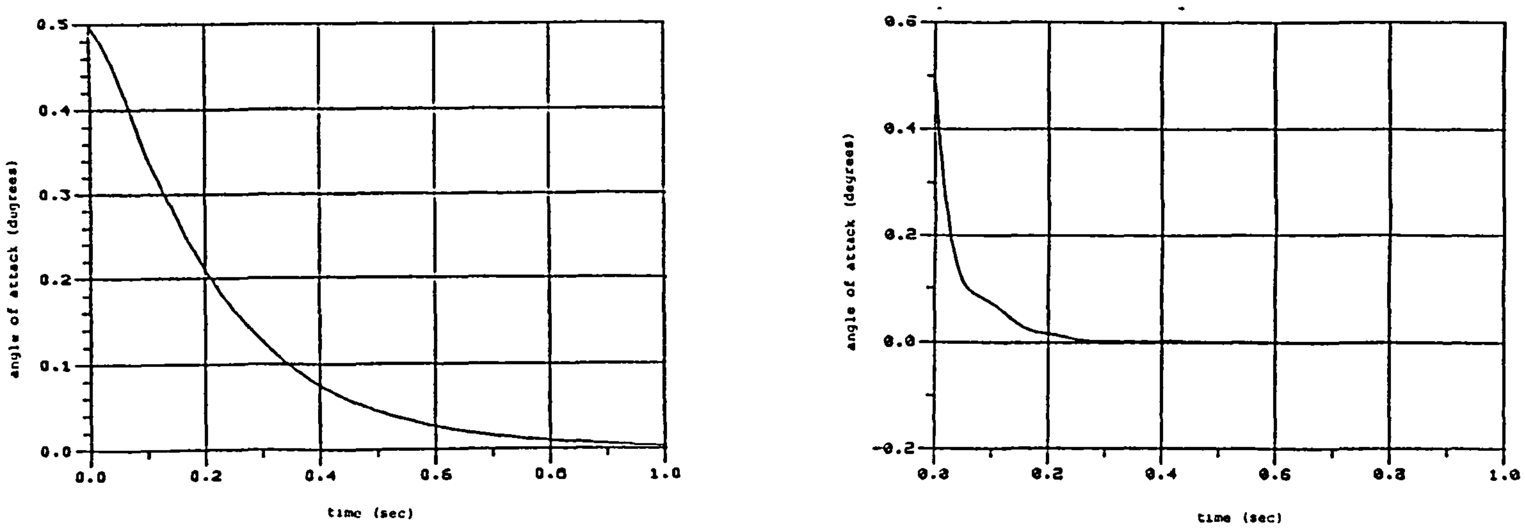

a. Design D: Angle of Attack

b. Design C: Angle of Attack

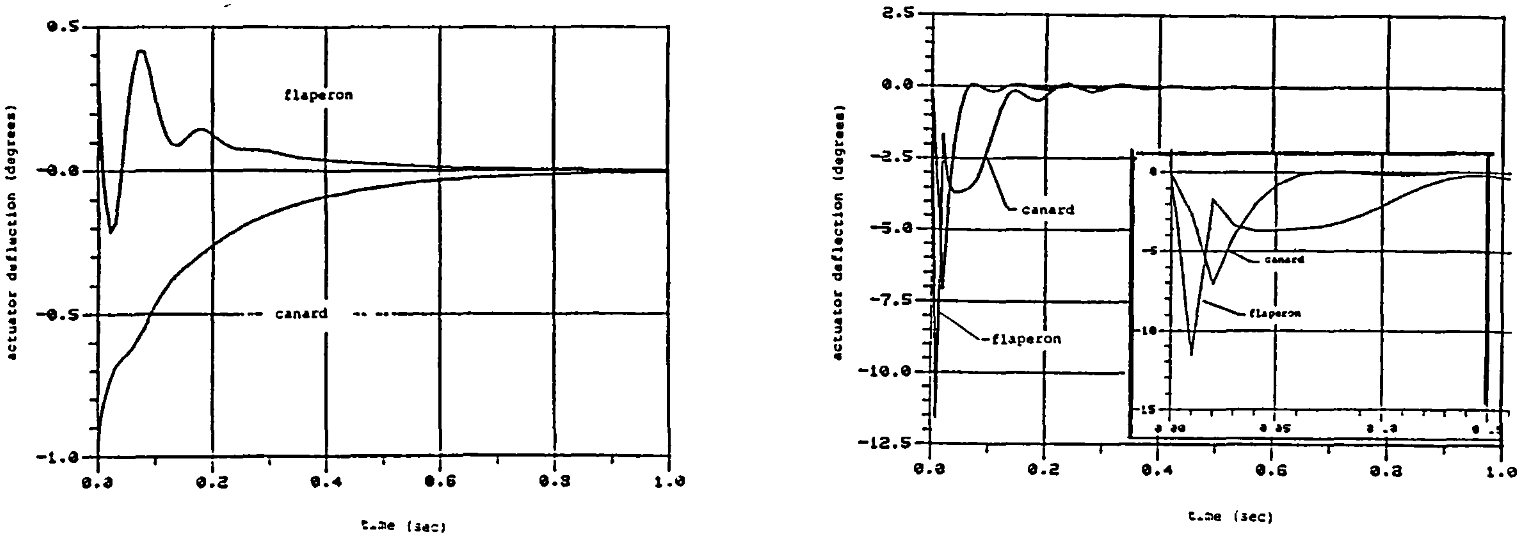

c. Design D: Actuator Deflections

d. Design C: Actuator Deflections
Inset: Blowup of 0<t<0.15sec

Figure 6.2 Response to Wind Gust (cont.)

different scales. Design C has much larger and more rapid deflections than Design D. Within 0.3 sec the actuators return to their trim setting, while Design D takes nearly 1 sec. On the other hand, the flaperon must deflect to -12° (which is beyond its limit of -6.95°) and the canard deflects to -7° with Design C. The maximum deflections for Design D are -1° for the canard and 0.4° for the flaperon.

We have seen that the design of Reference [7] does indeed stabilize the pitch rate and damp the wing tip bending rate with relatively gentle flaperon and canard control. While Design C stabilizes the pitch rate and dampens the wing tip bending rate more rapidly than Design D, quite large flaperon deflections are required and the responses tend to be more oscillatory.

6.2.3 Design D Adapted to Command Following

The regulator, Design D, must be rearranged in order to force the regulator to perform command following. Figure 6.3 is a block diagram of the regulator altered for command following. The system still requires full state feedback. The output states are compared to the reference commands and an error signal is generated.

Figure 6.4 shows the singular value curves for Design D. Figure 6.4a is a plot of the singular values of the loop broken at the plant input. This plot should be examined with respect to robustness considerations. The minimum singular value never has a gain greater than 0 db.

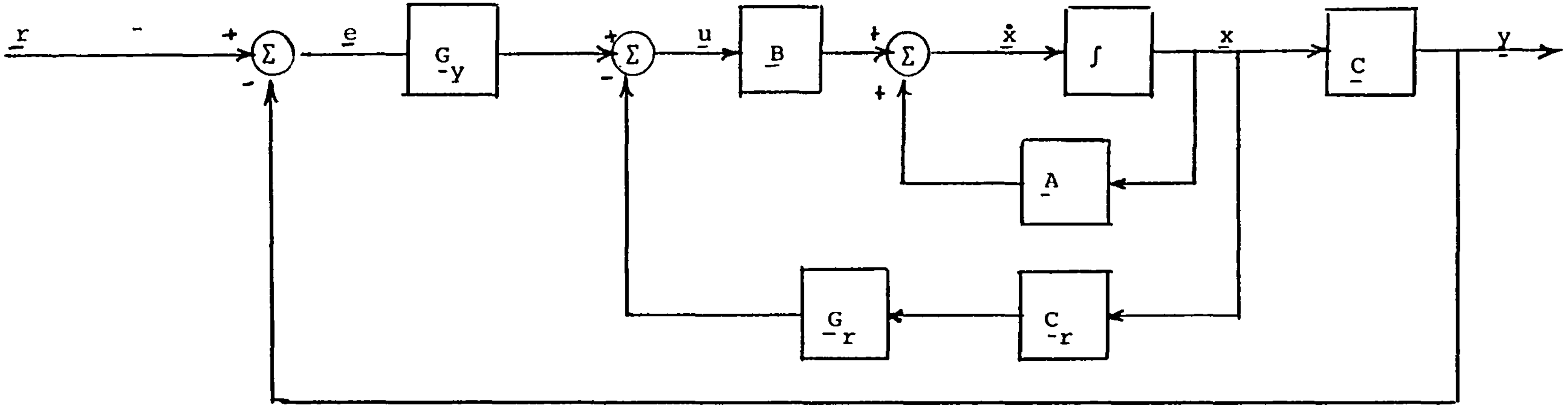

$$\underline{u} = -\,\underline{G}\,\underline{x}$$

$$= -\,[\;\underline{G}_y \quad \underline{G}_r\;]\begin{bmatrix}\underline{y}\\ \underline{x}_r\end{bmatrix}$$

Figure 6.3 Regulator problem adapted to command following.

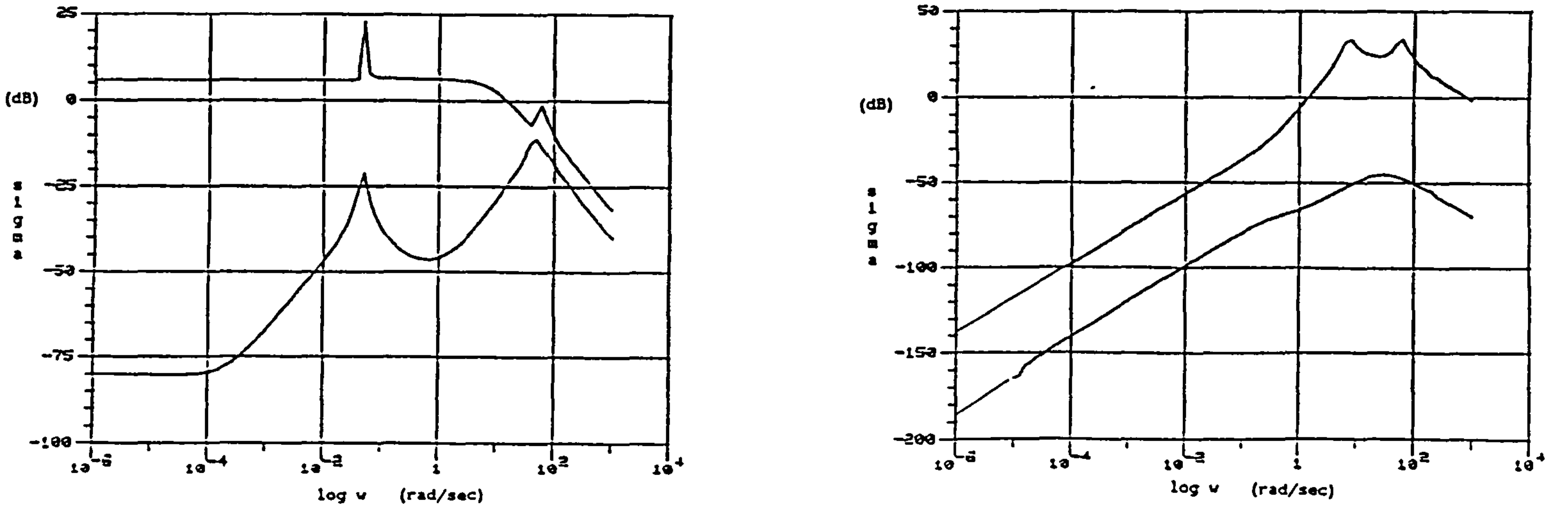

a. Loop Broken at Plant Input

b. Loop Broken at Plant Output

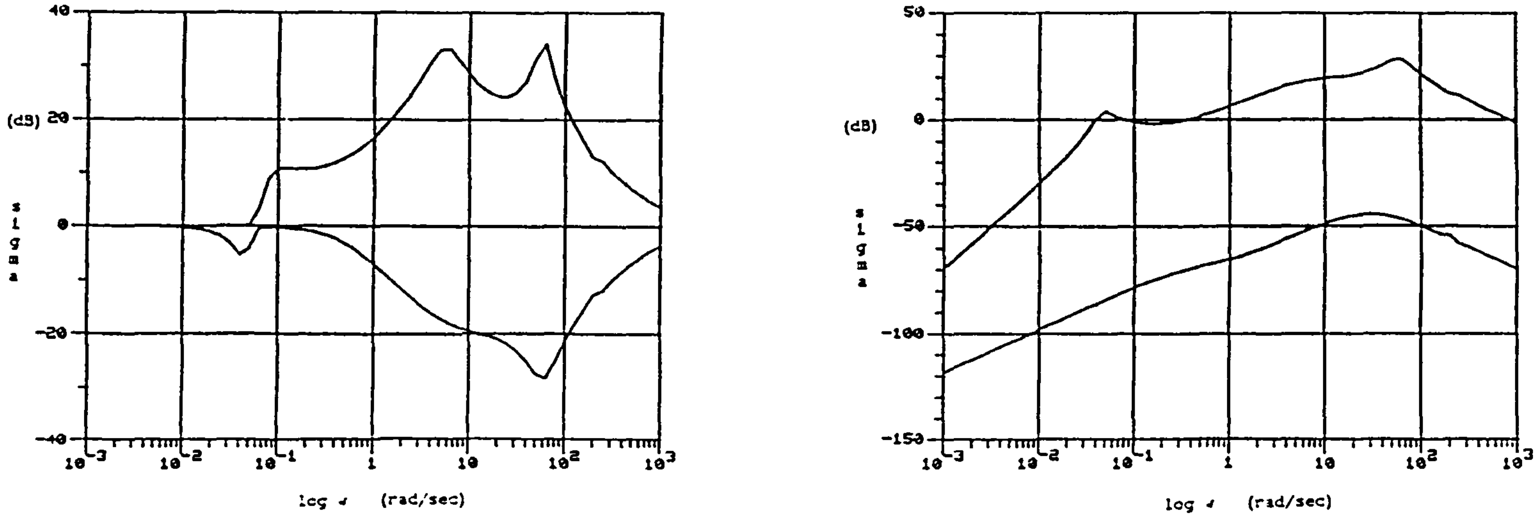

c. Loop Sensitivity

d. Closed Loop TFM

Figure 6.4 Design D: Singular Value Plots

The bandwidth is 10 rad/sec. The system should be robust to unmodelled high frequency dynamics.

Figure 6.4b is a plot of the singular values of the loop broken at the plant output. This is where we have been breaking the loop in the previous designs to understand command following performance. The outputs are pitch rate and wing tip bending rate. This plot, along with Figure 6.4c, the loop sensitivity, is useful when considering the command following performance. Again, the minimum singular value of both loops is never greater than 0 db. In terms of command following, the maximum singular value of the loop sensitivity has a gain greater than 1 only in the frequency range $0.1 < w < 10^3$.

The closed loop transfer function is shown in Figure 6.4d. The crossover frequency is approximately 1000 rad/sec. In order to actively control the bending mode at 60 rad/sec, it is necessary to have a bandwidth greater than 60 rad/sec. The high bandwidth is reasonable from that standpoint, but may cause difficulties with respect to high frequency noise or other unmodelled flexible wing modes and actuator dynamics.

Figure 6.5 shows the system response to a reference input in <u>pitch rate</u>. The pitch rate command was ramped-up from 0 to 1°/sec over 0.1 sec and remained 1°/sec after 0.1 sec. The wing tip bending rate was commanded to zero. Figure 6.5a is a plot of the pitch rate response and 6.5b is a plot of the wing tip bending rate response. The wing

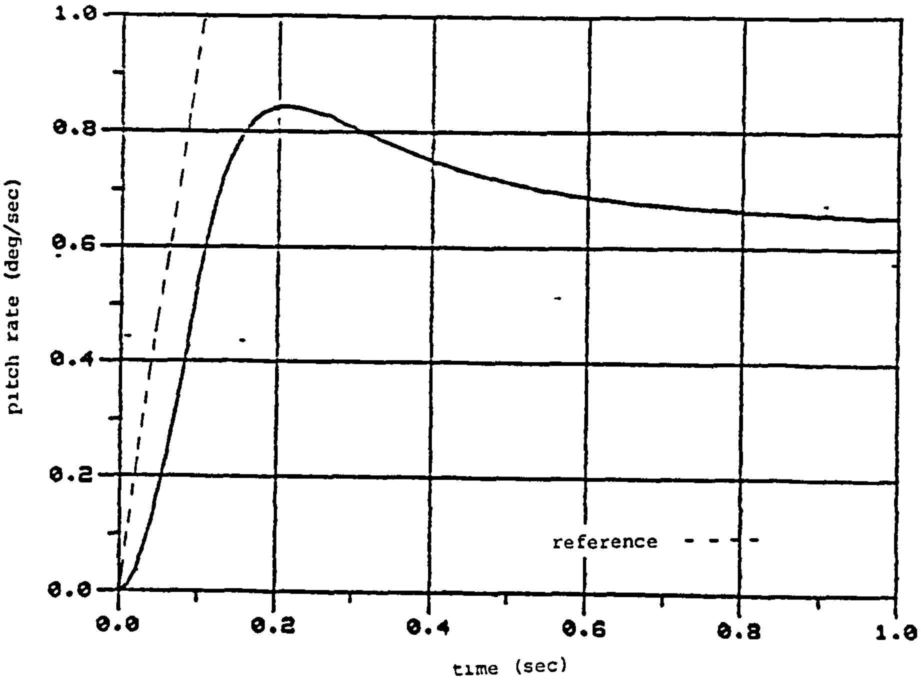

a. Pitch Rate

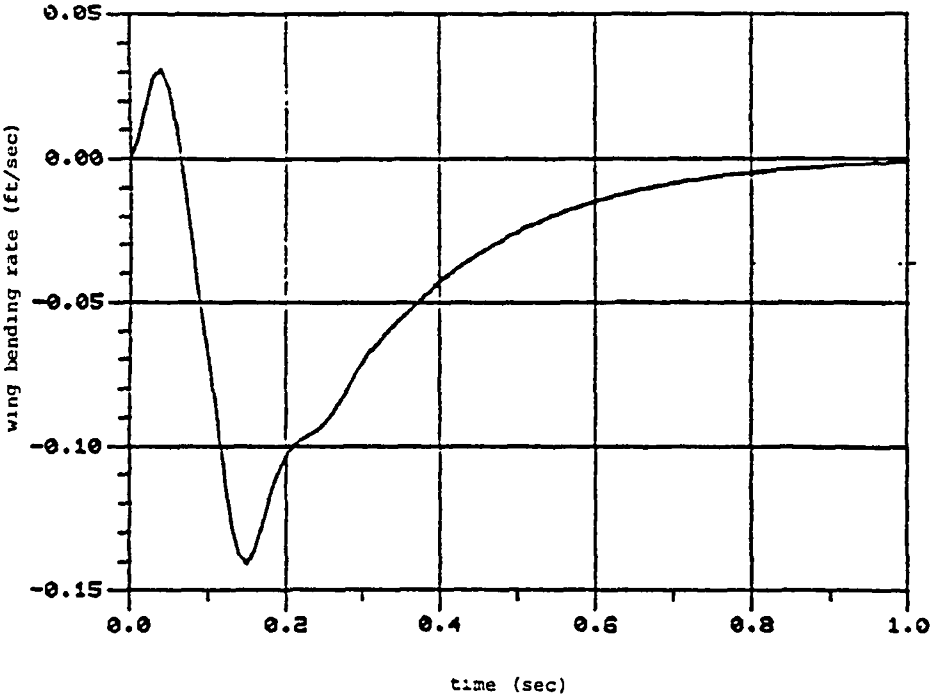

b. Wing Tip Bending Rate

Figure 6.5 Design D: Command Following Performance tip bending rate reaches virtually zero within 1 sec. However, the pitch rate settles at 0.65 deg/sec, which is 35% in error.

6.3 Summary

The full-state feedback regulator design, taken from Reference 7, is fine in terms of closed-loop pole locations. The plant is stabilized and the wing tip bending mode damping ratio is increased. However, when considering command following, the design is inadequate. The response to a wind gust disturbance is fairly good; the disturbance is damped out within 1 sec without violent actuator deflections. Design C responds much more quickly to wind gust disturbances; the disturbance is damped out within 0.4 sec. However, the canard and flaperon must be deflected quite rapidly and in the case of the flaperon, beyond its saturation limit.

Active control of the wing tip bending rate by the flaperon presents an interesting possibility. However, it is not a trivial matter to design a compensator to independently control one of the attitude coordinates (i.e. angle of attack, pitch attitude or pitch rate) and the wing tip bending rate as we have seen in this chapter. In the first place, an accurate high frequency model is necessary, at least the first two flexible modes must be included. Furthermore, there's approximately a decade separation between the maximum and minimum singular values. It may be more desirable to preserve the fast and slow loops, by designing a fast loop compensator with flaperon input and wing tip bending rate output and a slow loop compensator, with canard input and an attitude angle output. [19].

CHAPTER 7: SUMMARY, CONCLUSIONS AND DIRECTIONS FOR FURTHER RESEARCH

7.1 Summary and Conclusions

7.1.1 Summary

The goal of this study was to determine the effectiveness of independent flaperon and canard control. The main emphasis was on control of angle of attack and pitch attitude, the so called precision control modes. In order to examine the usefulness of the flaperon, two SISO systems with canard control only were compared to the TITO system with canard and flaperon control.

The linear model of a generic forward swept aircraft which included two flexible modes was developed in Reference 7. The design model used here is based on the original model. The model was rescaled and the torsion mode was dropped. The model error, used to form a stability-robustness test, is based on the relationship between the design model and the truth model. The designs were tested on the truth model.

Prior to the actual compensator design, the linear model was analyzed. The model analysis showed the unstable pole at 7.3 rad/sec is in the short period mode. The controllability analysis indicated that the first bending mode is controllable through the flaperon. This suggested an alternate output configuration, using the flaperon to control the wing tip bending rate. The transfer matrix from the controls to the angle of attack and pitch attitude output revealed that the flaperon has relatively little authority to deal with large commands before it saturates.

The design specifications are about the same for the three systems: SISO with canard control and angle of attack output (Design A), SISO with flaperon control and pitch attitude output (Design B), and TITO with both canard and flaperon control and pitch attitude and angle of attack output (Design C). The design specifications are based on performance and robustness considerations. The LQG/LTR design methodology was used to design the three compensators.

7.1.2 Conclusions

The main conclusion is that the TITO system can do what the SISO systems could, and more. The command following performance of the SISO systems' controlled output (α for Design A and θ for Design B) is comparable to the command following of the TITO system in the appropriate mode. While the TITO system was able to maintain a small pitch attitude due to the flaperon control, the pitch attitude of the SISO system drifted off at a rate of approximately 3 deg/sec. The performance of the TITO system in the direct lift mode was compared to the Design B's performance. In this case, the error in pitch attitude for the SISO system was about 2% while the TITO system had an error of less than 0.5%. Furthermore, while angle of attack drifted off at a rate of -1°/sec with the SISO system, the flaperon enabled the TITO system to maintain its angle of attack heading.

Due to the limited command authority of the flaperon, the command inputs must be limited in order to avoid saturating the actuator.

An alternate use for independent canard and flaperon control is to actively control the wing tip bending rate and an attitude coordinate such as pitch attitude or angle of attack. The actual design of such a compensator is not trivial. An additional difficulty is that an accurate model of the high frequency dynamics is necessary. Flexible wing modes are quite difficult to model accurately.

7.2 Suggestions for Future Research

This study has examined the independent canard and flaperon control of angle of attack and pitch attitude. Other uses for the flaperon control should also be investigated, including active control of the wing tip bending rate. Furthermore, the impact of sensor and actuator dynamics should be examined.

REFERENCES

[1] Kaplan, G. "The X-29: Is it Coming or Going?" IEEE Spectrum. June 1985.

[2] Gilbert, M.G., D. Schmidt, T.A. Weisshaar. "Quadratic Synthesis of Integrated Active Controls for an Aeroelastic Forward Swept Wing Aircraft." AIAA Paper No. 82-1544.

[3] Spacht G. "The Forward Swept Wing: A Unique Design Challenge." AIAA Aircraft Systems Meeting. Anaheim, CA. August 4-6, 1980.

[4] Krone, N.J. "Divergence Elimination with Advanced Composites." AIAA 1975 Aircraft Systems and Technology Meeting. Los Angeles, CA. August 4-7, 1975.

[5] Drone, N.J. "Forward Swept Wing Flight Demonstrator." AIAA Aircraft Systems and Technology Meeting. Anaheim, CA. August 4-6, 1980.

[6] Drone, N.J. Divergence Elimination with Advanced Composites. PhD Thesis, University of Maryland. December 1974.

[7] Gilbert, M. Dynamic Modeling and Active Control of Aeroelastic Aircraft. Master's Thesis, Purdue University. December 1982.

[8] Hertz, T., M. Shirk, R. Ricketts, and T. Weisshaar "On the Track of Practical Forward Swept Wings." Astronautical and Aeronautics. January 1982.

[9] Weisshaar T. and T. Zeiler "Flutter of Forward Swept Wings, Analyses and Tests." AIAA Paper No. 82-D646. May 1982.

[10] Weisshaar T. and T. Zeiler "Dynamic Stability of Flexible Forward Swept Wing Aircraft." AIAA Paper No. 82-1325. August 1982.

[11] Innocenti, M. and Schmidt D. "Quadratic Optimal Control Synthesis with Flight Control Application." Journal of Guidance and Control. Vol. 7, No. 2. March - April 1984.

[12] Athans, M. et al. Class Notes 6.232. MIT, January 1984

[13] Mordoff, K.F. "Grumman Competes Its X29-A Tests." Aviation Week & Space Technology. March 11, 1985.

REFERENCES

[14] Aviation Week & Space Technology. February 18, 1985.

[15] Merkel, P. and R. Whitmoyer. "Development and Evaluation of Precision Control Modes for Fighter Aircraft." AIAA Guidance and Control Conference. San Diego, CA. 1976. Paper No. 76-1950.

[16] Safanov, M.G., A.J. Laub, G.L. Hartmann. "Feedback Properties of Multivariable Systems: The Role and Use of the Return Difference Matrix." IEEE Transactions on Automatic Control. Vol. AC-26, No. 1 February 1981.

[17] Roskam, J. Flight Dynamics of Rigid & Elastic Airplanes, Parts I & II. USA. 1972.

[18] Lehtomaki, N.A. Practical Robustness Measures in Multivariable Control System Analysis. PhD Thesis. MIT. May 1981.

[19] Haiges, K. Multivariable Flight Control with Time-Scale Separation. Master's Thesis. MIT. May 1984.

[20] Stein, G. Personal Communication

[21] Doyle, J. and G. Stein. "Multivariable Feedback Design: Concepts for a Clasical/Modern Synthesis." IEEE Transactions on Automatic Control. February 1981.

APPENDIX 1; LINEAR MODEL ANALYSIS

1.1 Truth Model, A and B Matrices
    Vibration Mode Shape for Flexible Wing

1.2 Scaling Matrices
    Scaled A and B Matrices

1.3 Eigenvectors of Scaled Model

1.4 Singular Value Decomposition at DC and w=1 rad/sec

Generic Forward-Swept Wing Model

```
A Matrix

 5 2660E-04  5 3150E+00 -3.2200E+01 -1 4530E+01 -1 4050E-01  1 5070E-03   2 7430E+00  1 9840E-05
-6.4380E-05 -2.8810E+00 -4 6720E-04  1 0060E+00  7 6270E-02 -8 1820E-04  -1.4890E+00 -1.0770E-05
 0.0000E+00  0 0000E+00  0.0000E+00  1 0000E+00  0 0000E+00  0 0000E+00   0 0000E+00  0 0000E+00
 2.0330E-06  7.9560E+01  1.4750E-05 -8.3110E-01 -1 0550E+00  1.7620E-02   2.5010E+01  1 4580E-03
 0 0000E+00  0 0000E+00  0.0000E+00  0.0000E+00  0 0000E+00  1 0000E+00   0.0000E+00  0.0000E+00
-9 4390E-01 -3.1160E+04 -6.7790E-05  6.6400E+01 -3 6240E+03 -2 0640E+01  -2.8050E+04  3 8550E-02
 0 0000E+00  0 0000E+00  0.0000E+00  0 0000E+00  0.0000E+00  0.0000E+00   0.0000E+00  1 0000E+00
 3.3630E-03  7 5090E+01 -1.5640E-05 -6 4300E-01 -7 6250E-02 -8 1300E-04  -4 5240E+04 -3.6000E-02
```

```
B matrix
 5 8710E+00  9.4070E-01
-4 6270E-01 -5 1080E-01
 0 0000E+00  0.0000E+00
-1 9440E+01  6 1330E+01
 0.0000E+00  0 0000E+00
-6 2000E+03  2.8170E+02
 0 0000E+00  0.0000E+00
 1.3380E+00  6 4990E+01
```

Vibration Mode Shape (Reference 7)

Parameter	Mode 1		Mode 2	
Frequency ω_i (rad/sec.)	69.53		212.94	
Gen. Mass M_i (slug)	14.0		113.0	
Gen. Stiffness K_i (lb/ft)	67680.0		5124000.0	
Node	ϕ_z (ft)	ϕ_β (rad)	ϕ_z (ft)	ϕ_β (rad)
1 (wing root)	-0.041	0.002	-0.003	-0.002
2	-0.025	-0.009	-0.001	0.154
3	0.023	-0.019	0.000	0.307
4	0.098	-0.027	0.000	0.453
5	0.195	-0.034	0.000	0.587
6	0.309	-0.039	0.000	0.707
7	0.436	-0.042	0.000	0.809
8	0.572	-0.045	0.000	0.891
9	0.713	-0.046	-0.001	0.951
10	0.856	-0.046	-0.002	0.988
11 (wing tip)	1.000	-0.046	-0.003	1.000

Appendix 1.2

Scaling Matrices

S_x

$$\begin{bmatrix} 1. & & & & & & & \\ & 57.3 & & & & & & \\ & & 57.3 & & & & 0. & \\ & & & 57.3 & & & & \\ & & & & 1. & & & \\ & 0. & & & & 1. & & \\ & & & & & & 1. & \\ & & & & & & & 1. \end{bmatrix}$$

S_u

$$\begin{bmatrix} 57.3 & \\ & 57.3 \end{bmatrix} \begin{bmatrix} 1/12 & \\ & 1/30 \end{bmatrix} = \begin{bmatrix} 4.775 & \\ & 1.91 \end{bmatrix}$$

$S_y = S_x$

```
Scaled A and B Matrices

A Matrix

 5.2660E-04  9.2764E-02 -5.6200E-01 -2.5360E-01 -1.4050E-01  1.5070E-03   2.7430E+00  1.9840E-05
-3.6887E-03 -2.8810E+00 -4.6720E-04  1.0060E+00  4.3699E+00 -4.6879E-02  -8.5313E+01 -6.1708E-04
 0.0000E+00  0.0000E+00  0.0000E+00  1.0000E+00  0.0000E+00  0.0000E+00   0.0000E+00  0.0000E+00
 1.1648E-04  7.9560E+01  1.4750E-05 -8.3110E-01 -6.0447E+01  1.0096E+00   1.4330E+03  8.3537E-02
 0.0000E+00  0.0000E+00  0.0000E+00  0.0000E+00  0.0000E+00  1.0000E+00   0.0000E+00  0.0000E+00
-9.4390E-01 -5.4384E+02 -1.1832E-06  1.1589E+00 -3.6240E+03 -2.0640E+01  -2.8050E+04  3.8550E-02
 0.0000E+00  0.0000E+00  0.0000E+00  0.0000E+00  0.0000E+00  0.0000E+00   0.0000E+00  1.0000E+00
 3.3630E-03  1.3106E+00 -2.7297E-07 -1.1222E-02 -7.6250E-02 -8.1300E-04  -4.5240E+04 -3.6000E-02


B Matrix


 1.2296E+00  4.9255E-01
-5.5524E+00 -1.5324E+01
 0.0000E+00  0.0000E+00
-2.3328E+02  1.8399E+03
 0.0000E+00  0.0000E+00
-1.2985E+03  1.4750E+02
 0.0000E+00  0.0000E+00
 2.8023E-01  3.4029E+01
```

Scaled Model

(Note: Complex numbers are written with imaginary part beneath real part.)

Eigenvalues

```
7 3079E+00 -4.1612E-05 -4.1613E-05 -1.6952E-02 -1 6952E-02 -9 8719E+00 -9.8719E+00 -1.1918E+01
0.0000E+00  4.9226E-02 -4 9226E-02  2 1270E+02 -2 1270E+02  5 9117E+01 -5.9117E+01  0.0000E+00
```

Eigenvectors

```
 4 2987E-02 -7.0604E-01 -7 0604E-01 -2.2836E-05 -2 2836E-05  1 1808E-04  1.1808E-04  1.7869E-02
 0 0000E+00 -7 0276E-01  7 0276E-01  5.1164E-05 -5 1164E-05 -5 6448E-05  5.6448E-05  0 0000E+00

-9.1830E-02  9 9725E-05  9.9725E-05 -9 9191E-05 -9 9191E-05 -8 1336E-04 -8.1336E-04 -1 1750E-01
 0 0000E+00  9.6173E-05 -9.6173E-05 -1.4982E-03  1 4982E-03  1 5099E-03 -1 5099E-03  0 0000E+00

-1.3427E-01 -6 0910E-02 -6 0910E-02  1 1873E-04  1 1873E-04 -4 1910E-04 -4.1910E-04 -8.0935E-02
 0.0000E+00  6.2461E-02 -6 2461E-02 -1 1862E-05  1 1862E-05  1 8360E-05 -1 8360E-05  0 0000E+00

-9.8124E-01 -3.0722E-03 -3 0722E-03  2.5226E-03  2 5226E-03  3.0519E-03  3 0519E-03  9 6457E-01
 0.0000E+00 -3.0010E-03  3.0010E-03  2.5287E-02 -2.5287E-02 -2 4957E-02  2.4957E-02  0.0000E+00

 1.2756E-02  1.6837E-04  1.6837E-04 -2.5938E-03 -2 5938E-03 -1.0499E-02 -1.0499E-02  1.8495E-02
 0.0000E+00  1.6798E-04 -1 6798E-04  3 2846E-04 -3 2846E-04 -1 2958E-02  1.2958E-02  0 0000E+00

 9.3217E-02 -8 2709E-06 -8 2709E-06 -6.9819E-02 -6 9819E-02  8.6965E-01  8.6965E-01 -2.2042E-01
 0 0000E+00  8.2851E-06 -8.2851E-06 -5.5171E-01  5 5171E-01 -4.9274E-01  4.9274E-01  0.0000E+00

-2.4339E-06 -4.9115E-08 -4.9115E-08 -3 7953E-03 -3.7953E-03 -2 6457E-08 -2.6457E-08 -3.6575E-06
 0.0000E+00 -4.8992E-08  4 8992E-08  9 2159E-04 -9.2159E-04  8 6431E-08 -8 6431E-08  0.0000E+00

-1 7788E-05  2.5420E-09  2.5420E-09 -1 9596E-01 -1.9596E-01 -4.8482E-06 -4.8482E-06  4 3587E-05
 0.0000E+00 -2 2864E-09  2 2864E-09 -8 0726E-01  8.0726E-01 -2 4172E-06  2 4172E-06  0.0000E+00
```

Appendix 1.4

Transfer Matrices used for singular value decomposition at DC

```
                          Scaled                         Unscaled

                       g0                             g0s

                      Number of rows =  2            Number of rows =  2
                      Number of columns =  2         Number of columns =  2
transfer
matrix                 2 5460E-01 -7 7450E-01         3 0552E+00 -2 3235E+01

                      -6 8457E-02  3 3517E-01        -8 2148E-01  1 0055E+01


                       g0 sigma                       g0s sigma

                      Number of rows =  1            Number of rows =  1
                      Number of columns =  2         Number of columns =  2
singular values
                       8 8338E-01  3 6582E-02         2 5510E+01  4 5604E-01


                      g0 u                           g0s u

                      Number of rows =  2            Number of rows =  2
                      Number of columns =  2         Number of columns =  2

U matrix               9 2277E-01 -3 8536E-01         9 1862E-01 -3 9513E-01

                      -3 8536E-01 -9 2277E-01        -3 9513E-01 -9 1862E-01


                                                     g0s v
                       g0 v
                                                     Number of rows =  2
                      Number of rows =  2            Number of columns =  2
                      Number of columns =  2
                                                      1 2274E-01 -9 9244E-01
                       2 9582E-01 -9.5524E-01
V matrix                                             -9 9244E-01 -1 2274E-01
                      -9 5524E-01 -2 9582E-01
```

Transfer Matrices used for singular value decomposition at w=1 rad/sec

transfer matrix

```
aq

Number of rows =  2
Number of columns =  2

Enter xmin, xmax, xdel

x =          0.000

 2 0818E-01 -7 0042E-01
 1 8157E-02 -3.0914E-02

 1 3060E+00 -1.9316E+00
 2 6719E-01 -7 9965E-01
```

```
aqs

Number of rows =  2
Number of columns =  2

Enter xmin, xmax, xdel

x =          0 000

 2 4982E+00 -2 1013E+01
 2 1788E-01 -9 2742E-01

 1 5672E+01 -5 7949E+01
 3 2063E+00 -2 3989E+01
```

singular values

```
aq.sigma

Number of rows =  1
Number of columns =  2

Enter xmin, xmax, xdel

x =          0.000

 2 5773E+00  2 0159E-01
```

```
aqs sigma

Number of rows =  1
Number of columns =  2

Enter xmin, xmax, xdel

x =          0 000

 6 8049E+01  2 7485E+00
```

U matrix

```
aq u

Number of rows =  2
Number of columns =  2

Enter xmin, xmax, xdel

x =          0.000

 2 7231E-01  9 0700E-01
-2.7634E-02 -3.2006E-01

 9.4065E-01 -2.7360E-01
 2 0063E-01  7 6531E-03
```

```
aqs u

Number of rows =  2
Number of columns =  2

Enter xmin, xmax, xdel

x =          0 000

 3 0634E-01  8.9608E-01
-3 9690E-02 -3.1879E-01

 9 2966E-01 -3 0890E-01
 2 0078E-01  7 7754E-05
```

V matrix

```
aq.v

Number of rows =  2
Number of columns =  2

Enter xmin, xmax, xdel

x =          0 000

 5 1927E-01 -8 5461E-01

-8 4094E-01 -5 1097E-01
 1.5226E-01  9.2514E-02
```

```
aqs v

Number of rows =  2
Number of columns =  2

Enter xmin, xmax, xdel

x =          0 000

 2 3469E-01 -9 7207E-01

-9 5652E-01 -2 3093E-01
 1 7319E-01  4.1812E-02
```

(Note: imaginary part is below real part)

APPENDIX 2: COMPENSATOR GAINS

2.1 Design A

2.2 Design B

2.3 Design C

2.4 Design D

Appendix 2.1
Compensator Gain Matrices

Design A (SISO α)

H:

```
-6.3199E+00
 6.0050E+01
 7.7656E+01
 1.8516E+03
-4.1610E+00
-3.0103E+02
```

G:

```
-6 2036E-03  9.6310E+01 -7.6274E-04  1.6964E+00  6.7647E+00 -4.6306E-03
```

Appendix 2.2
Deaign B (SISO θ)

H:

```
-2 6705E+01
 4.4277E+01
 6.0458E+01
 1.8276E+03
-2.0931E+00
-2.1941E+02
```

G:

```
-1.4509E-01  3.8431E-02  9.9968E+01  3.2932E-01 -3.3809E-02  5.4979E-04
```

Appendix 2.3
Compensator Gain Matrices

Design C (TITO)

m: matching matrix

```
-2.9000E-01  6.5000E-02
-7.9000E-02 -5.0000E-02
```

H:

```
-8.0485E+00 -9.4231E+00
 3.3078E+01  1.9598E+01
 1.9598E+01  4.6351E+01
 3.9795E+02  1.2662E+03
 1.0179E+01 -1.0721E+01
 3.5161E+02  2.5209E+02
```

G:

```
4.9393E-04 -7.6933E+01 -6.3529E+01 -4.8729E-01 -5.5159E-01  5.1513E-03
5.6533E-05 -6.3450E+01  7.7227E+01  2.9781E-01 -1.3466E-01 -2.2119E-04
```

Appendix 2.4

Regulator Feedback Gains (Reference 7)

$$\begin{bmatrix} 3.5700E{-}06 & -7.5100E{-}01 & -1.4200E{-}03 & -1.2400E{-}01 & -1\ 4700E{-}02 & -2.6400E{-}03 & 0\ 0000E{+}00 & 0.0000E{+}00 \\ -1.0800E{-}05 & 1.8730E{+}00 & 9.3800E{-}03 & 2.9200E{-}01 & 1\ 4200E{-}02 & 2.2600E{-}04 & 0.0000E{+}00 & 0.0000E{+}00 \end{bmatrix}$$

End of Document